nagra.

Arbeitsbericht NAB 21-21

TBO Bözberg-1-1: Data Report

Dossier V Structural Geology

February 2022

National Cooperative
for the Disposal of
Radioactive Waste

Hardstrasse 73
P.O. Box 280
5430 Wettingen
Switzerland
Tel. +41 56 437 11 11

www.nagra.ch

nagra.

Arbeitsbericht NAB 21-21

TBO Bözberg-1-1: Data Report

Dossier V Structural Geology

February 2022

A. Ebert[1], L. Gregorczyk[1], S. Cioldi[1], E. Hägerstedt[1] & M. Gysi[2]

[1] Geologiegemeinschaft Strukturgeologie-Experten Nagra Tiefbohrungen

[2] Nagra

Keywords:
BOZ1-1, Jura Ost, TBO, deep drilling campaign, structural geology, goniometry, drill cores

National Cooperative for the Disposal of Radioactive Waste

Hardstrasse 73
P.O. Box 280
5430 Wettingen
Switzerland
Tel. +41 56 437 11 11

www.nagra.ch

Nagra Arbeitsberichte ("Working Reports") present the results of work in progress that have not necessarily been subject to a comprehensive review. They are intended to provide rapid dissemination of current information.

This NAB aims at reporting drilling results at an early stage. Additional borehole-specific data will be published elsewhere.

In the event of inconsistencies between dossiers of this NAB, the dossier addressing the specific topic takes priority. In the event of discrepancies between Nagra reports, the chronologically later report is generally considered to be correct. Data sets and interpretations laid out in this NAB may be revised in subsequent reports. The reasoning leading to these revisions will be detailed there.

This Dossier was prepared by a project team consisting of:
A. Ebert (core description, core photograph picking, core goniometry, writing and QC)
L. Gregorczyk (core description, core photograph picking, core goniometry, writing and QC)
S. Cioldi (core description, core photograph picking and core goniometry)
E. Hägerstedt (core description, core photograph picking and core goniometry)
K. Decker (QC)
M. Gysi (project management, conceptualisation and QC)

Editorial work: Geomecon, P. Blaser and M. Unger

The Dossier has greatly benefitted from technical discussions with, and reviews by, external and internal experts. Their input and work are very much appreciated.

"Copyright © 2022 by Nagra, Wettingen (Switzerland) / All rights reserved.
All parts of this work are protected by copyright. Any utilisation outwith the remit of the copyright law is unlawful and liable to prosecution. This applies in particular to translations, storage and processing in electronic systems and programs, microfilms, reproductions, etc."

Table of Contents

Table of Contents I

List of Tables II

List of Figures III

List of Appendices VIII

1 Introduction 1
1.1 Context 1
1.2 Location and specifications of the borehole 2
1.3 Documentation structure for the BOZ1-1 borehole 6
1.4 Scope and objectives of this dossier 7
1.5 Petrophysical logs and preliminary log analysis available 7
1.6 Borehole deviation 8

2 Methodology 9
2.1 Core goniometry 9
2.1.1 Introduction 9
2.1.2 Workflow 9
2.1.3 Dip picking and dip type classification 11
2.1.4 Dip data for non-oriented and missing cores 13
2.1.5 Goniometry confidence assessment and uncertainties 16
2.2 Structural work 19
2.3 Geo-statistical evaluation 26

3 Inventory of structure types 27
3.1 Examples of fault planes 27
3.2 Examples of fault zones 35
3.3 Examples of fractures / joints 38
3.4 Examples of veins / tension gashes 39
3.5 Examples of stylolites 41
3.6 Examples of open pores 42
3.7 Examples of drilling-induced fractures 44
3.8 Examples of folding 46

4 Geo-statistical evaluation: Results 47
4.1 Entire cored borehole section (255.00 m to 1'037.31 m MD log depth) 47
4.1.1 Basic structural dip evaluation 47
4.1.2 Natural structural discontinuities 51
4.1.3 Fracture density (P32) and distribution 60
4.1.4 Kinematic indicators 60

4.2 Malm ... 65
4.2.1 Wildegg Formation ... 65
4.3 Dogger ... 72
4.3.1 Hauptrogenstein to Ifenthal Formation ... 72
4.3.2 Passwang Formation ... 78
4.3.3 Opalinus Clay ... 83
4.4 Lias (Staffelegg Formation) ... 88
4.5 Keuper ... 95
4.5.1 Klettgau Formation ... 95
4.5.2 Bänkerjoch Formation ... 98
4.6 Muschelkalk ... 103
4.6.1 Schinznach Formation ... 103
4.6.2 Zeglingen Formation ... 110
4.6.3 Kaiseraugst Formation ... 116
4.7 Dinkelberg Formation and Weitenau Formation ... 120

5 Main structural findings ... 123
5.1 Deformed bedding within the Opalinus Clay ... 123
5.2 Fault zone within the Schinznach Formation ... 124
5.3 Fault zone within the Zeglingen Formation ... 126

6 References ... 133

List of Tables

Tab. 1-1: General information about the BOZ1-1 borehole ... 2
Tab. 1-2: Core and log depth for the main lithostratigraphic boundaries in the BOZ1-1 borehole ... 5
Tab. 1-3: List of dossiers included in NAB 21-21 ... 6
Tab. 2-1: Core goniometry confidence assessment of the analysed interval ... 16
Tab. 2-2: Types of structural discontinuities identified in this study ... 20
Tab. 2-3: Systematically recorded parameters for the investigated structures ... 23
Tab. 4-1: Vector means of orientation values for bedding planes and structural discontinuities (Azim: dip azimuth) ... 47
Tab. 4-2: List of interpreted fault zones, mirror-like fault plane (MirFP) zones and associated fracture density classes (FDC) ... 53
Tab. 4-3: List of all kinematic indicators in oriented and non-oriented cores ... 61

List of Figures

Fig. 1-1: Tectonic overview map with the three siting regions under investigation 1
Fig. 1-2: Overview map of the investigation area in the Jura Ost siting region with the location of the BOZ1-1 borehole in relation to the boreholes Riniken and BOZ2-1 3
Fig. 1-3: Lithostratigraphic profile and casing scheme for the BOZ1-1 borehole 4
Fig. 1-4: Borehole deviation within the cored section..... 8
Fig. 2-1: Using a goniometer to determine kinematic indicators along faults..... 11
Fig. 2-2: Symbols for dip types, fracture density classes and kinematic data used for this study..... 12
Fig. 2-3: Two mirror-like fault planes identified at 688.94 m and 689.00 m MD (log depth) in the Klettgau Formation 13
Fig. 2-4: Example of dip data in a non-oriented core interval..... 14
Fig. 2-5: Interval without 360° core photographs from 698.88 m to 699.46 m MD (log depth) in the Klettgau Formation 15
Fig. 2-6: Core – FMI / UBI correlation for a fault at 266.56 m MD (log depth) in the Wildegg Formation..... 17
Fig. 2-7: Core – FMI / UBI correlation from 424.35 m to 425.05 m MD (log depth) in the Klingnau Formation..... 17
Fig. 2-8: Core – FMI / UBI correlation for subhorizontal to shallow dipping bedding 18
Fig. 2-9: The five main groups of structural discontinuities 20
Fig. 2-10: Completed DIN A3 sheet of primary record of the detailed structural core analysis 25
Fig. 3-1: Fault plane 27
Fig. 3-2: Fault plane 28
Fig. 3-3: Fault plane 29
Fig. 3-4: Mirror-like fault plane 30
Fig. 3-5: Mirror-like fault plane 31
Fig. 3-6: Mirror-like fault plane 32
Fig. 3-7: Stylolitic fault plane..... 33
Fig. 3-8: Stylolitic fault plane..... 34
Fig. 3-9: Fault zone with FDC 3..... 35
Fig. 3-10: Fault zone 36
Fig. 3-11: Fault zone 37
Fig. 3-12: Fracture..... 38
Fig. 3-13: Fracture..... 38
Fig. 3-14: Vein / tension gash..... 39

Fig. 3-15: Vein / tension gash ... 39
Fig. 3-16: Vein / tension gash ... 40
Fig. 3-17: Stylolite ... 41
Fig. 3-18: Stylolite ... 41
Fig. 3-19: Stylolites ... 42
Fig. 3-20: Open pores ... 42
Fig. 3-21: Open pores ... 43
Fig. 3-22: Petal fractures ... 44
Fig. 3-23: Discing ... 45
Fig. 3-24: Folding ... 46
Fig. 4-1: Stereogram and depth plot for bedding planes (n = 411) for the entire cored borehole section ... 48
Fig. 4-2: Dip azimuth rose diagram, dip histogram and depth plot for bedding planes (n = 411) for the entire cored borehole section ... 49
Fig. 4-3: Vector azimuth (or walkout) plot with bedding dips (n = 411) in oriented cores ... 50
Fig. 4-4: Overview plot showing P32 fracture densities along the BOZ1-1 borehole and the BOZ1-1B sidetrack ... 52
Fig. 4-5: Stereogram and depth plot of fault planes for the entire cored interval ... 54
Fig. 4-6: Dip azimuth rose diagram, dip histogram and depth plot for fault planes in the entire cored interval ... 55
Fig. 4-7: Stereogram and depth plot for tension gashes / veins, unassigned fractures and joints in the entire cored interval ... 56
Fig. 4-8: Dip azimuth rose diagram of tension gashes / veins, unassigned fractures and joints in the entire cored interval ... 57
Fig. 4-9: Stereogram and depth plot for stylolites (n = 574) along the cored BOZ1-1 borehole and BOZ1-1B sidetrack ... 58
Fig. 4-10: Dip azimuth rose diagram and depth plot for stylolites in the entire cored interval ... 59
Fig. 4-11: Plunge azimuth of striations along fault planes in the entire cored interval ... 61
Fig. 4-12: Stereogram with striations on all oriented fault planes (including multiple lineations on a single fault plane) and associated kinematic data ... 62
Fig. 4-13: Stereogram with all striations on oriented thrust / reverse fault planes (including multiple lineations on a single fault plane) ... 62
Fig. 4-14: Stereogram with all oriented normal fault planes (including multiple lineations on a single fault plane) and associated striations ... 63
Fig. 4-15: Stereogram with all oriented strike-slip fault planes (including multiple lineations on a single fault plane) and associated striations ... 63
Fig. 4-16: Stereogram with all oriented fault planes (including multiple lineations on a single fault plane) with unknown shear sense ... 64
Fig. 4-17: Stereogram and depth plot of fault planes (Wildegg Formation) ... 65

Fig. 4-18: Dip azimuth rose diagram, dip histogram and depth plot of fault planes (Wildegg Formation) 66

Fig. 4-19: Stereogram and depth plot of tension gashes / veins and unassigned fractures (Wildegg Formation) 67

Fig. 4-20: Dip azimuth rose diagram, dip histogram and depth plot of tension gashes / veins, joints and unassigned fractures (Wildegg Formation)..... 68

Fig. 4-21: Stereogram and depth plot of stylolites (Wildegg Formation, n = 262) 69

Fig. 4-22: Dip azimuth rose diagram, dip histogram and depth plot of stylolites (Wildegg Formation, n = 262) 70

Fig. 4-23: Stereogram of fault planes with striation, including multiple lineations on a single fault plane (Wildegg Formation, n = 150)..... 71

Fig. 4-24: Stereogram and depth plot of fault planes (Hauptrogenstein to Ifenthal Formation) 72

Fig. 4-25: Dip azimuth rose diagram, dip histogram and depth plot of fault planes (Hauptrogenstein to Ifenthal Formation) 73

Fig. 4-26: Stereogram and depth plot of tension gashes / veins, joints and unassigned fractures (Hauptrogenstein to Ifenthal Formation) 74

Fig. 4-27: Stereogram and depth plot of stylolites (Hauptrogenstein to Ifenthal Formation; n = 51)..... 75

Fig. 4-28: Dip azimuth rose diagram, dip histogram and depth plot of stylolites (Hauptrogenstein to Ifenthal Formation; n = 51)..... 76

Fig. 4-29: Stereogram of fault planes with striations, including multiple lineations on a single fault plane (Hauptrogenstein to Ifenthal Formation; n = 40)..... 77

Fig. 4-30: Stereogram and depth plot of fault planes (Passwang Formation) 78

Fig. 4-31: Stereogram and depth plot of tension gashes / veins, joints and unassigned fractures (Passwang Formation) 79

Fig. 4-32: Stereogram and depth plot of stylolites (Passwang Formation; n = 15)..... 80

Fig. 4-33: Dip azimuth rose diagram, dip histogram and depth plot of stylolites (Passwang Formation; n = 15)..... 81

Fig. 4-34: Stereogram of fault planes with striations (Passwang Formation; n = 6) 82

Fig. 4-35: Stereogram and depth plot of fault planes (Opalinus Clay)..... 83

Fig. 4-36: Dip azimuth rose diagram, dip histogram and depth plot of fault planes (Opalinus Clay)..... 84

Fig. 4-37: Stereogram and depth plot of tension gashes / veins, joints and unassigned fractures (Opalinus Clay)..... 85

Fig. 4-38: Dip azimuth rose diagram, dip histogram and depth plot of tension gashes / veins, joints and unassigned fractures (Opalinus Clay)..... 86

Fig. 4-39: Stereogram of fault planes with striations, including multiple lineations on a single fault plane (Opalinus Clay; n = 71)..... 87

Fig. 4-40: Stereogram and depth plot of fault planes (Lias)..... 88

Fig. 4-41: Dip azimuth rose diagram, dip histogram and depth plot of fault planes (Lias)..... 89

Fig. 4-42: Stereogram and depth plot of tension gashes / veins, joints and unassigned fractures (Lias) 90
Fig. 4-43: Dip azimuth rose diagram, dip histogram and depth plot of tension gashes / veins, joints and unassigned fractures (Lias) 91
Fig. 4-44: Stereogram and depth plot of stylolites (Lias; n = 22) 92
Fig. 4-45: Dip azimuth rose diagram, dip histogram and depth plot of stylolites (Lias; n = 22) 93
Fig. 4-46: Stereogram of fault planes with striations, including multiple lineations on a single fault plane (Lias; n = 28) 94
Fig. 4-47: Stereogram and depth plot of faults (Klettgau Formation) 95
Fig. 4-48: Dip azimuth rose diagram, dip histogram and depth plot of faults (Klettgau Formation) 96
Fig. 4-49: Stereogram of fault planes with striations, including multiple lineations on a single fault plane (Klettgau Formation; n = 89) 97
Fig. 4-50: Stereogram and depth plot of faults (Bänkerjoch Formation) 98
Fig. 4-51: Dip azimuth rose diagram, dip histogram and depth plot of faults (Bänkerjoch Formation) 99
Fig. 4-52: Stereogram and depth plot of tension gashes / veins, joints and unassigned fractures (Bänkerjoch Formation) 100
Fig. 4-53: Dip azimuth rose diagram, dip histogram and depth plot of tension gashes / veins, joints and unassigned fractures (Bänkerjoch Formation) 101
Fig. 4-54: Stereogram of fault planes with striations, including multiple lineations on a single fault plane (Bänkerjoch Formation; n = 169) 102
Fig. 4-55: Stereogram and depth plot of fault planes (Schinznach Formation) 103
Fig. 4-56: Dip azimuth rose diagram, dip histogram and depth plot of fault planes (Schinznach Formation) 104
Fig. 4-57: Stereogram and depth plot of tension gashes / veins, joints and unassigned fractures (Schinznach Formation) 105
Fig. 4-58: Dip azimuth rose diagram, dip histogram and depth plot of tension gashes / veins, joints and unassigned fractures (Schinznach Formation) 106
Fig. 4-59: Stereogram and depth plot of stylolites (Schinznach Formation; n = 219) 107
Fig. 4-60: Dip azimuth rose diagram, dip histogram and depth plot of stylolites (Schinznach Formation; n = 219) 108
Fig. 4-61: Stereogram of fault planes with striations, including multiple lineations on a single fault plane (Schinznach Formation; n = 52) 109
Fig. 4-62: Stereogram and depth plot of fault planes (Zeglingen Formation) 110
Fig. 4-63: Dip azimuth rose diagram, dip histogram and depth plot of fault planes (Zeglingen Formation) 111
Fig. 4-64: Stereogram and depth plot of tension gashes / veins, joints and unassigned fractures (Zeglingen Formation) 112
Fig. 4-65: Dip azimuth rose diagram, dip histogram and depth plot of tension gashes / veins, joints and unassigned fractures (Zeglingen Formation) 113

Fig. 4-66: Stereogram and depth plot of stylolites (Zeglingen Formation; n = 5)..... 114
Fig. 4-67: Stereogram of fault planes with striations, including multiple lineations on a single fault plane (Zeglingen Formation; n = 132) 115
Fig. 4-68: Stereogram and depth plot of fault planes (Kaiseraugst Formation) 116
Fig. 4-69: Dip azimuth rose diagram, dip histogram and depth plot of fault planes (Kaiseraugst Formation) 117
Fig. 4-70: Stereogram and depth plot of tension gashes / veins, joints and unassigned fractures (Kaiseraugst Formation) 118
Fig. 4-71: Stereogram of fault planes with striations, including multiple lineations on a single fault plane (Kaiseraugst Formation; n = 45)..... 119
Fig. 4-72: Stereogram and depth plot of fault planes (Dinkelberg Formation and Weitenau Formation)..... 120
Fig. 4-73: Stereogram and depth plot of tension gashes / veins, joints and unassigned fractures (Dinkelberg Formation and Weitenau Formation) 121
Fig. 4-74: Stereogram of fault planes with striations (Dinkelberg Formation and Weitenau Formation; n = 4)..... 122
Fig. 5-1: Deformed bedding in the Opalinus Clay from 624.10 m to 625.40 m MD (log depth)..... 123
Fig. 5-2: Overview plot of the fault zone within the Schinznach Formation at 850.27 m to 851.52 m MD (log depth) in BOZ1-1..... 124
Fig. 5-3: Stereogram with interpreted structures in the fault zone from 850.27 m to 851.52 m MD (log depth). 125
Fig. 5-4: Overview plot of the viscose deformation zone (from 883.75 m to 915.54 m MD log depth) including the flanked brittle deformation (from 881.05 m to 883.75 m MD log depth and from 915.54 m to 922.30 m MD log depth) 127
Fig. 5-5: Different deformation fabrics in drill cores 128
Fig. 5-6: Stereogram and depth plot of fault planes of the viscose deformation zone (from 883.75 m to 915.54 m MD log depth) including the flanked brittle deformation (from 881.05 m to 883.75 m MD log depth and from 915.54 m to 922.30 m MD log depth) 129
Fig. 5-7: Stereogram and depth plot of tension gashes / veins and unassigned fractures of the viscose deformation zone (from 883.75 m to 915.54 m MD log depth) including the flanked brittle deformation (from 881.05 m to 883.75 m MD log depth and from 915.54 m to 922.30 m MD log depth)..... 130
Fig. 5-8: Stereogram of fault planes and associated striations of the viscose deformation zone (from 883.75 m to 915.54 m MD log depth) including the flanked brittle deformation (from 881.05 m to 883.75 m MD log depth and from 915.54 m to 922.30 m MD log depth); n = 132 131
Fig. 5-9: Plunge azimuth rose diagram and plunge histogram of striations of the viscose deformation zone (from 883.75 m to 915.54 m MD log depth) including the flanked brittle deformation (from 881.05 m to 883.75 m MD log depth and from 915.54 m to 922.30 m MD log depth); n = 132..... 132

List of Appendices

App. A: Lithostratigraphy profile Bözberg-1-1, 1:2'500, 0.00 m to 1'037.39 m MD core depth

App. B: Structural geology profile Bözberg-1-1, 1:1'000, 250.00 m to 1'037.31 m MD log depth

App. C-1: Structural geology profile Bözberg-1-1, 1:100, 250.00 m to 525.00 m MD log depth

App. C-2: Structural geology profile Bözberg-1-1, 1:100, 500.00 m to 775.00 m MD log depth

App. C-3: Structural geology profile Bözberg-1-1, 1:100, 750.00 m to 925.00 m MD log depth

App. C-4: Structural geology profile Bözberg-1-1, 1:100, 900.00 m to 1'037.31 m MD log depth

App. D-1: Overview plot of stereograms and rose diagrams: Villigen to Klettgau Fm.

App. D-2: Overview plot of stereograms and rose diagrams: Bänkerjoch to Weitenau Fm.

App. E-1: Core goniometry depth shift table

App. E-2: Core goniometry rotation angle table

App. F: Lithostratigraphy patterns, colours, weathering index and symbols for lithostratigraphy

Note: In the digital version of this report the appendices can be found under the paper clip symbol.

1 Introduction

1.1 Context

To provide input for site selection and the safety case for deep geological repositories for radioactive waste, Nagra has drilled a series of deep boreholes ("Tiefbohrungen", TBO) in Northern Switzerland. The aim of the drilling campaign is to characterise the deep underground of the three remaining siting regions located at the edge of the Northern Alpine Molasse Basin (Fig. 1-1).

In this report, we present the results from the Bözberg-1-1 borehole.

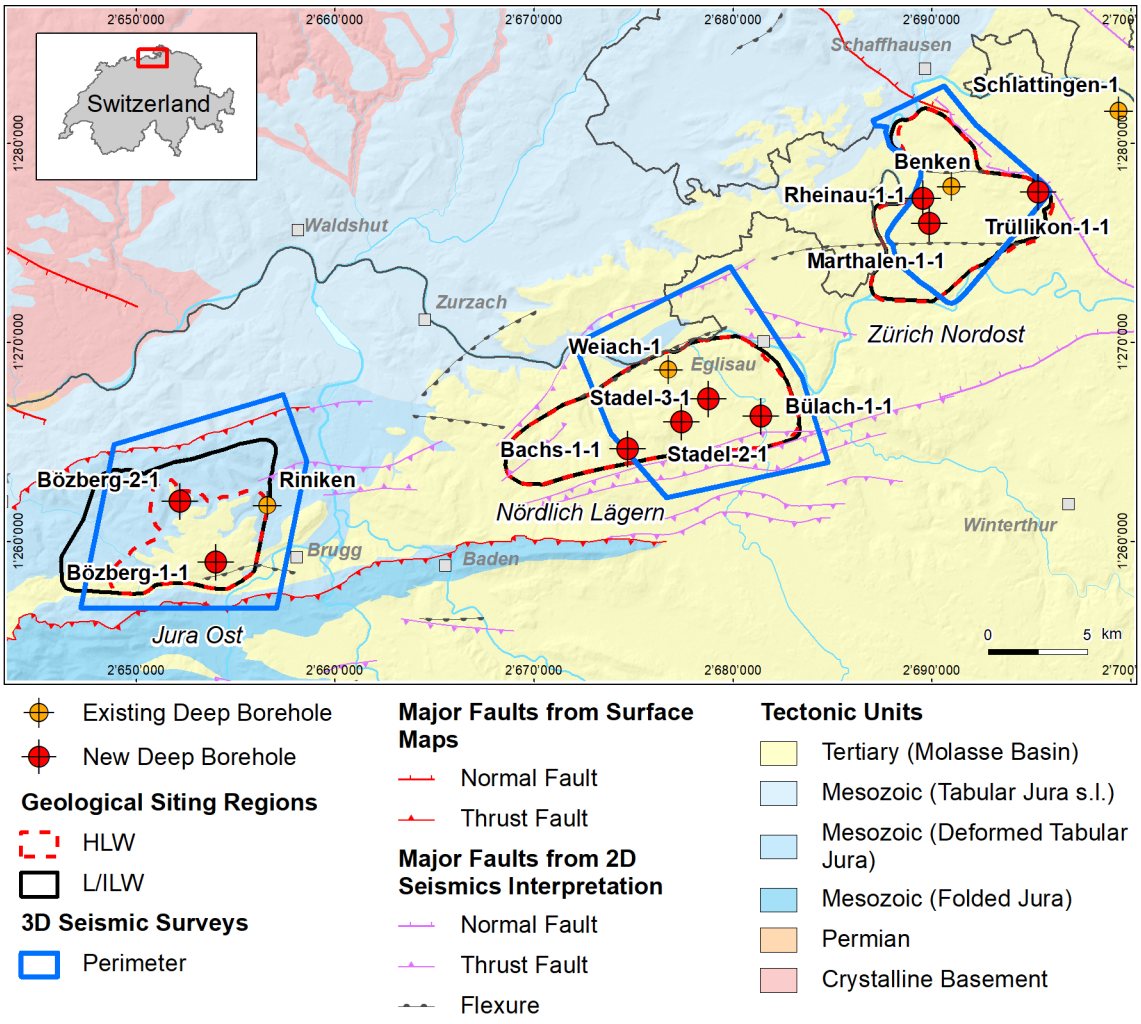


Fig. 1-1: Tectonic overview map with the three siting regions under investigation

1.2 Location and specifications of the borehole

The Bözberg-1-1 (BOZ1-1) exploratory borehole is the fourth borehole drilled within the framework of the TBO project. The drill site is located in the southern part of the Jura Ost siting region (Fig. 1-2). The borehole specifications are provided in Tab. 1-1.

Due to a lost packer system, the borehole was cemented up to 682 m MD[1] (*cf.* Dossier I). Resuming coring operations, a sidetrack was initiated with a kickoff point (KOP) at 709 m MD. This sidetrack was labelled Bözberg-1-1B (BOZ1-1B). BOZ1-1B reached a final depth of 1'037.39 m MD. For easier communication and labelling, the name BOZ1-1 is generally used for this borehole, including the sidetrack, unless stated otherwise.

Tab. 1-1: General information about the BOZ1-1 borehole

Siting region	Jura Ost
Municipality	Bözberg (Canton Aargau / AG), Switzerland
Drill site	Bözberg-1 (BOZ1)
Borehole	Bözberg-1-1 (BOZ1-1) including sidetrack Bözberg-1-1B (BOZ1-1B)
Coordinates	LV95: 2'653'995.815 / 1'258'925.446
Elevation	Ground level = top of rig cellar: 513.29 m above sea level (asl)
Borehole depth	1'037.39 m measured depth (MD) below ground level (bgl) for BOZ1-1B
Drilling period	27th April 2020 – 2nd December 2020 (spud date to end of rig release)
Drilling company	PR Marriott Drilling Ltd
Drilling rig	Rig-16 Drillmec HH102
Drilling fluid	Water-based mud with various amounts of different components such as[2]: 0 – 250 m: Polymers 250 – 882 m: Potassium silicate & polymers 882 – 1'037.39 m: Sodium chloride & polymers

The lithostratigraphic profile and the casing scheme are shown in Fig. 1-3. The comparison of the core versus log depth[3] of the main lithostratigraphic boundaries in the BOZ1-1 borehole is shown in Tab. 1-2.

[1] Measured depth (MD) refers to the position along the borehole trajectory, starting at ground level, which for this borehole is the top of the rig cellar. For a perfectly vertical borehole, MD below ground level (bgl) and true vertical depth (TVD) are the same. In all Dossiers depth refers to MD unless stated otherwise.

[2] For detailed information see Dossier I.

[3] Core depth refers to the depth marked on the drill cores. Log depth results from the depth observed during geophysical wireline logging. Note that the petrophysical logs have not been shifted to core depth, hence log depth differs from core depth.

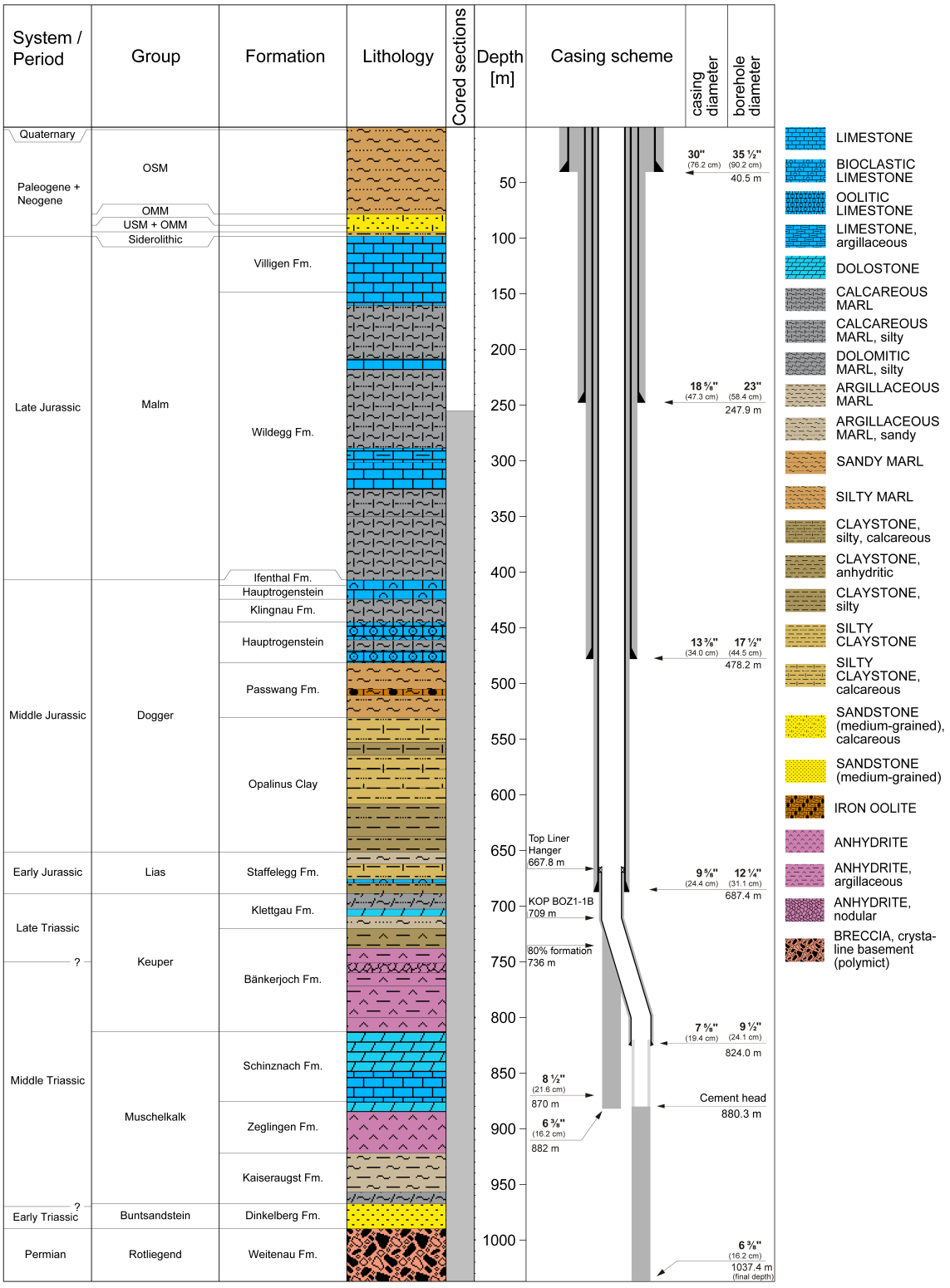


Fig. 1-3: Lithostratigraphic profile and casing scheme for the BOZ1-1 borehole[4]

[4] For detailed information see Dossier I and III.

Tab. 1-2: Core and log depth for the main lithostratigraphic boundaries in the BOZ1-1 borehole[5]

System / Period	Group	Formation	Core depth in m (MD)	Log depth in m (MD)	
Quaternary			**2**		—
Paleogene + Neogene	OSM		78		—
	OMM		88		—
	USM / OMM		94		—
	Siderolithic		**98**		—
Jurassic	Malm	Villigen Formation	148		—
		Wildegg Formation	406.67	406.72	—
	Dogger	Ifenthal Formation	411.91	411.94	—
		Hauptrogenstein	424.11	424.13	—
		Klingnau Formation	444.85	444.93	—
		Hauptrogenstein	481.50	481.55	—
		Passwang Formation	530.28	530.32	—
		Opalinus Clay	651.39	651.46	—
	Lias	Staffelegg Formation	**688.72**	**688.76**	—
Triassic	Keuper	Klettgau Formation	720.03	720.21	—
		Bänkerjoch Formation	812.62	812.45	—
	Muschelkalk	Schinznach Formation	875.89	876.05	—
		Zeglingen Formation	922.22	922.30	—
		Kaiseraugst Formation	967.38	967.70	—
	Buntsandstein	Dinkelberg Formation	**989.89**	**989.83**	—
Permian	Rotliegend	Weitenau Formation	1037.39 final depth		

[5] For details regarding lithostratigraphic boundaries see Dossier III and IV; for details about depth shifts (core goniometry) see Section 2.1.

1.3 Documentation structure for the BOZ1-1 borehole

NAB 21-21 documents the majority of the investigations carried out in the BOZ1-1 borehole, including laboratory investigations on core material. The NAB comprises a series of stand-alone dossiers addressing individual topics and a final dossier with a summary composite plot (Tab. 1-3).

This documentation aims at early publication of the data collected in the BOZ1-1 borehole. It includes most of the data available approximately one year after completion of the borehole. Some analyses are still ongoing (e.g. diffusion experiments, analysis of veins, hydrochemical interpretation of water samples) and results will be published in separate reports.

The current borehole report will provide an important basis for the integration of datasets from different boreholes. The integration and interpretation of the results in the wider geological context will be documented later in separate geoscientific reports.

Tab. 1-3: List of dossiers included in NAB 21-21

Black indicates the dossier at hand.

Dossier	Title	Authors
I	TBO Bözberg-1-1: Drilling	M. Ammen, P.-J. Palten, J. Vliek, K. Gollob & K. Hilgendorf
II	TBO Bözberg-1-1: Core Photography	D. Kaehr & M. Gysi
III	TBO Bözberg-1-1: Lithostratigraphy	M. Schwarz, P. Schürch, H. Naef, P. Jordan, R. Felber, T. Ibele & M. Gysi
IV	TBO Bözberg-1-1: Microfacies, Bio- and Chemostratigraphic Analyses	S. Wohlwend, H.R. Bläsi, S. Feist-Burkhardt, B. Hostettler, U. Menkveld-Gfeller, V. Dietze & G. Deplazes
V	TBO Bözberg-1-1: Structural Geology	A. Ebert, L. Gregorczyk, S. Cioldi, E. Hägerstedt & M. Gysi
VI	TBO Bözberg-1-1: Wireline Logging, Micro-hydraulic Fracturing and Pressure-meter Testing	J. Gonus, E. Bailey, J. Desroches & R. Garrard
VII	TBO Bözberg-1-1: Hydraulic Packer Testing	R. Schwarz, R. Beauheim, S.M.L. Hardie, M. Voß & A. Pechstein
VIII	TBO Bözberg-1-1: Rock Properties, Porewater Characterisation and Natural Tracer Profiles	P. Wersin, L. Aschwanden, L. Camesi, E.C. Gaucher, T. Gimmi, A. Jenni, M. Kiczka, U. Mäder, M. Mazurek, D. Rufer, H.N. Waber, C. Zwahlen & D. Traber
IX	TBO Bözberg-1-1: Rock-mechanical and Geomechanical Laboratory Testing	E. Crisci, L. Laloui & S. Giger
X	TBO Bözberg-1-1: Petrophysical Log Analysis	S. Marnat & J.K. Becker
	TBO Bözberg-1-1: Summary Plot	Nagra

1.4 Scope and objectives of this dossier

The dossier at hand (Dossier V) documents the work of the structural geology experts. The objectives of the report are:

- core goniometry to reset drill cores to the correct depth and original orientation based on high resolution borehole images and high resolution 360° core photographs (Appendices E-1 and E-2)
- structural discontinuities identification on high resolution 360° core photographs and drill cores
- true dip and dip azimuth analysis of structures and bedding planes on high resolution 360° photographs in TerraStation II and/or manual measurements with a geological compass on drill cores
- documentation of recorded structures and their relevant parameters
- visualisation of structural geology data as profiles and overview plots:
  - profile 1:1'000: Appendix B
  - profile 1:100: Appendices C-1 to C-4
  - overview plot of stereograms and rose diagrams: Appendices D-1 and D-2

In this dossier, the following core sections were analysed:

- BOZ1-1: core sections no. 1 to 212, from 255.00 m to 871.20 m MD (core depth)
- BOZ1-1B: core sections no. 13B to 56B, from 871.53 m to 1'037.39 m MD (core depth)
- The overlapping core interval between BOZ1-1 and BOZ1-1B was not analysed and therefore is not documented in this report.

The level of detail in this dossier is limited by the data availability at data cut-off two months after the end of drilling operations. The lithostratigraphic subdivision used in this report is in line with the finding in Dossier III.

1.5 Petrophysical logs and preliminary log analysis available

The petrophysical logs and preliminary log analysis listed below were available at the data-freeze and considered as a supplementary source of information for this report (for more details, see Dossier VI):

- total natural gamma ray borehole and potassium corrected (GR)
- caliper / radius (RD1 to RD6)
- near / array corrected limestone porosity (APLC)
- high resolution formation density (RHO8)
- high resolution formation photoelectric factor (PEF8)
- array laterolog apparent resistivity from computed focusing mode 0 to 5 (RLA1 to RLA5)
- formation micro imager (FMI)
- ultrasonic borehole image (UBI)
- borehole breakouts and centreline fractures analysis based on FMI and UBI images

1.6 Borehole deviation

The cored sections of BOZ1-1 and BOZ1-1B are almost vertical with a slight deviation towards the NNW and a distinct change in deviation towards the N at about 882 m MD (log depth). This change is due to the sidetrack BOZ1-1B. The maximum horizontal deviation within the cored section is about 35 m to NNW at the depth of 1'037.39 (TD). BOZ1-1B is less inclined than BOZ1-1 (Fig. 1-4).

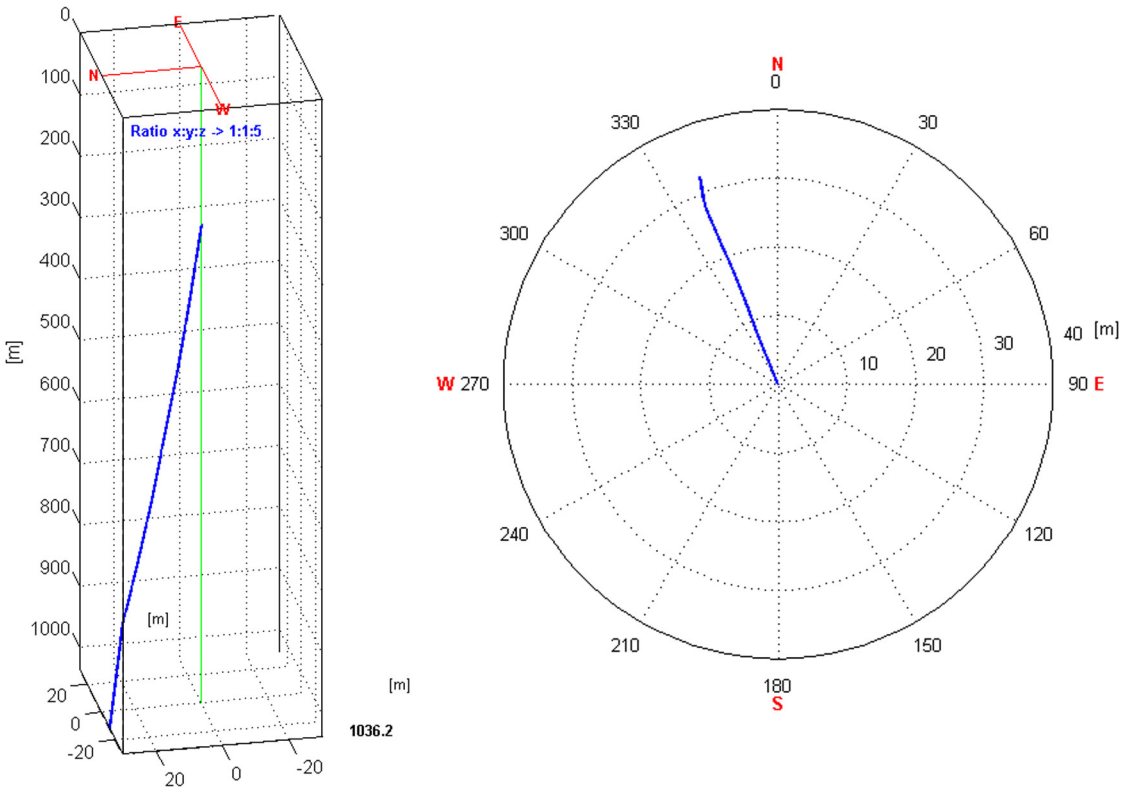


Fig. 1-4: Borehole deviation within the cored section

The left image visualises the borehole path in 3D with a compressed z-axis compared to the x- and y-axis. The borehole azimuth is shown on the right.

2 Methodology

2.1 Core goniometry

2.1.1 Introduction

A structural analysis was performed on drill cores along with circumferential and planar drill core photographs. Using the reference line on the core surface, positioned at an azimuth of 0° during core photography, most drill cores could be oriented using borehole image logs.

For this study, high-resolution 360° and planar photographs were available for most of the cored interval from 255.00 m to 1'037.39 m MD (core depth). The data were delivered as 1'266 circumferential and 1'283 planar photographs in TIF format. However, the original photographs with a resolution of 10 pixels/mm were too large to be handled with TerraStation II (TERRASCIENCES Inc.). Therefore, the original photographs were compressed by 25% and exported with a resolution of 300 dpi. In addition, FMI and UBI logs were available. Both were of good to excellent quality. Further relevant data included auxiliary borehole data, core orientation line and core section listings, lithostratigraphic boundaries and petrophysical logs.

2.1.2 Workflow

This section describes the methodology used for extracting the directional information from 360° core photographs. The following steps were tailored for efficient core goniometry using the TerraStation II software:

1. Quality control of core photographs:

   Prior to loading the data, it was ensured that the core orientation line (red) on the 360° core photographs was set to 0°.

   Note: the core orientation line (COL) represents a continuous reference line set to an azimuth of 0° to fix the relative orientation of drill cores. The COL was drawn on the core surface immediately after core retrieval at the drill site. The line lengths vary widely from a few centimetres up to several metres and therefore sometimes continue over several core sections depending on whether each individual core section could be fitted together along the core edges or not. If core sections could not be merged, a new COL was determined. The coherent COL was then used to orient the drill core using borehole image logs.

2. Data loading:

   All 360° core photographs were loaded as mirror images in order to simulate the borehole image log looking from the inside of the borehole. A constant value of 95 mm (3.74") was added as image diameter.

   The processed FMI and UBI logs as well as the auxiliary petrophysical logs were imported into TerraStation II. It was checked that the depth of the petrophysical logs, especially the first GR (gamma ray) run, matched the depth of the FMI data.

3. Depth shifting:

   The 360° core photographs were shifted to FMI logs using distinct, correlated planar and/or non-planar features. For the purpose of simplicity and consistency, only one shift value was applied for each individual core section (generally 3 m per section). This resulted in minor data gaps and/or overlaps at core section boundaries of a few centimetres maximum. In total, 251 distinct depth shift values were applied for the core sections of the entire cored borehole; these varied from - 0.20 m to + 0.35 m. The defined values are listed in Appendix E-1.

4. Core orientation:

   The core was oriented using correlated geological features (e.g. faults / fractures, inclined / deformed bedding, nodules etc.) which were matched with the orientation on the FMI by rotating the 360° core photographs clockwise around the borehole axis.

   The obtained angle of rotation was then applied to the entire core section with a continuous COL. Simultaneously, the validity across other geological features was checked. Note that the length of a linked COL segment was highly variable and could continue across several core sections. All COLs and the applied angles of rotation of the individual COLs are listed in Appendix E-2. To highlight the uncertainties related to core orientation, an uncertainty assessment was carried out and visualised using three confidence classes.

5. Quality control of core goniometry:

   Prior to the structural recording of the drill cores, the depth shifts, the core correlation with the FMI / UBI combination and the core orientations were reviewed.

The following steps do not belong to classical core goniometry. However, they played a key role in the coherent workflow of the structural core analysis and are thus mentioned here:

6. Dip picking on oriented 360° core photographs:

   Bedding-related planes were picked manually for a structural dip evaluation.

   Structural elements on drill cores were picked manually and characterised in detail with respect to relevant parameters.

7. Recording of kinematic features:

   Kinematic indicators along fault surfaces such as slickensides, striations, shear sense indicators and (fault) offsets were identified and measured on the cores. To determine the lineation azimuth and plunge and/or planes not visible in the photographs, a goniometer constructed by Geo Explorers was used. The drill core was placed in the goniometer facing uphole and rotated around the vertical axis by the angle of rotation determined from the core orientation line. Subsequently, the azimuth and plunge of the striation were measured using a geological compass (see Fig. 2-1).

8. Examination of angular differences:

   Using the TectonicsFP software, the angular differences between the striation azimuths / plunges and the orientation of associated fault planes were checked. If the angular offset exceeded 15°, the fault plane and lineation were remeasured.

9. Quality control:

   A final quality control was performed, with the main focus on consistency (between TerraStation, primary records of structural core analysis and the structural inventory meta-data), completeness of records and the accurate characterisation of the recorded tectonic features.

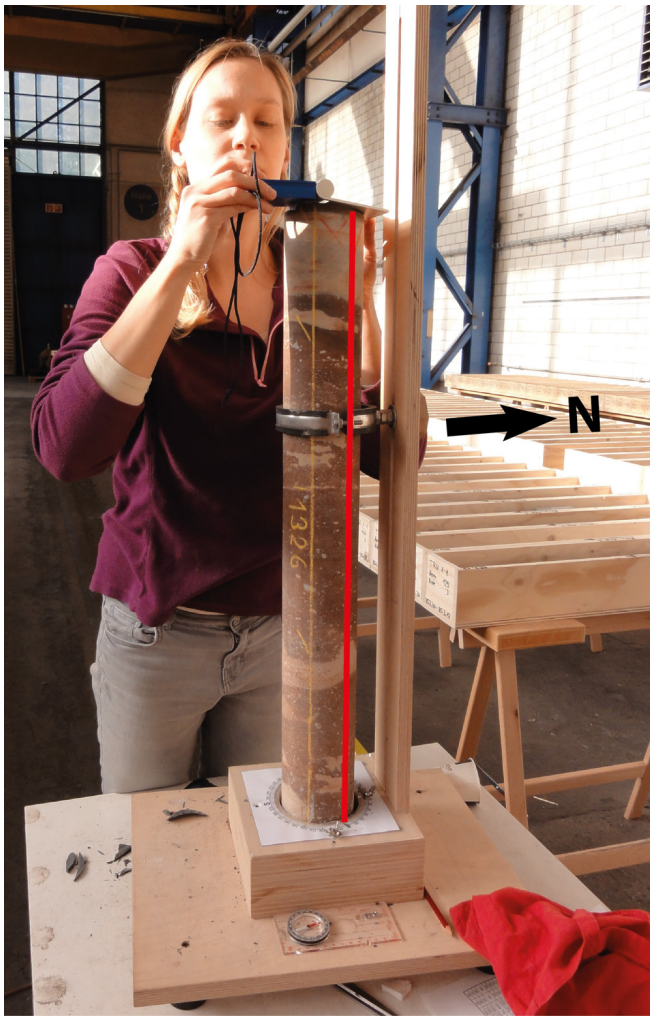


Fig. 2-1: Using a goniometer to determine kinematic indicators along faults

Note the red core orientation line defining the position of the drill core in the goniometer.

2.1.3 Dip picking and dip type classification

Due to higher accuracy and reliability compared to automated methods, a manual sinusoid method and a point-to-point method were used to pick all relevant features on the 360° core photographs. In a cylindrical borehole, a perfect plane will appear as a sine wave on the circumferential core photograph and its amplitude reflects the dip relative to the borehole axis.

Different dip classes were defined for the different structure types. For this study, a total of 15 different dip types were defined in TerraStation II (Fig. 2-2).

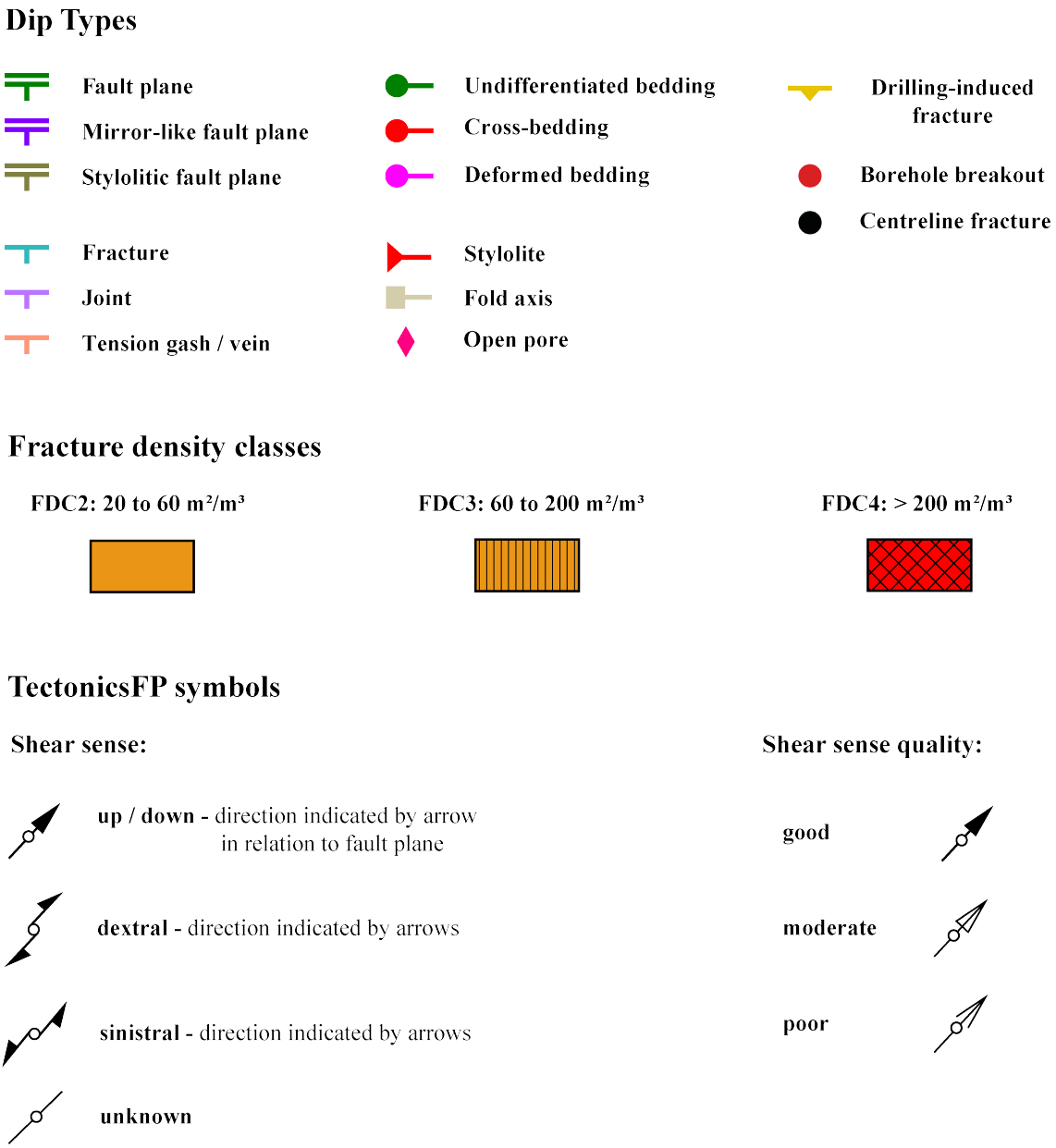


Fig. 2-2: Symbols for dip types, fracture density classes and kinematic data used for this study

Some structures were only visible on planes not outcropping at the rim of the core and were not visible on the 360° core photographs. The orientation of these structures was obtained with a geological compass, as described above, and the data were subsequently imported into the digital dip dataset. Consequently, the associated dip sine waves did not fit with any visible traces and/or were simply not visible at this depth level, as exemplified in Fig. 2-3.

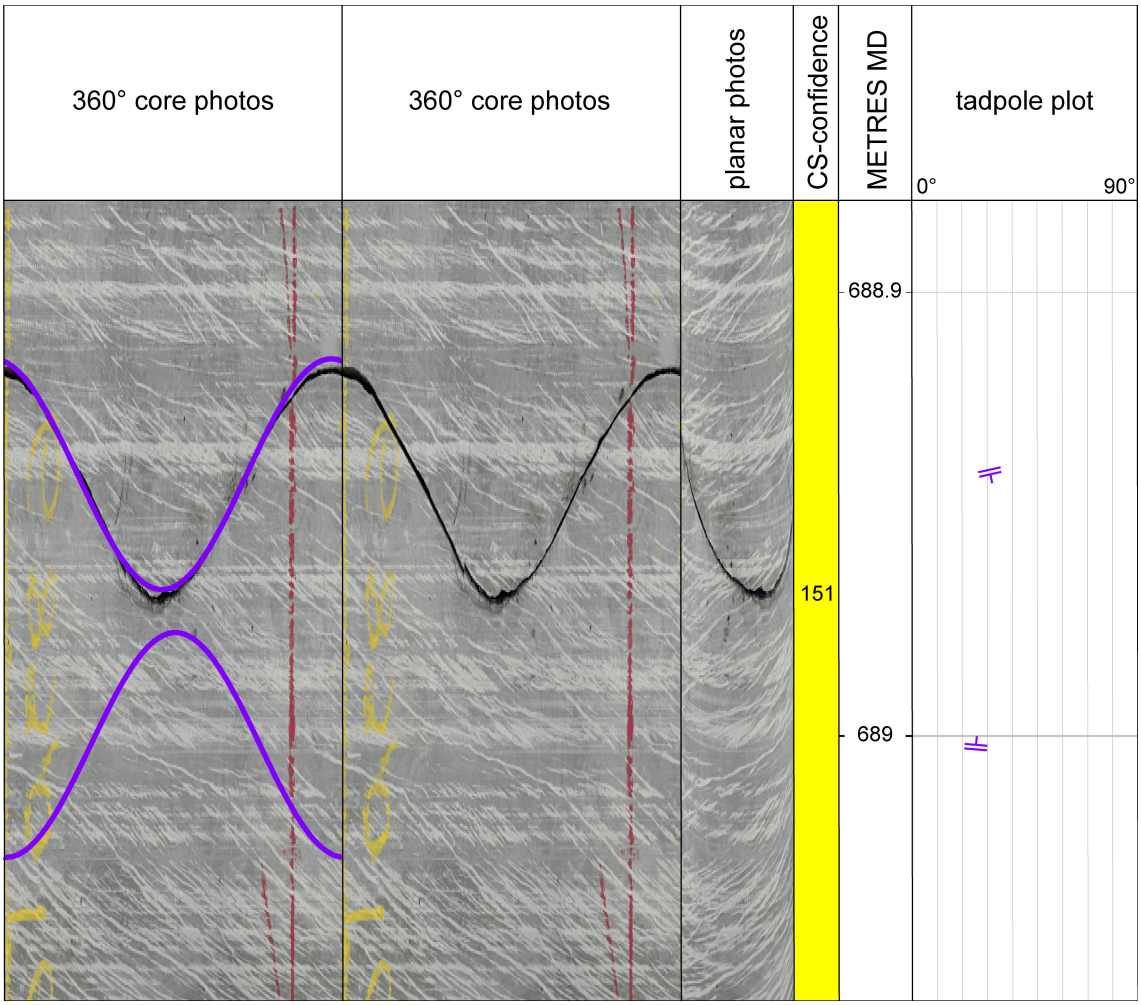


Fig. 2-3: Two mirror-like fault planes identified at 688.94 m and 689.00 m MD (log depth) in the Klettgau Formation

The latter was determined within the drill core.

From left to right: shifted and oriented 360° core photograph with (left) and without (right) picked sine waves, followed by depth-shifted planar core photographs, core section numbering in the coloured bar displaying the goniometry confidence ranking, depth track showing the position and length of the currently displayed window, tadpole plot. Note that the displayed sine wave of the structure at 689.00 m MD (log depth) is not visible in the 360° core photograph. The fault plane was therefore implemented from the core analysis and the orientation obtained from a compass measurement.

2.1.4 Dip data for non-oriented and missing cores

Due to a lack of correlated features, poor data quality or missing image log data, 44.17 m of the available drill cores remained non-oriented. Within these non-oriented drill cores, a total of 25 bedding planes and 49 tectonic / drilling-induced discontinuities could be observed and picked. The structural planes were nevertheless measured manually with a geological compass and included in TerraStation II or picked digitally on 360° core photographs. For non-oriented drill cores and core photographs, the red core orientation line was set to 0°. Because the dip measurements of these features are correct, but the dip azimuth measurements are affected by the lack of orientation, the non-oriented dataset can only be used for fracture density calculations.

To highlight incorrect dip azimuth measurements of these features, a quality indicator of 0 was assigned and open tadpoles were used for visualisation (Fig. 2-4). A quality indicator of 1 was assigned to all correctly oriented features.

For intervals with missing 360° core photographs, short drill core sections could still be oriented using the coherent core orientation line, which sometimes continued across several cores. The depth and orientation of the structures were then measured on the core and the dip data were subsequently imported into the digital database of TerraStation II (see Fig. 2-5).

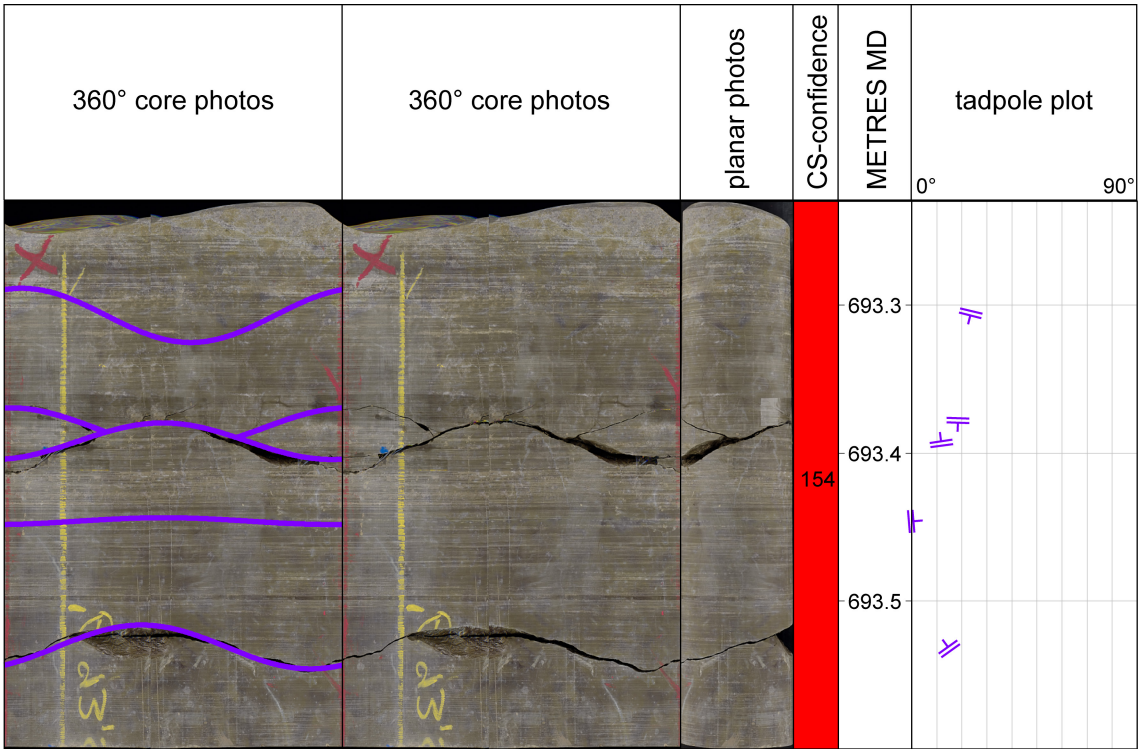


Fig. 2-4: Example of dip data in a non-oriented core interval

The goniometry confidence is set to "core not oriented" (red). Example from the Klettgau Formation from 693.23 m to 693.60 m MD (log depth).

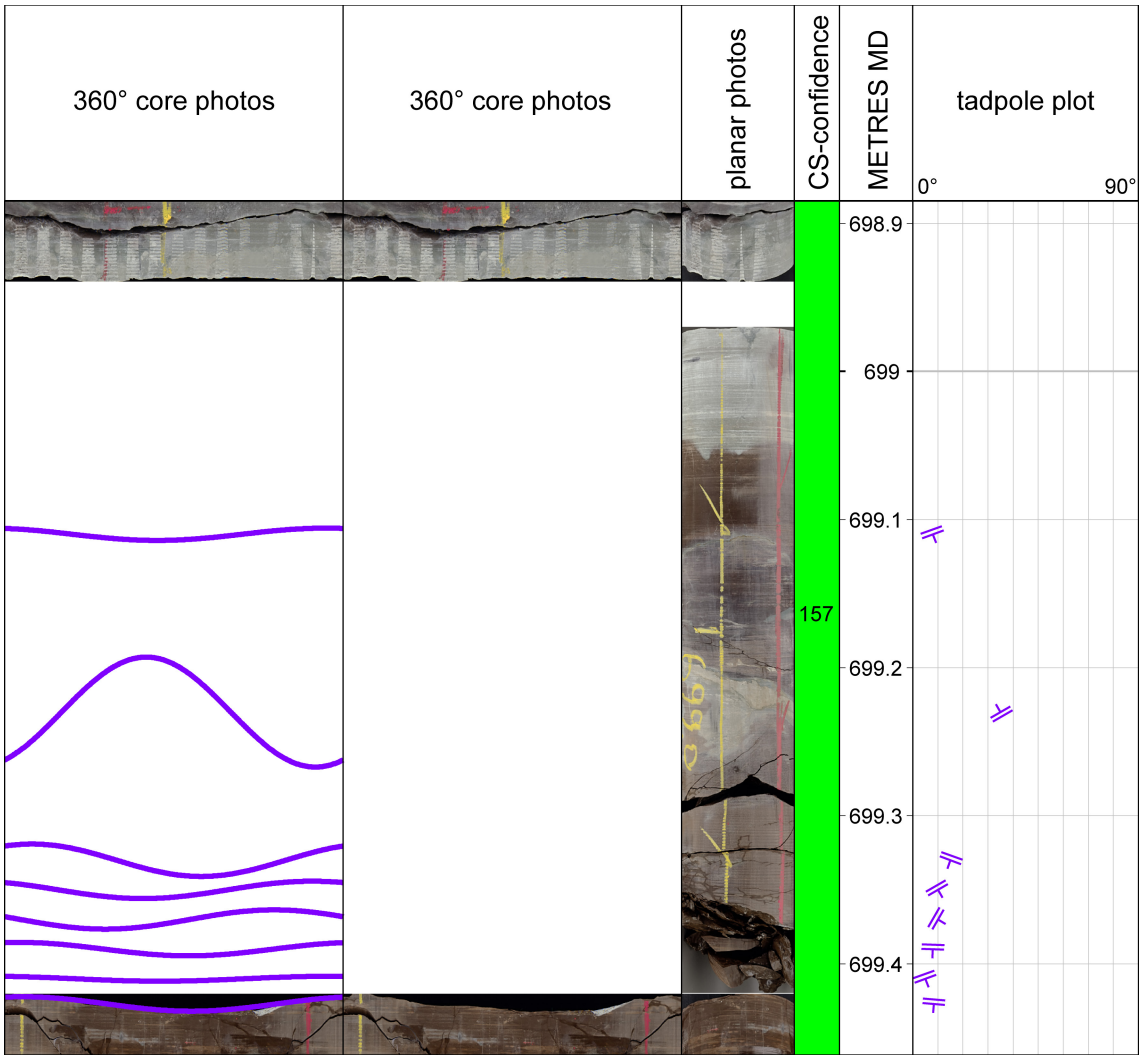


Fig. 2-5: Interval without 360° core photographs from 698.88 m to 699.46 m MD (log depth) in the Klettgau Formation

In this example, the core goniometry and structural analysis were performed directly on the drill core. The orientation data were determined with a geological compass and subsequently imported into the digital dip database of TerraStation II. The goniometry confidence for this core section is high (green).

2.1.5 Goniometry confidence assessment and uncertainties

Goniometry confidence ranking

To visualise the uncertainties related to the core goniometry, the reliability of the core orientation was classified using a confidence ranking scheme. The assessment was carried out for each connected core orientation line and depended particularly on the number of reliably correlated features within these intervals. Features with a moderate to steep (> 15°) dip generally provided a higher confidence and resulted in lower angular uncertainties than e.g. shallow structures (< 15°). The features used for the core goniometry are listed in Appendix E-2 along with the coherent COL. Examples of the correlated features between the FMI and the core are presented in Figs. 2-6, 2-7 and 2-8.

There are three confidence levels for the goniometry illustrated as coloured fields in the structural composite plots (Appendix B and C). The confidence level depends on the number of evident structures found within each coherent core orientation line:

- high is defined by three or more distinct, preferably moderately inclined to steep (> 15°) planar and/or non-planar features (Fig. 2-6), resulting in a high angular accuracy
- moderate is associated with one or two correlated (non-)planar structures with shallow to moderate dip angles (< 15°; Figs. 2-7 and 2-8); thus, the core orientation contains some uncertainty and is less accurate
- not oriented is characterised by a lack of obvious indicators for the core orientation; these cores are not oriented

Tab. 2-1 gives an overview of the core goniometry confidence assessment. The procedure described in Section 2.1.2 resulted in a successful orientation of 729.05 m out of the total 773.22 m drill cores (94%), retrieved form the cored interval from 255.00 to 1'037.31 m MD (core depth).

Tab. 2-1: Core goniometry confidence assessment of the analysed interval

Interval			**Goniometry confidence**								
Top	**Bottom**	**Length**	**High**			**Moderate**			**Not oriented**		
[m MD core depth]			[m]	[%]	No. of COL	[m]	[%]	No. of COL	[m]	[%]	No. of COL
255.00	1'037.31	773.22	411.62	53	33	317.43	41	54	44.17	6	31

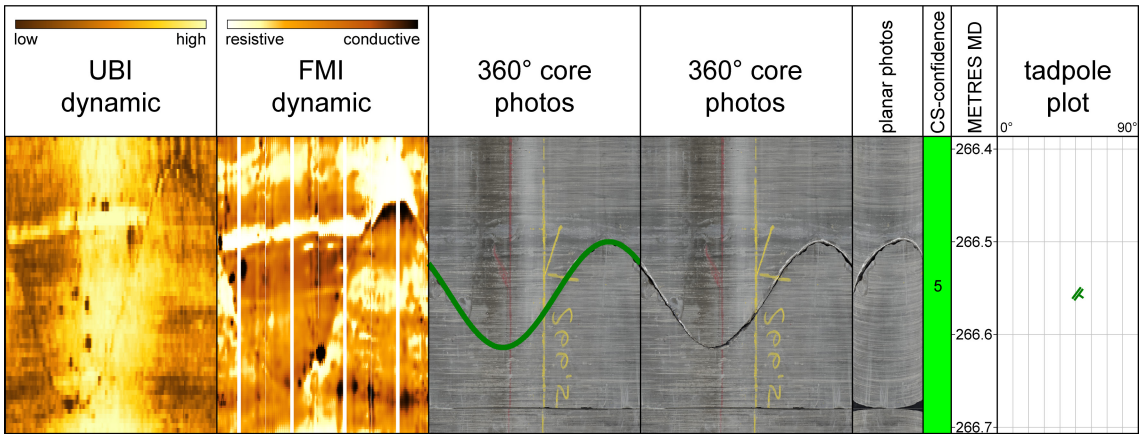


Fig. 2-6: Core – FMI / UBI correlation for a fault at 266.56 m MD (log depth) in the Wildegg Formation

This prominent 52° SE-dipping fault was unequivocally correlated across the UBI and FMI logs and the core photographs and therefore represents a high-confidence indicator for the core orientation. From left to right: acoustic UBI image log, dynamic normalised FMI images, shifted and oriented 360° core photographs with (left) and without (right) sine waves, followed by shifted planar core photographs. The core section numbering is shown in the coloured bar displaying the goniometry confidence ranking (high – green, moderate – yellow, red – not oriented). The depth track shows the position and length of the currently displayed window (33 cm). A tadpole plot with true orientations of manually picked planes is also displayed.

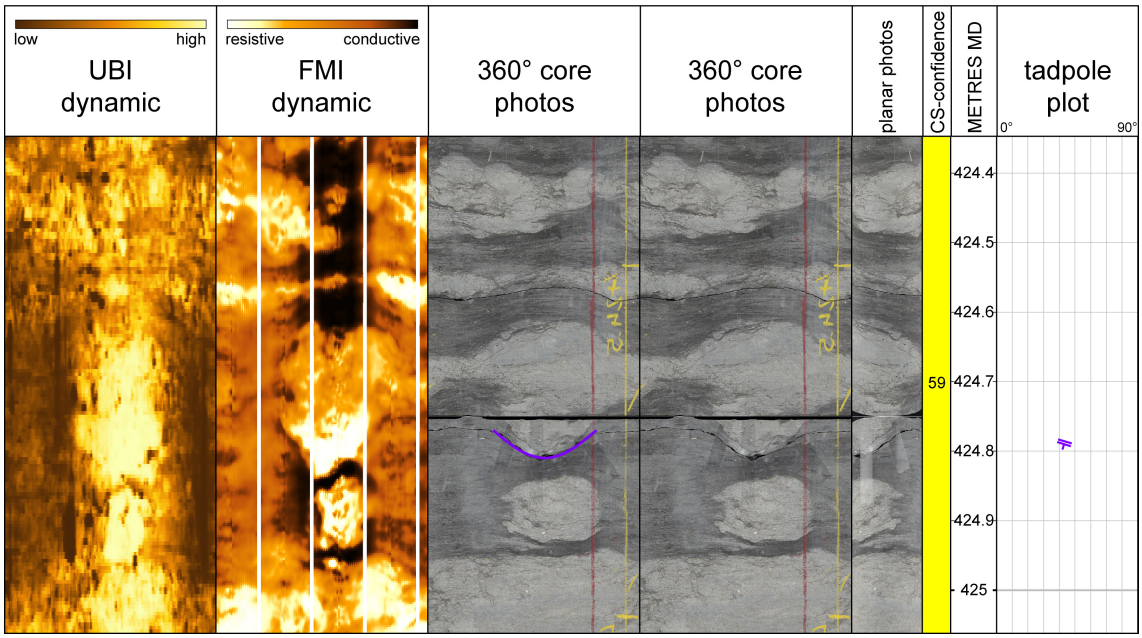


Fig. 2-7: Core – FMI / UBI correlation from 424.35 m to 425.05 m MD (log depth) in the Klingnau Formation

These unique structures represent nodules which appear bright (high amplitude) on the UBI and resistive on the FMI images. They were used to shift and orient core section 59. Due to their heterogeneous nature, they are considered as indicators of limited quality for the core goniometry and assigned a moderate confidence level (yellow).

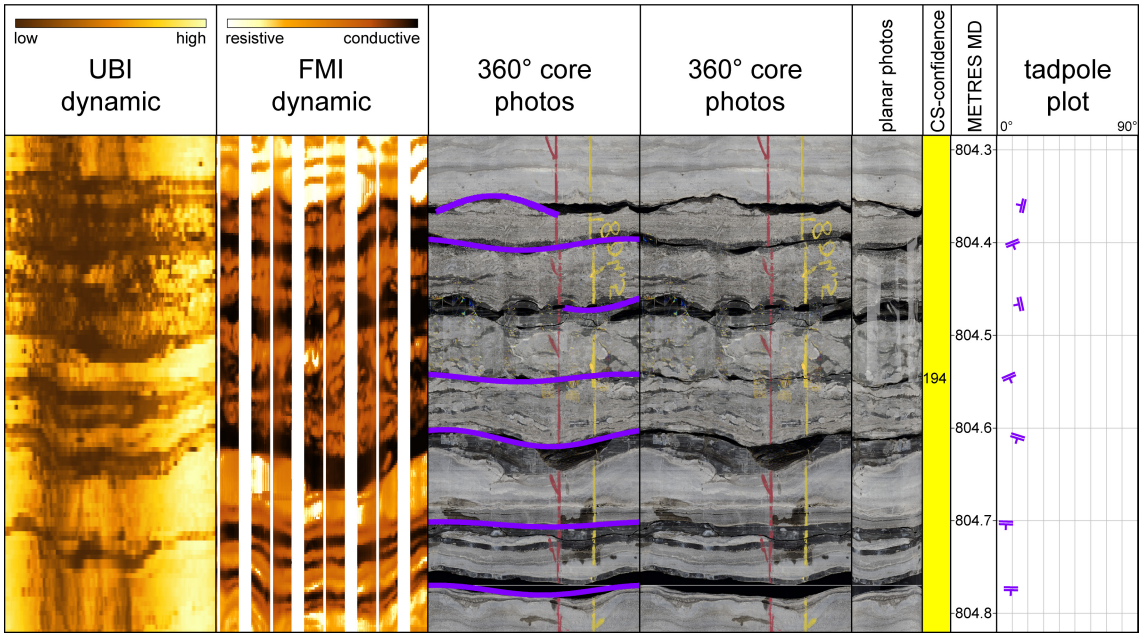


Fig. 2-8: Core – FMI / UBI correlation for subhorizontal to shallow dipping bedding

The FMI and the core photograph match within the well-bedded strata in the Bänkerjoch Formation from 804.28 m to 804.82 m MD (log depth). Although the bedding planes are clearly visible on the FMI and core photographs, the relatively low dip angles (< 15°) imply some angular uncertainty and are therefore considered as moderate indicators for core goniometry (yellow).

Project-specific uncertainties

A number of unavoidable limitations and uncertainties were associated with the work performed and may have affected the accuracy of the results. These factors are evaluated below:

- angular uncertainty is associated with the core goniometry and is reflected by the confidence scheme. It particularly implies an angular error for the azimuth

- errors related to compass measurements on drill cores: to explore the measurement-related error, multiple measurements of the same structure were performed by different users. The reproducibility was 5° for the dip magnitudes and 5° to 10° for the dip azimuths. Considering that most geological compasses have an error margin within 2° for dip azimuth and magnitude, it can be concluded that the above-mentioned goniometer has an acceptable error margin and can safely be used for accurate structural core analysis

- dip picking on 360° photographs: the pixel resolution of the screen defines the angular uncertainty of the dip picks in 3D space and is 1° to 2° for the dip angle and 2° to 4° for the dip azimuth
  - core photographs: although the derived 360° core photographs covered almost the entire studied interval (255.00 m to 1'037.39 m MD core depth), some data gaps occurred, e.g. from 480.02 m to 483.00 m MD (core depth), from 690.01 m to 692.00 m MD (core depth) and from 728.83 m to 732.70 m MD (core depth). The missing core sections are mostly due to pilot holes for formation integrity tests, hence no core photographs could be taken. In case of highly fractures or disintegrated cores, 360° core photographs have not been recorded, as these intervals were not suitable for circumferential photography
  - in some core intervals the core orientation line was discontinuous. This was mainly related to uncertainties in fitting individual core pieces / sections together. In such cases, the non-coherent core sections were treated separately (see Appendix E-2)
  - due to the presence of steel in Nagra's core storage facility in Würenlingen, a site-specific magnetic field disturbance was recognised. Consequently, the goniometer needed to be carefully aligned towards relative north to obtain the correct orientations of the geological features (mainly lineations) measured with a compass. This always had to be kept in mind when moving the equipment across the core store

2.2 Structural work

This section describes (A) how the structural recording and characterisation of drill cores were carried out, (B) which structure types were distinguished, and (C) which structure parameters were defined. Details with regard to the structural core analysis are given in the structural analysis manual and enclosed factsheets and templates (Ebert & Decker 2019).

A) After the core goniometry was finalised, all deformation structures were recorded on the drill cores. The recording was usually completed within a few weeks.

   The overall core quality was excellent. Only cores from clay-rich lithologies (particularly the Dogger) were affected by progressive discing but were still suitable for structural analysis. Due to 472 samples with lengths of up to 50 cm being taken at the drill site (e.g. for porewater or geomechanical analyses), there were gaps within the core sections. Samplers were strictly advised not to sample core intervals containing tectonic structures. The completeness of the structural record is therefore not biased or limited by sampling. Furthermore, it can be assumed that the complete structural inventory was recorded because high-resolution core photographs were taken from all cores, including the sampled core sections.

   Most of the structural work was performed by two people. A structural geology expert defined all visible structure types along with their relevant parameters for each core section, which was usually 3 m long. At the same time, the other colleague manually picked the structures on the 360° core photographs in TerraStation II. The structures and their parameters such as mineralisation, thickness or shear sense were documented on a DIN A3 template with content previously defined in Ebert & Decker (2019). The log depth was determined in metres MD along with the true orientation of the structures on oriented 360° core photographs. The difference in depth between the core and log depth mostly varied between -0.20 m and +0.35 m and depended on the dynamic depth shift of the core photographs with regard to the FMI used as the main depth reference data. Striations on slickensides recognised on surfaces of broken cores were measured with a geological compass (Fig. 2-1). As soon as a core section was completely analysed, all entries from the DIN A3 template were digitised and data QC was carried out.

B) Depending on rock rheology and the type and degree of deformation, different types of structural discontinuities may develop. Based on this, the structures were subdivided into five main groups of structural discontinuities (Fig. 2-9). In total, 11 types of structures were distinguished in this study (Tab. 2-2) and are illustrated with numerous examples in Chapter 3. Detailed definitions and information on the origin of the structures can be found in the structural analysis manual of Ebert & Decker (2019).

C) Additionally, parameters such as mineralisation, shear sense and thickness (listed in Tab. 2-3) were determined and documented for each individual structure on the DIN A3 template (Fig. 2-10). Each structure was sketched and labelled with a consecutive number on the designed grid with a scale of 1:10.

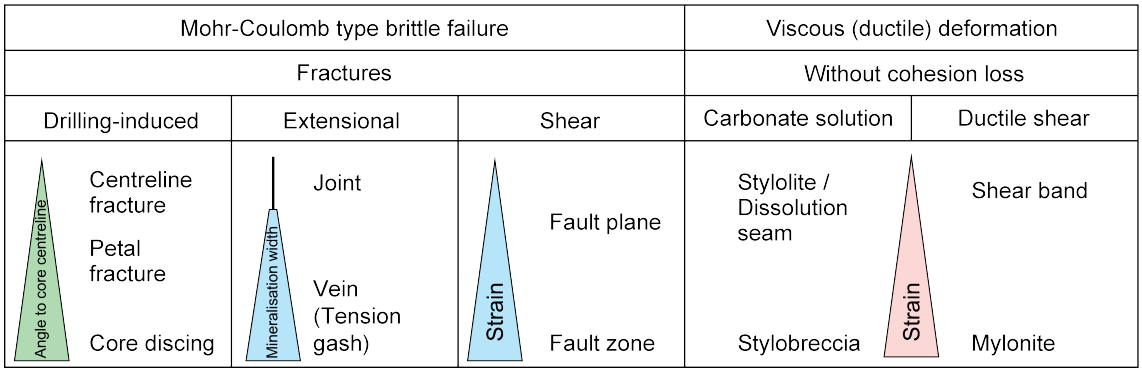


Fig. 2-9: The five main groups of structural discontinuities

Tab. 2-2: Types of structural discontinuities identified in this study

For more details see Ebert & Decker (2019).

Discontinuity group	**Structure type**	**Characteristics**
Brittle structures with shear indications	Fault plane	Planes of shear failure, i.e. planes along which there has been movement parallel to the plane (Peacock et al. 2016). Single, thin, planar and sharp structural discontinuities with shear indications (e.g. striations or slickenfibres).
	Mirror-like fault plane	A fault plane with a smoothed, polished or shiny slip surface.
	Stylolitic fault plane	A fault plane with dissolution seams and stylolite-bearing columns which are oblique or parallel to the plane (modified from Hancock 1985).
	Fault zone	A fault zone is defined as a zone with a volume which includes interacting and linked fault segments, densely fractured rock and/or fault rocks; zones are typically bounded by subparallel margins or fault planes (modified from Peacock et al. 2016).

Tab. 2-2: continued

Discontinuity group	**Structure type**	**Characteristics**
Brittle structures without shear or slip indications	Joint	A barren, closed fracture on which there is no measurable slip or dilation at the scale of observation. If any mineral fill, including crystal growth fibres, is visible, the structure is better called a vein (Hancock 1985).
	Vein	Extensional fracture filled by secondary mineral crystallisation.
	Tension gash	Vein formed by dilation; tension gashes may be fully cemented (vein), partly cemented (partly open) or open (Passchier & Trouw 1996).
Structure without preserved evidence for the mode of fracturing	Fracture	General term for a structure without preserved evidence for the mode of fracturing, i.e. it is applicable to structures formed by extension or shear; fractures can include close-to-planar discontinuities such as dykes, faults, joints and veins (Peacock et al. 2016).
Structures caused by dissolution	Stylolites	Stylolites are irregular seams of insoluble residues with dark, "mountainous" rough teeth formed by pressure solution (Passchier & Trouw 1996).
	Open pores	Isolated open volumes in the rock mass, resulting e.g. from incomplete cementation of veins, dissolution or preserved cavities in fossils.
	Karst	Open networks resulting from dissolution of carbonates. These cm- to m-wide cavities may have been refilled later.
Fabrics without cohesion loss, e.g. caused by ductile deformation	Shear bands	Minor planar shear zones in which the progressive deformation is non-coaxial (Passchier & Trouw 1996).
	Mylonites	Strongly deformed rock from a ductile shear zone with a planar foliation and usually with a stretching lineation (Passchier & Trouw 1996).
	Schistosity	Secondary foliation defined by preferred orientation of equant fabric elements in a medium- to coarse-grained rock. Individual foliation-defining elements (e.g. micas) are visible with the naked eye (Passchier & Trouw 1996).
	Dynamic recrystallisation	Dynamically recrystallised, smaller and elongated crystals.

Tab. 2-2: continued

Discontinuity group	**Structure type**	**Characteristics**
Drilling-induced fractures (DIF)	Drilling-induced fractures	Collective term for fractures created by forces associated with drilling and coring procedures. Depending on load on drill bit, mud weight and rock properties, drilling-induced fractures develop during drilling or shortly thereafter. Based on the aperture, fracture surface and geometric relationships, drilling-induced fractures can be distinguished from natural fractures. Drilling-induced fractures are always open and never mineralised.
	Petal fracture	Drilling-induced fracture with convex-up geometry cutting a core downwards starting from its perimeter. Petal fractures form immediately ahead of the drill bit as a result of excessive bit weight during coring. They propagate downhole.
	Centreline fracture	Drilling-induced fracture that typically splits a core approximately in half.
	Core discing	The formation of discs of relatively uniform thickness which fracture on surfaces approximately normal to the axis of the core.
Additional features / dip types	Undifferentiated bedding	Planar surface representing either the boundary between two different lithological units or internal bedding. Thought to reflect original horizontal and planar surfaces.
	Deformed bedding	Bedding planes occurring in narrow zones in any lithology with moderate to steep dip angles (> 15°) which differ from the general structural dip. They have been subjected to deformation due to faulting and/or folding.
	Cross-bedding	Inclined foreset surfaces in sandstone occurring in sets and bounded by set boundaries. These sedimentary features may be used as paleocurrent indicators. Upper truncation by the next set is diagnostic.
	Fold (axis)	One or a stack of originally flat and planar surfaces, such as sedimentary rocks, that are bent or curved due to applied external stress. Folds appear in various scales and shapes.
	Fracture density	Numerical value that reflects a quantitative measure of the abundance of fractures in rock mass (e.g. fractures per metre, fracture area per rock volume).

Tab. 2-3: Systematically recorded parameters for the investigated structures

Parameter	**Definition of parameters and procedure for defining parameters**
Depth	All types of structures are recorded quantitatively along the scanline of the core axis. The depth of the structure is measured at the point where it cuts the core axis. For steeply dipping planes, the depth should be determined halfway between the top edge and the base of the intersection ellipse of the structure. If a zone is recorded (e.g. fault zone, shear band, fracture density class), the top (Top MD) and the base (Bottom MD) of the zone are specified in the corresponding columns.
Core orientation line number	After the extraction of the core from the inner tube, the core pieces are juxtaposed whenever possible. Continuous sections without drilling breaks, demarcated by grinding, crushed or core loss zones, are marked with a core orientation line and denoted with a consecutive number. This number enables linking of the recorded structure with the key structure of this orientation line section that was identified on the borehole image.
Depth shift between core and FMI	The depth shift is defined using correlated structures visible on both the FMI and core.
Correlation with log	Assessment of whether each individual structure can be clearly identified on FMI / UBI and core. "yes" indicates that the structure can be correlated with the image log and "no" indicates structures which cannot be correlated, or which are not shown by the image log. In addition, a correlation quality ranking is carried out (1 – good, 2 – moderate, 3 – no correlation).
Dip direction and dip	Measured dip direction and dip of the structure.
Structure type	The abbreviations for structure types according to Tab. 2-2 are entered into the paper template.
Length of structure	The length of the long axis of the intersection ellipse is measured for structures which cut the core axis at acute angles (dipping with more than about 70°) and structures which do not cut through the entire core diameter. The measured length will be used for the calculation of fracture density P32. Measurements are required to reduce the inaccuracy resulting from calculating fracture areas solely from the angle between the structure and the core axis.
Azimuth and plunge of lineations	Measured dip azimuth and plunge of the lineation observed on the measured plane.
Shear sense and quality	Shear sense of fault planes and shear bands using up (reverse fault), down (normal fault), dex (dextral strike slip) or sin (sinistral strike slip), and reliability indicators (good, fair, poor) of the shear sense observation.
Mineralisation / fault rock type	Any type of filling, mineralisation or fault rock associated with the structure (e.g. CC for calcite of a vein filling, synCC for mineralisation of slickenfibres).

Tab. 2-3: continued

Parameter	**Definition of parameters and procedure for defining parameters**
Open / closed and width / length of open structures	Information on whether a tension gash / vein is open (displaying a continuous aperture), partly open (displaying a discontinuous aperture) or closed at the observation scale (i.e. the naked eye), including the width of the aperture and the observed lengths of open streaks for partly open structures.
Roughness	Roughness classification of a structure using the joint roughness coefficient (JRC). The JRC gives a picture of the classification of fracture smoothness and waviness (planarity) along 10 cm length of the fracture (Barton 1976, Barton & Choubey 1977). The scale of the JRC is from 0 (very smooth and planar) to 20 (very rough and wavy).
Fracture condition	Specifies whether the core is broken naturally or artificially at the structure under consideration or intact. If it cannot be specified whether the break occurred naturally or artificially, broken should be used.
Fracture density class (FDC)	In cases where cores or parts of a core are heavily disintegrated and order cannot be restored, the density of natural fractures cannot be calculated accurately. Fracture density should be estimated using the classification scheme of Bauer et al. (2016): fracture density class 2 (spacing of fractures = 5 cm to 10 cm), fracture density class 3 (spacing of fractures = 1 cm to 5 cm) or fracture density class 4 (spacing of fractures < 1 cm).
Additional remarks	Offsets or displacements as well as crosscutting relations are documented under "remarks". Further remarks are e.g. karstification, the shape and length of the teeth of stylolites, alterations, recrystallisation phenomena or whether a structure is of synsedimentary origin.

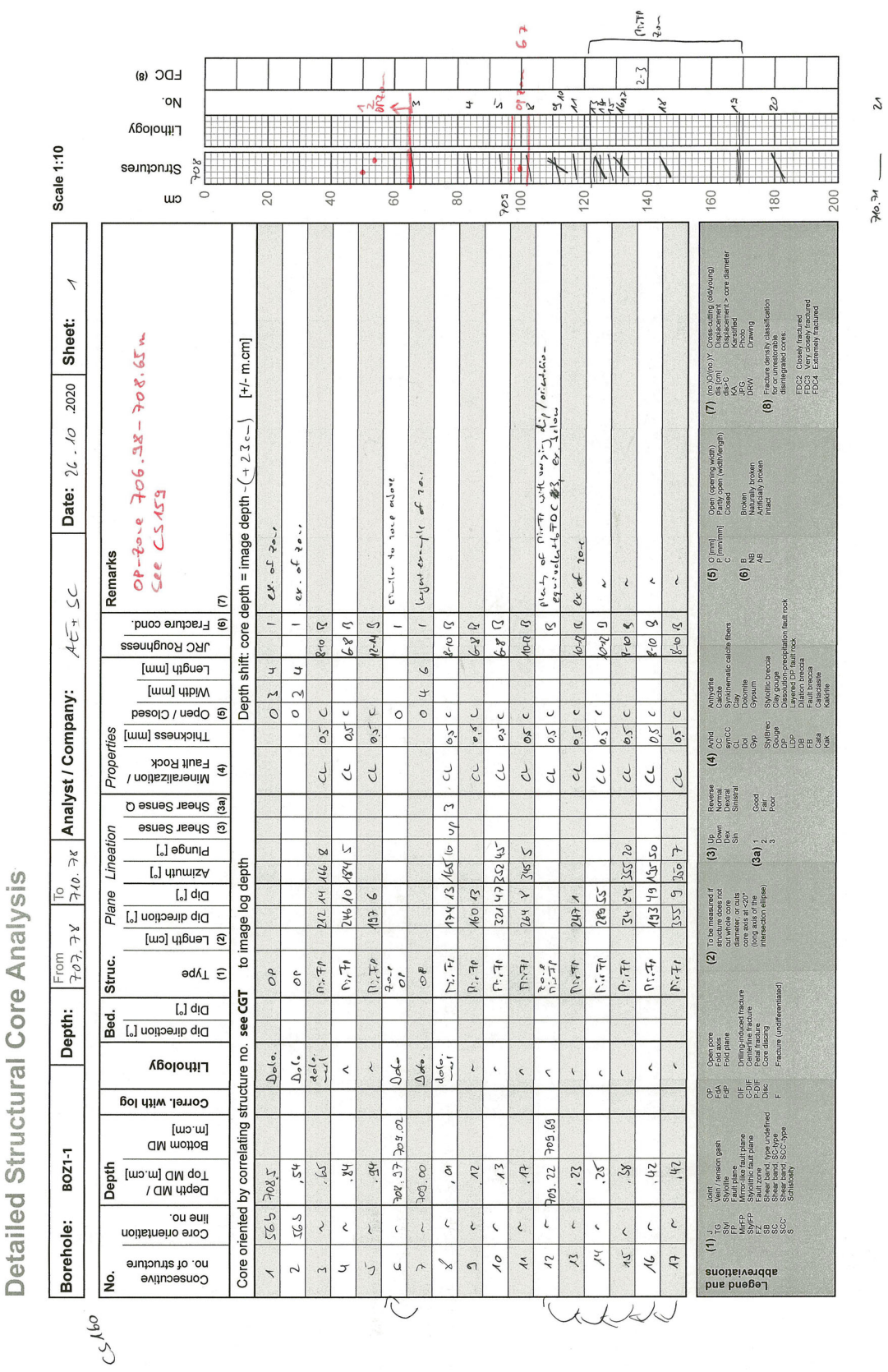


Fig. 2-10: Completed DIN A3 sheet of primary record of the detailed structural core analysis Example of core section 160 (707.78 m to 710.78 m MD core depth).

2.3 Geo-statistical evaluation

For the geo-statistical evaluation presented in Chapter 4, different structural tools and techniques were applied to analyse the available dip dataset. Most of the work was performed with TerraStation II (TERRASCIENCES, Inc.). This provides several advanced modules for the import, processing, visualisation and analysis of all types of available borehole data such as petrophysical logs, borehole images, core data and stratigraphic information.

For the structural evaluation of the different lithostratigraphic units and the different types of structural discontinuities, a series of figures was compiled:

- stereograms (Schmidt projection, lower hemisphere)
  - poles of the planes were displayed to examine the spatial orientation of bedding and structural planes
  - azimuth rose diagrams were compiled for planar features (bedding and fractures). The diagrams show the dip azimuth of the planes under consideration. The rose diagram is a circular histogram summarising orientation measurements. The radius of each segment of a rose diagram is proportional to the number of observations that occur within the angular range of that segment. Azimuth rose diagrams are displayed with cumulative petals, resulting in staked petals for different dip categories. For the directional statistics in Chapter 4 a minimum threshold of ten structures was set for the rose diagrams
- dip histograms visualise the dip angle distribution and clustering for a given dip dataset
- vector means for representative clusters of the different structure types were calculated in stereograms
- the vector azimuth plot (dip walkout plot) reflects the along-borehole dip variations and was compiled for bedding-related dips only (deformed dips and crossbedding were excluded). Here, the azimuth of a plane was plotted in a nose-to-tail fashion pointing in the direction of dip. The length of an interval is related to the number of dips and not to the thickness of lithostratigraphic units
- fracture density (P32 curves) reflects the fracture area per unit of rock volume (m^2/m^3). The algorithm computes the area of each fracture and creates a sum of the areas across the defined window of 1 m core length and steps of 0.1524 m. The lengths of subvertical fractures are incorporated whereas truncated parts of fractures are discarded. The computation of the area accounts for borehole ellipticity. The total area of fractures is then divided by the borehole volume (or volume of the rock mass) of the selected window. See Ebert & Decker (2019) and the literature therein for a more detailed discussion on P32 fracture density calculation. For this study, P32 fracture densities were calculated for all structural discontinuities as well as for each individual group:
  - fault planes, mirror-like fault planes and stylolitic fault planes
  - fractures, joints and tension gashes / veins
  - stylolites

The recorded kinematic indicators were analysed using TectonicsFP software. The available fault and kinematic data were plotted in the stereographic Angelier projection, with the symbols and colours reflecting the different shear senses (up, down, sinistral or dextral) and the observed shear sense reliability (good, moderate, poor). All Angelier plots in this report show corrected datasets, in which the data points of the lineations are projected onto the great circle of the corresponding fault plane, even if they have an angular offset of < 15°.

3 Inventory of structure types

The different structure types identified in the drill cores from BOZ1-1 and BOZ1-1B, and their relevant characteristics were described in Section 2.2. In this chapter, these structures are visualised with examples. The diameter of the cores in the following figures (Fig. 3-1 – 3-24) is 95 mm.

3.1 Examples of fault planes

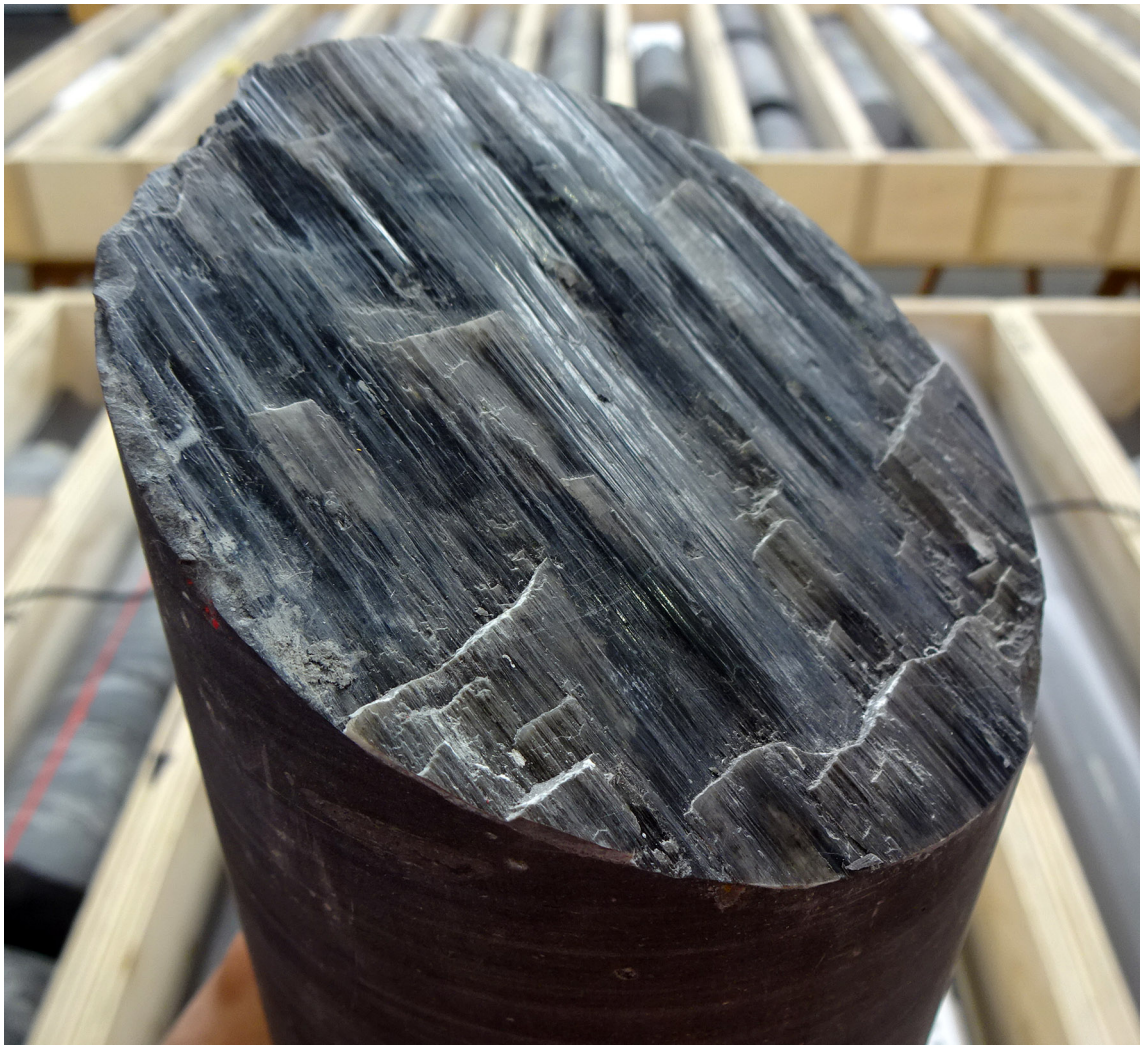


Fig. 3-1: Fault plane

Characteristics: Example of a fault plane with striation and mm-thick synkinematic calcite fibres. Shear sense is top up (reverse fault).

Formation: Wildegg Formation, depth: 401.06 m MD (core depth)

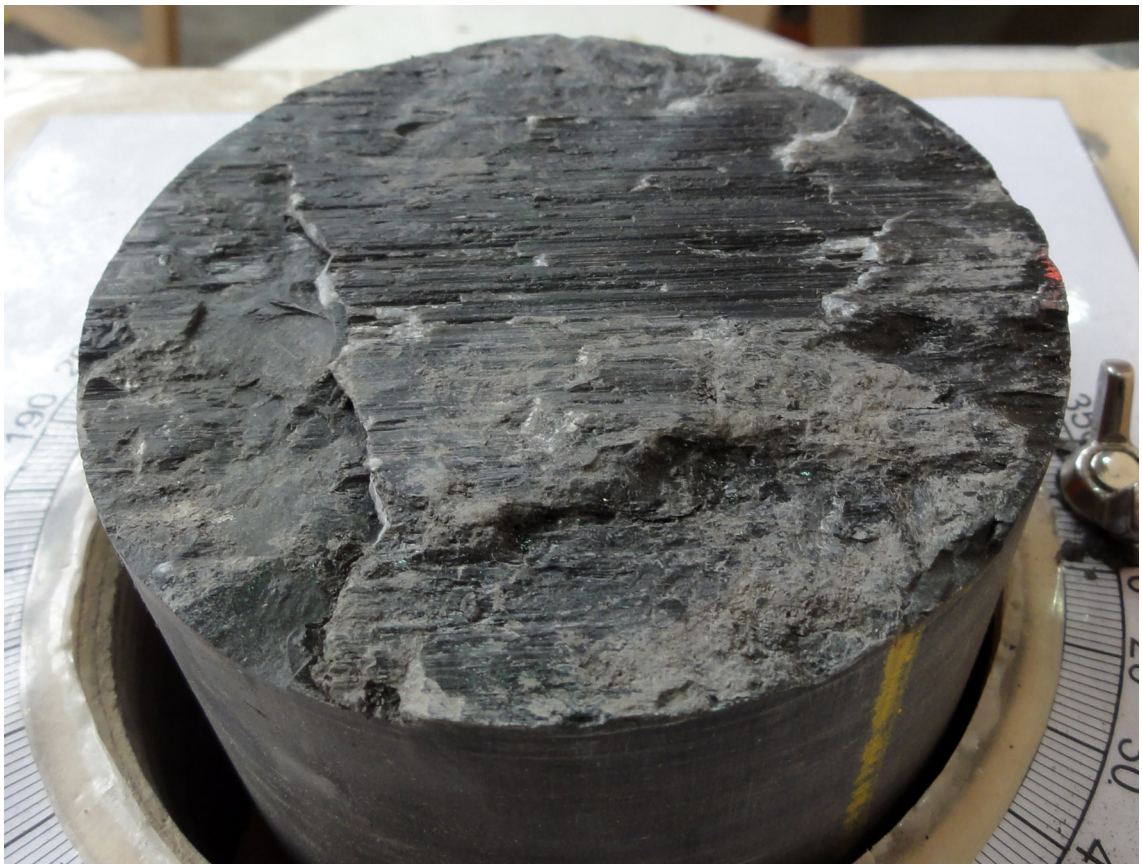


Fig. 3-2: Fault plane

Characteristics: Example of a subhorizontal fault plane with striation and mm-thick syn-kinematic calcite. Shear sense is top left (reverse fault).

Formation: Opalinus Clay, depth: 544.72 m MD (core depth)



Fig. 3-3: Fault plane

Characteristics: Example of a strike-slip fault. The striation shows a subhorizontal slip with a dextral shear sense (strike-slip fault). The photograph depicts the hanging wall of the fault.

Formation: Opalinus Clay, depth: 613.56 m MD (core depth)



Fig. 3-4: Mirror-like fault plane

Characteristics: Shallow and irregular fault plane with a polished, mirror-like slip surface and striation.

Formation: Klingnau Formation, depth: 437.81 m MD (core depth)



Fig. 3-5: Mirror-like fault plane

Characteristics: Example of a subhorizontal fault plane with a smooth mirror-like slip surface and striation.

Formation: Bänkerjoch Formation, depth: 804.41 m MD (core depth)



Fig. 3-6: Mirror-like fault plane

Characteristics: Example of a steeply dipping fault plane with a smooth mirror-like slip surface and subhorizontal striation.

Formation: Bänkerjoch Formation, depth: 742.01 m MD (core depth)

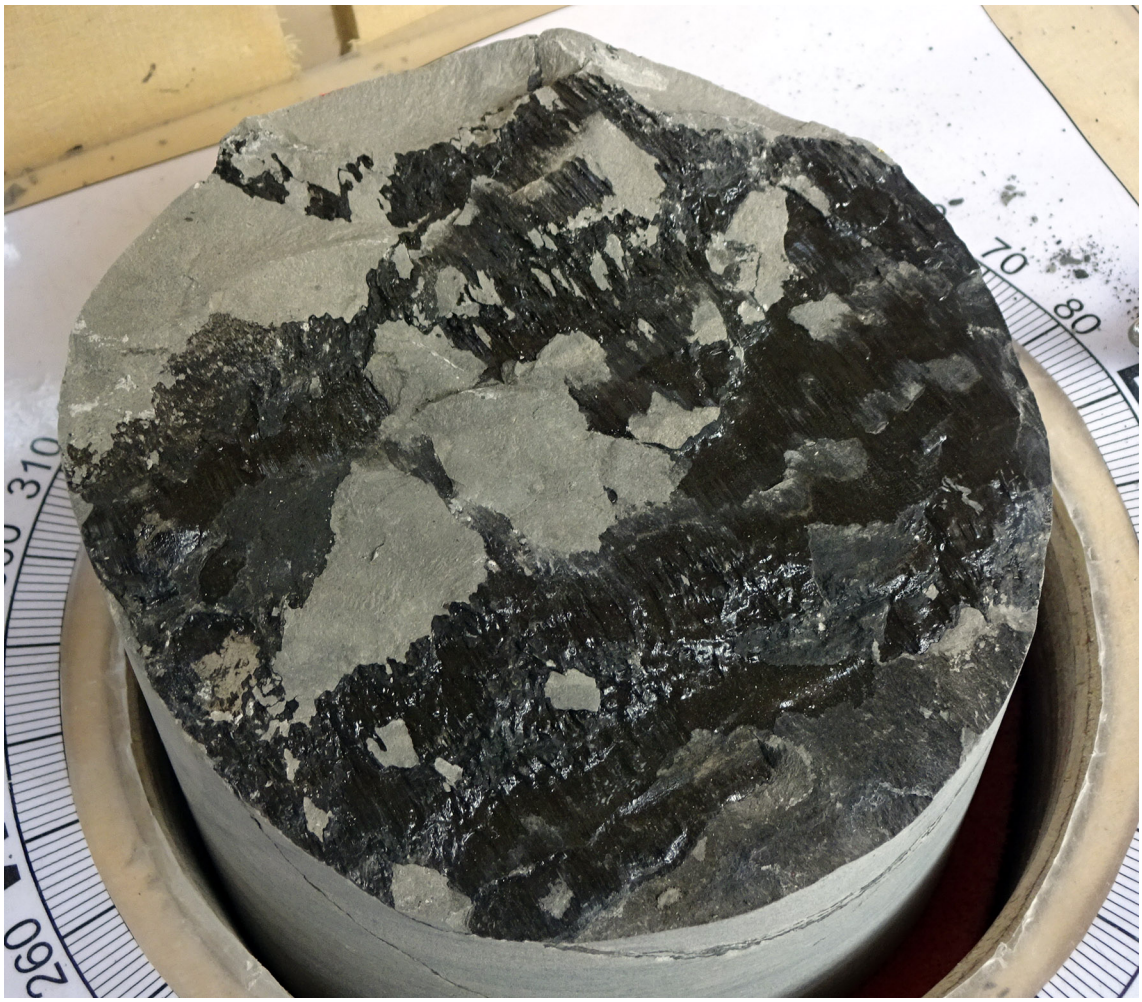


Fig. 3-7: Stylolitic fault plane

Characteristics: Example of a stylolitic fault plane with subhorizontal striation generated by carbonate dissolution and displacement subparallel to the plane.

Formation: Wildegg Formation, depth: 315.49 m MD (core depth)



Fig. 3-8: Stylolitic fault plane

Characteristics: Transition of a steeply dipping stylolite into a shallow dipping stylolitic fault plane with striation generated by carbonate dissolution and displacement subparallel to the plane.

Formation: Wildegg Formation, depth: 319.71 m MD (core depth)

3.2 Examples of fault zones

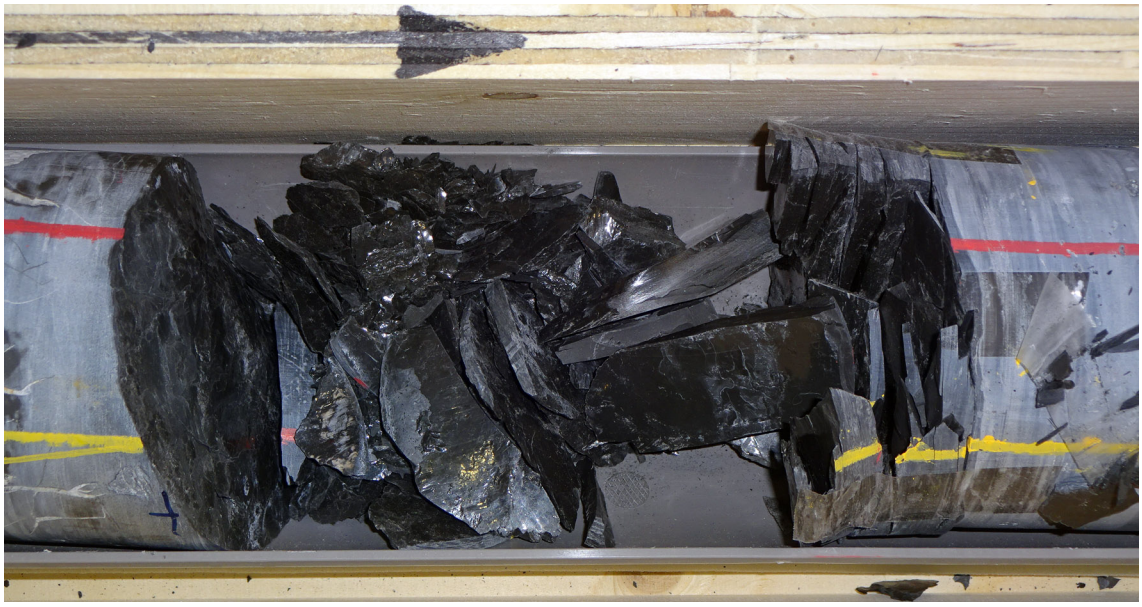


Fig. 3-9: Fault zone with FDC 3

Characteristics: Example of a fault zone with numerous individual and intersecting mirror-like fault planes. The core disintegration level corresponds to fracture density class 3.

Formation: Bänkerjoch Formation, depth: 720.25 m to 720.48 m MD (core depth)

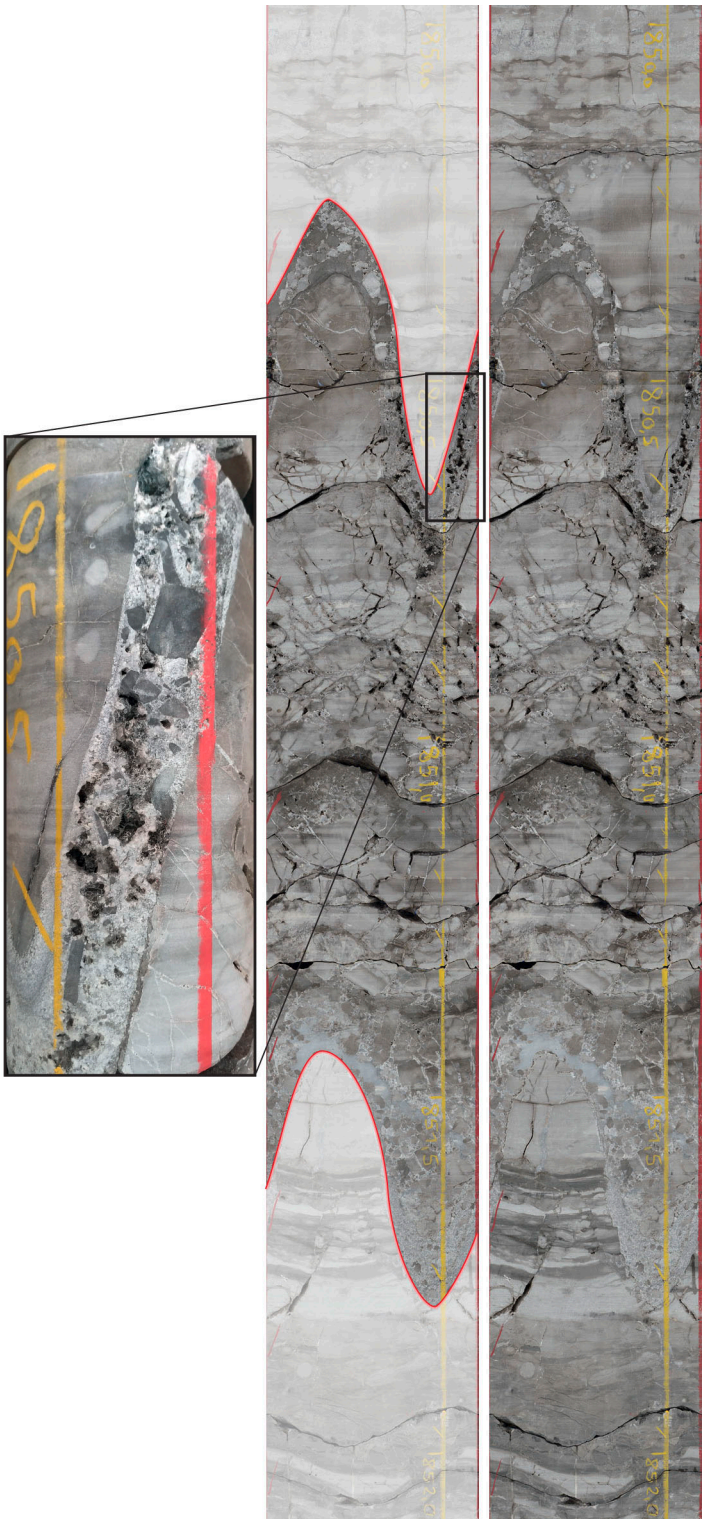


Fig. 3-10: Fault zone

Characteristics: Example of a fault zone with fault breccia and numerous fault planes with synkinematic calcite. The left image shows an example of a dilation breccia at the top of the fault zone.

Formation: Schinznach Formation, depth: 849.98 m to 852.09 m MD (core depth)



Fig. 3-11: Fault zone

Characteristics: Example of a fault zone with synkinematic calcite and fault breccia.

Formation: Bänkerjoch Formation, depth: 742.73 m to 742.79 m MD (core depth)

3.3 Examples of fractures / joints

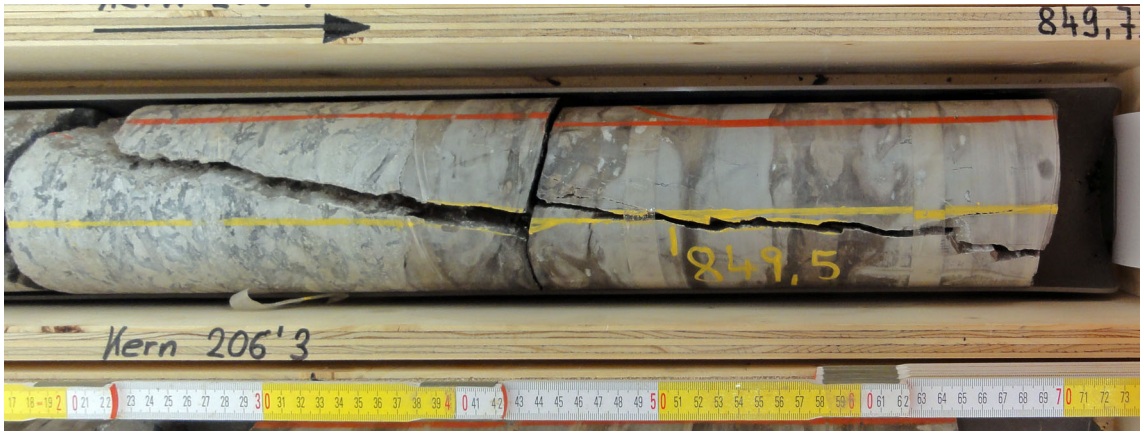


Fig. 3-12: Fracture

Characteristics: Example of a 50 cm long, subvertical extensional fracture.

Formation: Schinznach Formation, depth: 849.52 m MD (core depth)



Fig. 3-13: Fracture

Characteristics: Fracture surface of the fracture in Fig. 3-12 with rough surface and absence of slip indications.

Formation: Schinznach Formation, depth: 849.52 m MD (core depth)

3.4 Examples of veins / tension gashes

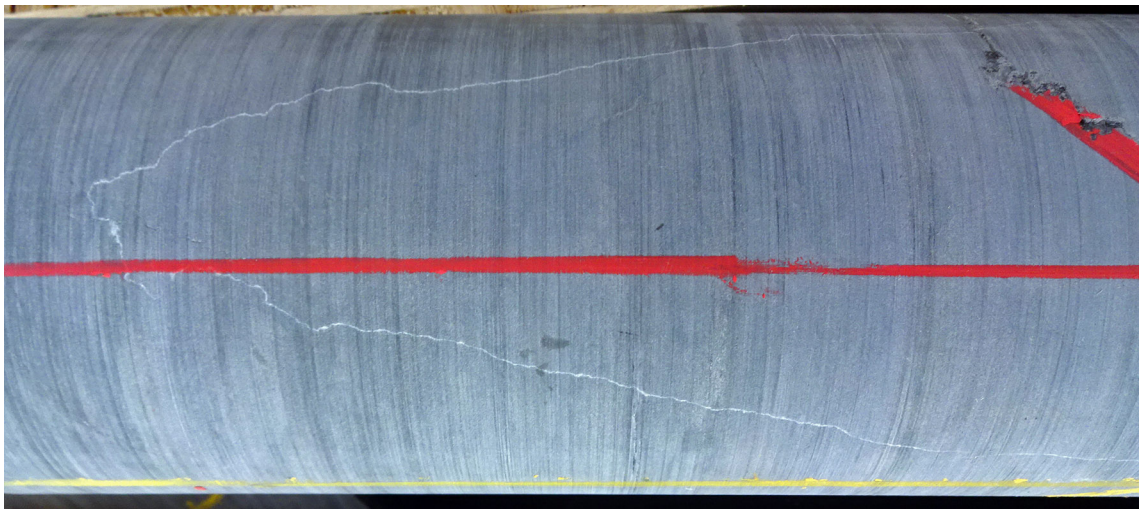


Fig. 3-14: Vein / tension gash

Characteristics: Example of a thin, subvertical calcite-filled tension gash.

Formation: Wildegg Formation, depth: 324.34 m MD (core depth)

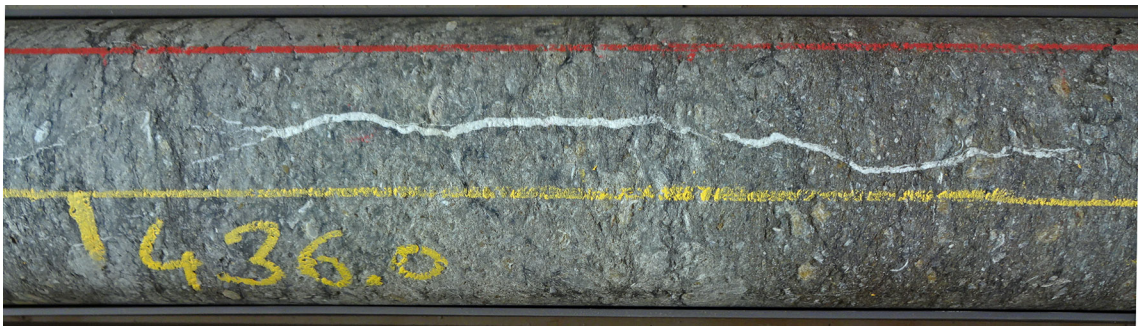


Fig. 3-15: Vein / tension gash

Characteristics: Example of a subvertical, several millimetres thick and undulating calcite tension gash.

Formation: Klingnau Formation, depth: 436.01 m MD (core depth)



Fig. 3-16: Vein / tension gash

Characteristics: Example of a tension gash filled with fibrous anhydrite.

Formation: Bänkerjoch Formation, depth: 747.82 m MD (core depth)

3.5 Examples of stylolites

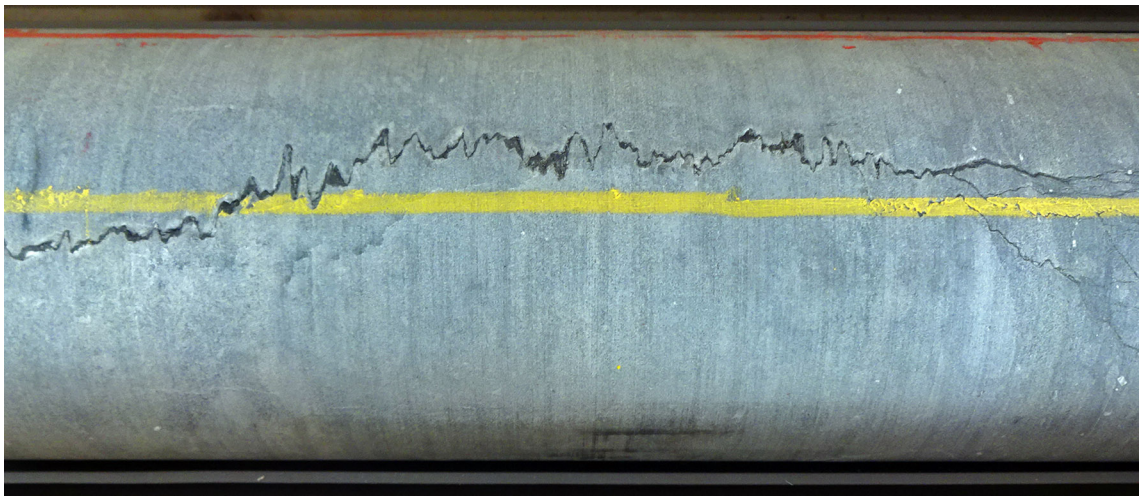


Fig. 3-17: Stylolite

Characteristics: Example of a subvertical stylolite with mm-long subhorizontal teeth.

Formation: Wildegg Formation, depth: 319.72 m MD (core depth)

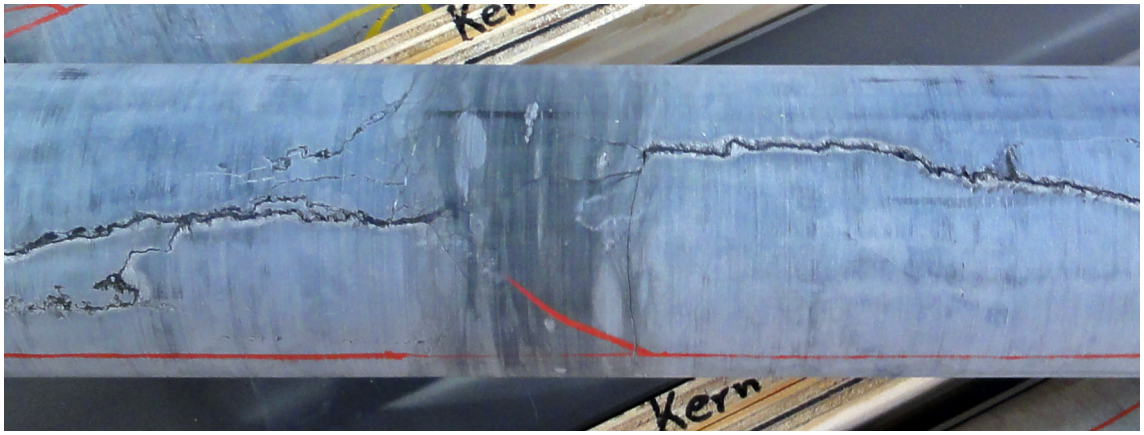


Fig. 3-18: Stylolite

Characteristics: Example of a subvertical stylolite.

Formation: Wildegg Formation, depth: 304.30 m MD (core depth)

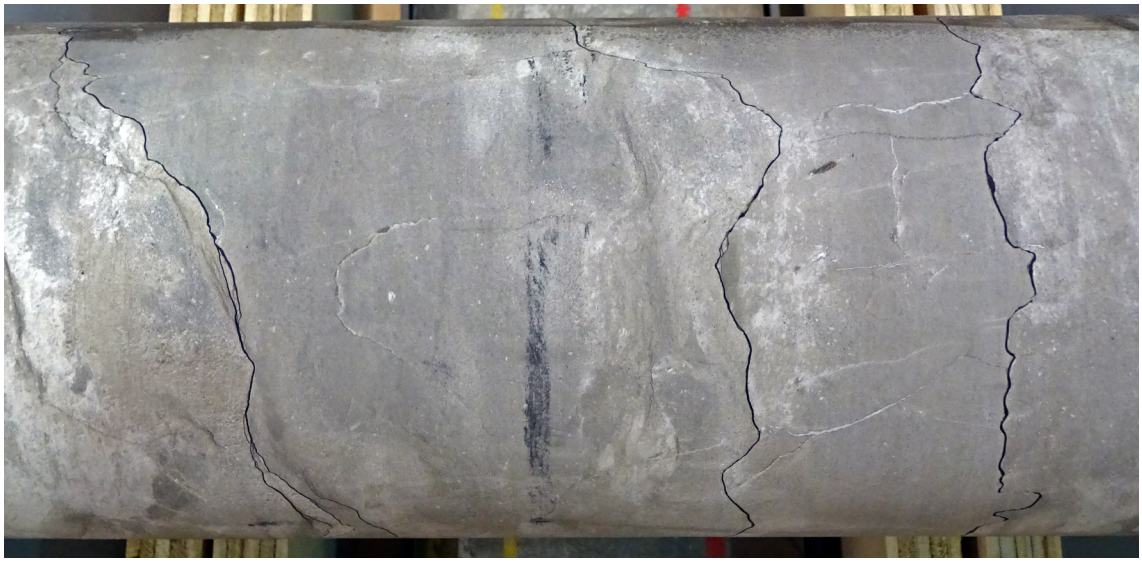


Fig. 3-19: Stylolites

Characteristics: Example of subhorizontal stylolites.

Formation: Schinznach Formation, depth: 835.71 m to 836.07 m MD (core depth)

3.6 Examples of open pores



Fig. 3-20: Open pores

Characteristics: Example of an open pore, 8 mm in diameter and idiomorphic calcite crystals.

Formation: Ifenthal Formation, depth: 407.95 m MD (core depth)

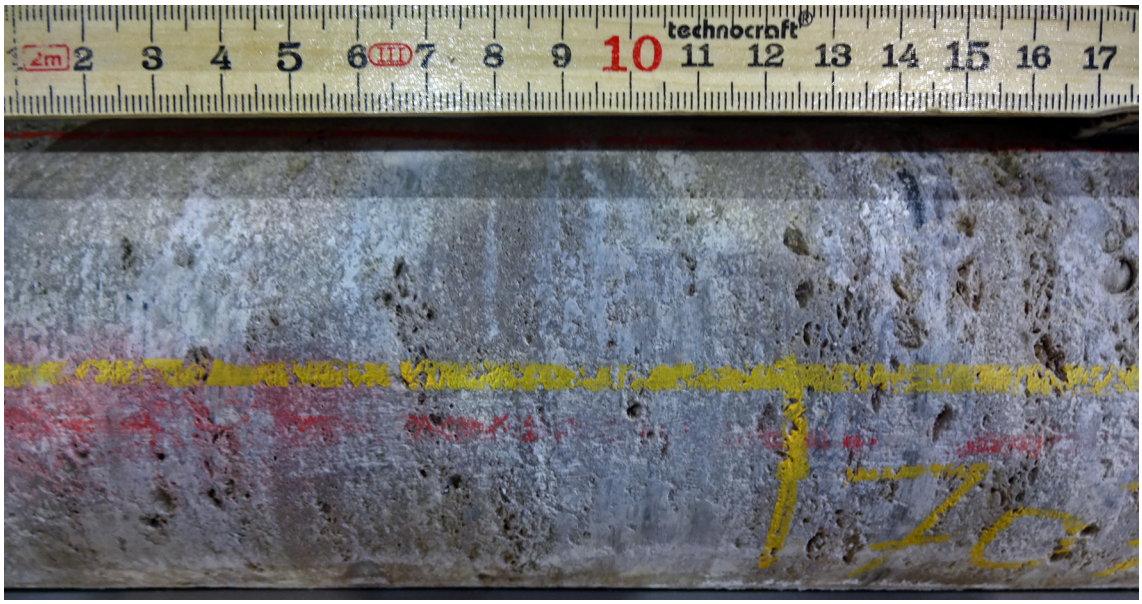


Fig. 3-21: Open pores

Characteristics: Example of small open pores in a layer typically found in the Triassic dolostone with a dense network of mm-sized pores devoid of mineralisation.

Formation: Klettgau Formation, depth: 706.87 m to 707.06 m MD (core depth)

3.7 Examples of drilling-induced fractures



Fig. 3-22: Petal fractures

Characteristics: Example of a petal fracture of a small, curved and broken core with dip azimuth to the E.

Formation: Schinznach Formation, depth: 875.48 m MD (core depth)



Fig. 3-23: Discing

Characteristics: Example of a discing structure in claystone, splitting the core into several discs with typical parallel fractures. Discs are oriented perpendicular to the core axis and (sub-)parallel to the bedding. Here, fracturing nucleated from the shell in the centre of the core as indicated by the plumose structure.

Formation: Opalinus Clay, depth: 607.67 m MD (core depth)

3.8 Examples of folding

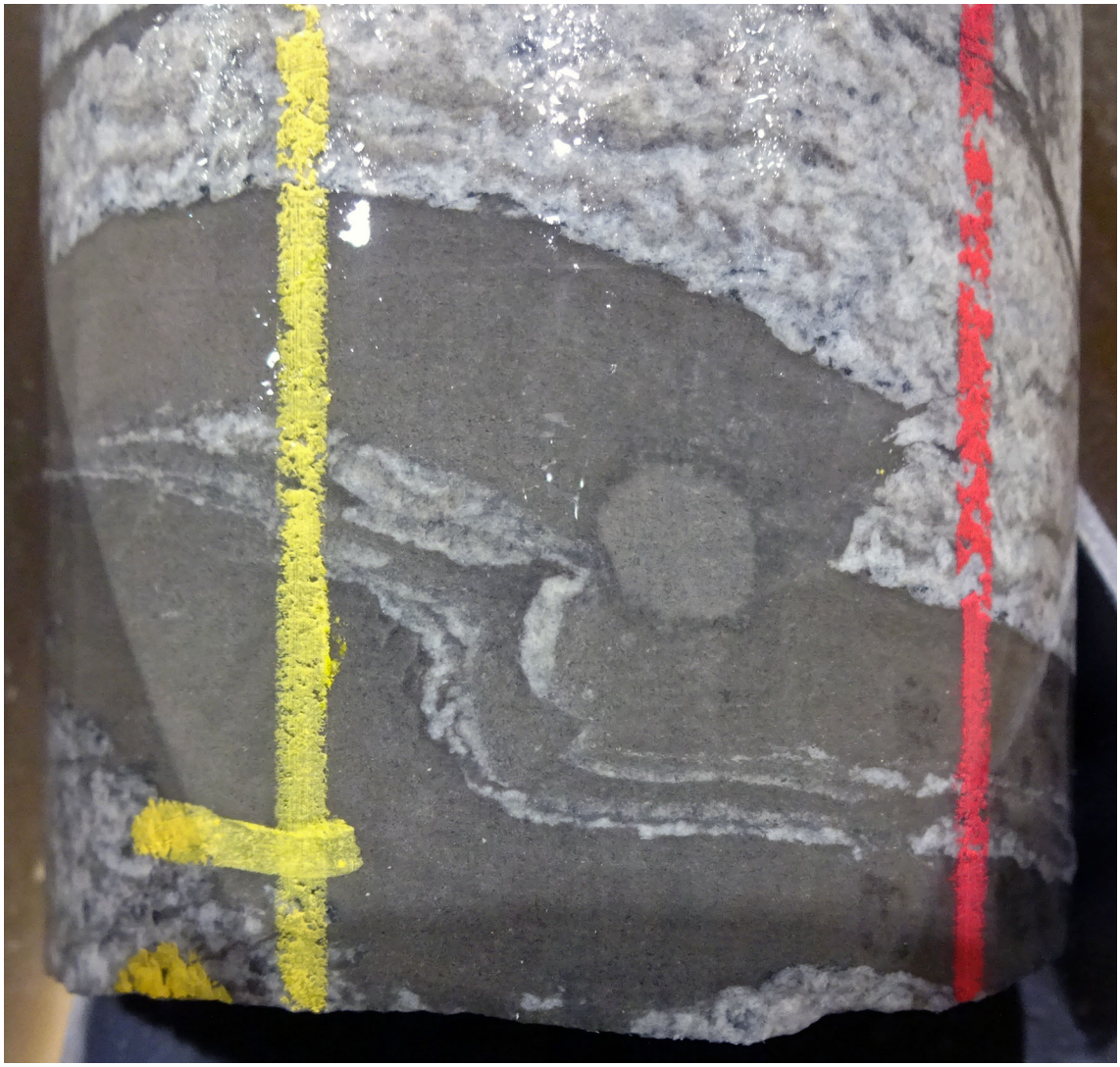


Fig. 3-24: Folding

Characteristics: Example of folded anhydrite / dolostone layers, most likely of synsedimentary origin.

Formation: Zeglingen Formation, depth: 921.97 m MD (core depth)

4 Geo-statistical evaluation: Results

Vector means of orientation values (dip direction and dip angle) of bedding planes and planar structural discontinuities were calculated for different data clusters in a stereographic projection (see Tab. 4-1). Bedding dips and structural discontinuities recorded in non-oriented cores (n = 74) were excluded from the following stereographic evaluation unless otherwise specified. However, they were included in the fracture density calculations (P32 curves) presented in Section 4.1.3.

Tab. 4-1: Vector means of orientation values for bedding planes and structural discontinuities (Azim: dip azimuth)

	Cluster 1 (main)			**Cluster 2 (subordinate)**			**Cluster 3 (subordinate)**		
	Azim	**Dip**	**No.**	**Azim**	**Dip**	**No.**	**Azim**	**Dip**	**No.**
Bedding	157	03	378						
Faults	175	05	733						
Tension gashes, joints, fractures	-	-	-						
Stylolites	164	09	209	178	74	165			

4.1 Entire cored borehole section (255.00 m to 1'037.31 m MD log depth)

A total of 3'649 individual planar and non-planar features were identified during the core analysis and manual dip picking of the 773.22 m of core material. They are visualised at different scales in the structural composite plots of Appendices B and C and are evaluated briefly below.

4.1.1 Basic structural dip evaluation

Bedding dips, particularly in lithologies of a plane-parallel nature such as in claystone, marl and siltstone sequences, are the best indicators for structural dip and its variation with depth. The dip variations along the current borehole are well reflected in the stereograms of Figs. 4-1 and 4-2 and in the vector azimuth plot in Fig. 4-3.

The studied borehole interval (255.00 m to 1'037.31 m MD log depth) ranging from the Malm to the Weitenau Formation reveals a subhorizontal to shallow (1° to 10º) structural dip with dip azimuth towards the NE, ESE, S, SE and SW; the overall mean structural dip is 157/03 [dip direction / dip angle] (n = 378; see Tab. 4-1). A number of local, abrupt changes in dip orientation were associated with evident faults / fault zones in the borehole, e.g. from 269.90 m to 271.23 m MD (log depth), from 688.54 m to 688.76 m MD (log depth) and from 850.27 m to 851.52 m MD (log depth). These dip changes are well reflected and highlighted in the dip azimuth vector plot of Fig. 4-3. Consequently, faulting may be considered as the main deformation mechanism controlling the structural dip in the current borehole.

Dip anomalies were also observed in the Opalinus Clay from 568.90 m to 572.00 m MD (log depth), from 600.70 m to 607.60 m MD (log depth) and from 623.90 m to 627.26 m MD (log depth). These borehole intervals are partly characterised by beds dipping up to 65° (deformed bedding, not visualised in the rose diagram of Fig. 4-2) and with variable dip directions and are most likely linked to soft-sediment deformation. However, a more detailed structural dip evaluation is beyond the scope of this study.

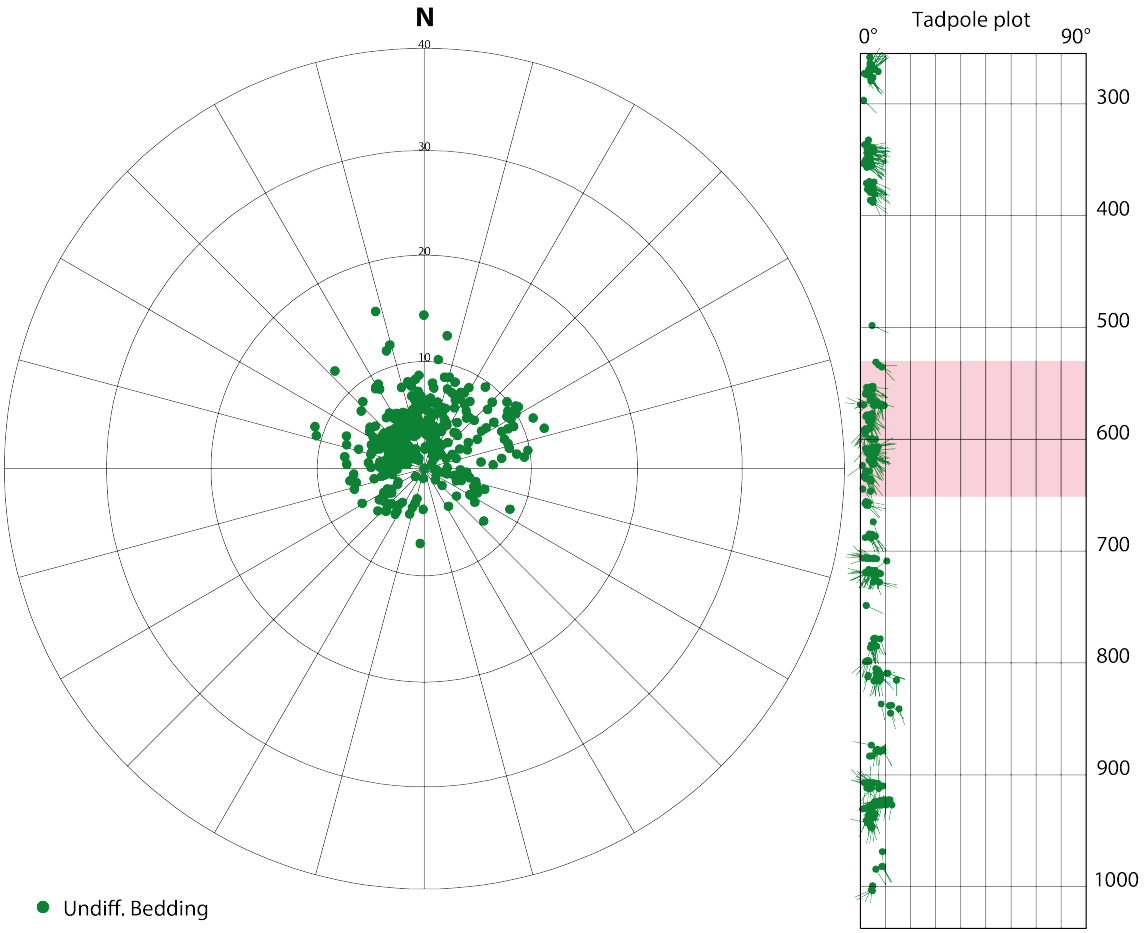


Fig. 4-1: Stereogram and depth plot for bedding planes (n = 411) for the entire cored borehole section

Note the predominance of 0° to 10° SE-directed dips with an overall mean of 157/03 (n = 378). Depth range is 255.00 m to 1'037.31 m MD (log depth). The Opalinus Clay interval is indicated by a red bar in the tadpole plot. The perimeter of the stereogram corresponds to 40° dip.

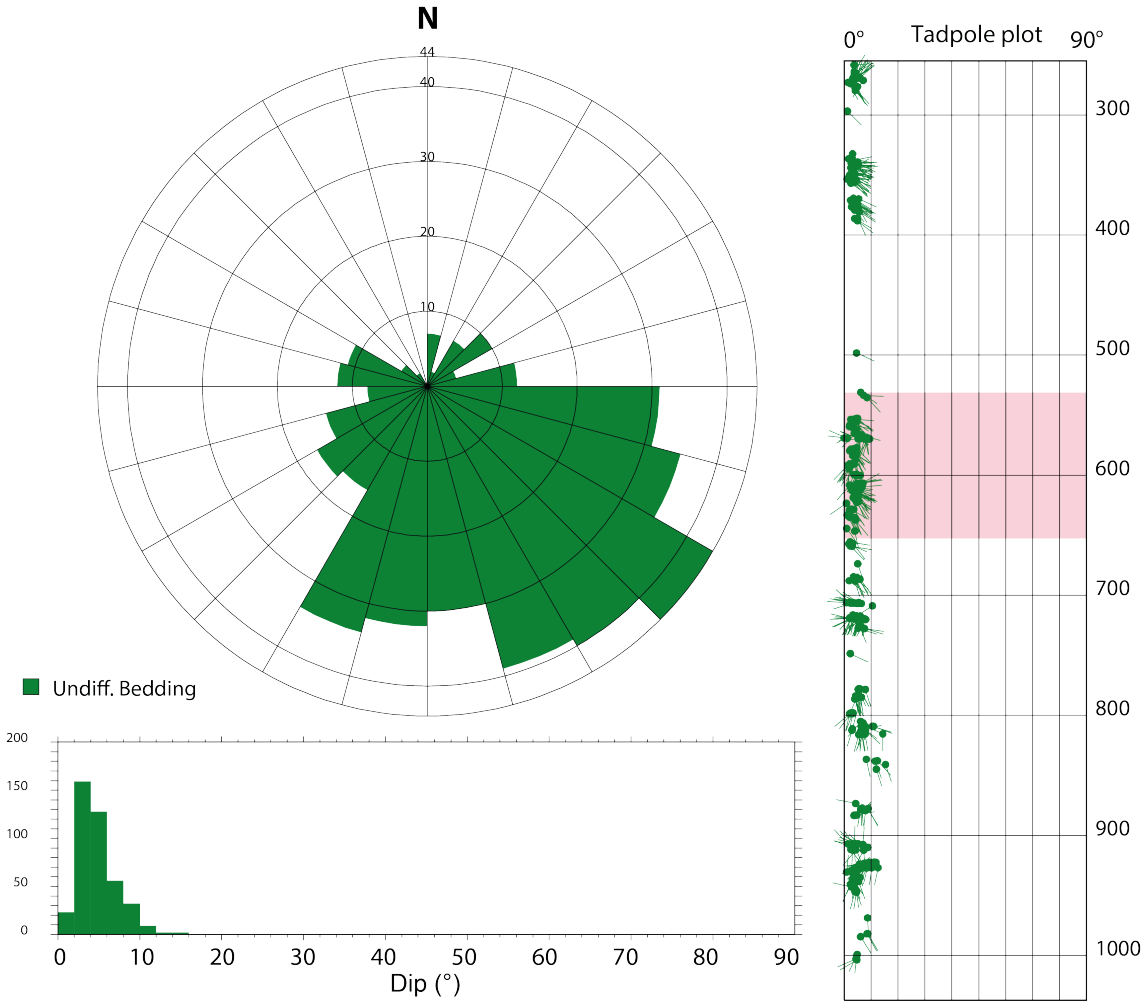


Fig. 4-2: Dip azimuth rose diagram, dip histogram and depth plot for bedding planes (n = 411) for the entire cored borehole section

Note the predominance of dip directions towards the SE. Depth range is 255.00 m to 1'037.31 m MD (log depth). The Opalinus Clay interval is indicated by a red bar in the tadpole plot.

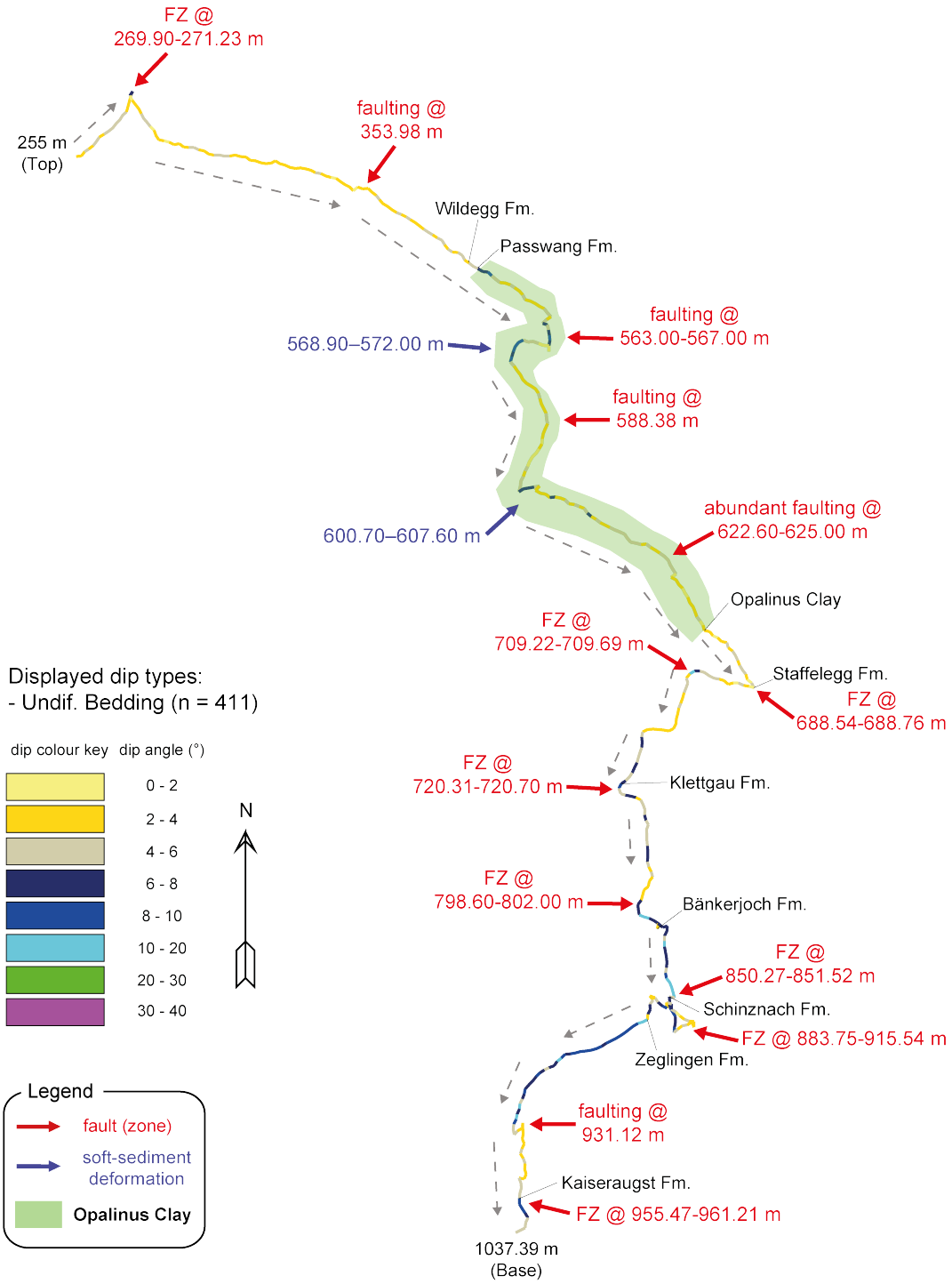


Fig. 4-3: Vector azimuth (or walkout) plot with bedding dips (n = 411) in oriented cores

The colour-coding reflects the dip angle. The horizontal distance has no meaning and only represents the number of bedding planes in the corresponding section. Grey arrows point in the direction of the overall dip direction. Lithostratigraphic formation boundaries (bottoms) are indicated as well as faults / fault zones (red arrows) and zones with possible soft-sediment deformation (blue arrows). The Opalinus Clay interval is shaded in green. Steeply dipping deformed bedding planes and those from non-oriented cores are excluded from this plot. Depths are given in metres MD (log depth).

4.1.2 Natural structural discontinuities

Fault planes

In total, 1'386 individual faults were recorded in the BOZ1-1 borehole and the BOZ1-1B sidetrack. Faults are planes of shear failure, i.e. planes with plane-parallel movement (Ebert & Decker 2019). Depending on their appearance in the drill core, three types of fault planes were distinguished: (1) fault planes (n = 424), (2) mirror-like fault planes (n = 885) and (3) stylolitic fault planes (n = 77). Out of all recorded faults, 1'351 (97%) were detected in oriented cores and are included in this evaluation.

Several structurally complex intervals along the BOZ1-1 borehole and the BOZ1-1B sidetrack were interpreted as fault zones. They are commonly associated with intense fracturing and high fracture densities. The different FDC are defined by Ebert & Decker (2019). In total, 30 individual fault zones were defined for the entire cored interval along with their FDC in some zones (see Tab. 4-2).

Faults are unevenly distributed along the borehole as shown in Fig. 4-4 and are discussed in more detail in Section 4.1.4. At certain depths faults are absent, whereas at other depths they occur as swarms with a large number of individual fault planes causing heavily fractured and disintegrated rock. Such fault zones and core intervals are described using FDC.

The orientations of all recorded faults are displayed in the stereograms of Figs. 4-5 and 4-6. Faults show a scattered orientation with variable dip directions and dip angles ranging from horizontal to subvertical (1° to 90°). However, there is a predominance of bedding-subparallel and S- to SSE-dipping faults with an overall mean of 175/05 (n = 733; mean of selected cluster). Associated kinematic data could be defined on 814 fault planes out of 1'387 and are further evaluated in Section 4.1.4.

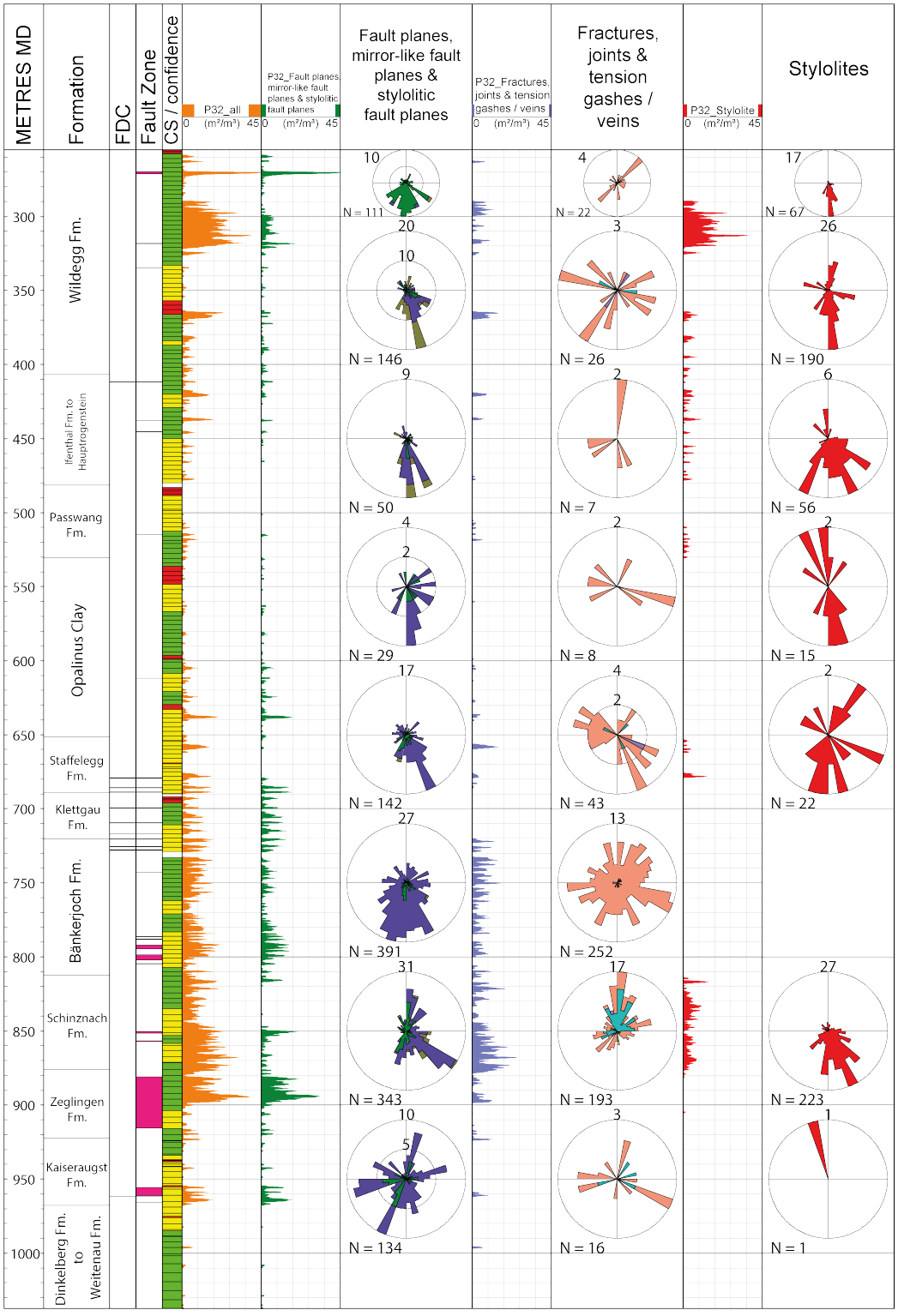


Fig. 4-4: Overview plot showing P32 fracture densities along the BOZ1-1 borehole and the BOZ1-1B sidetrack

In addition, a lithostratigraphic subdivision, core sections and goniometry confidence as well as fault zones associated with intense fracturing (described by FDC; see Tab. 4-2 below) are shown. Rose diagrams with the respective number of planes are displayed for 100 m intervals, except for the topmost diagrams which cover an interval of 45 m.

Tab. 4-2: List of interpreted fault zones, mirror-like fault plane (MirFP) zones and associated fracture density classes (FDC)

Fault zones				**FDC**
Top [m MD log depth]	**Bottom** [m MD log depth]	**Thickness** [m]	**Type**	**Type**
269.90	271.23	1.33	Fault zone	
318.31	318.56	0.25	Fault zone	
334.64	334.7	0.06	Fault zone	
411.66	411.69	0.03	MirFP zone	FDC2
437.78	437.90	0.12	Fault zone	
445.41	445.49	0.08	Fault zone	
515.01	515.07	0.06	MirFP zone	
611.71	611.80	0.09	Fault zone	
679.14	679.15	0.01	MirFP zone	FDC2
679.27	679.35	0.08	Fault zone	FDC3
685.65	685.97	0.32	Fault zone	FDC2
688.54	688.76	0.22	Fault zone	FDC2
699.23	699.45	0.22	MirFP zone	FDC2
709.22	709.69	0.47	MirFP zone	FDC3
716.73	716.75	0.02	Fault zone	FDC3
720.31	720.70	0.39	MirFP zone	FDC3
725.35	725.50	0.15	MirFP zone	
727.75	727.93	0.18	MirFP zone	FDC2
742.77	742.83	0.06	Fault zone	
786.11	786.52	0.41	MirFP zone	
787.97	788.03	0.06	MirFP zone	
792.16	794.66	2.5	MirFP zone	
798.60	802.00	3.4	Fault zone	
804.39	804.80	0.41	MirFP zone	
850.27	851.52	1.25	Fault zone	
856.51	857.19	0.68	Fault zone	
883.75	915.54	31.79	Fault zone	
955.47	961.21	5.74	MirFP zone	
961.83	961.89	0.06	MirFP zone	FDC2
965.58	965.71	0.13	MirFP zone	

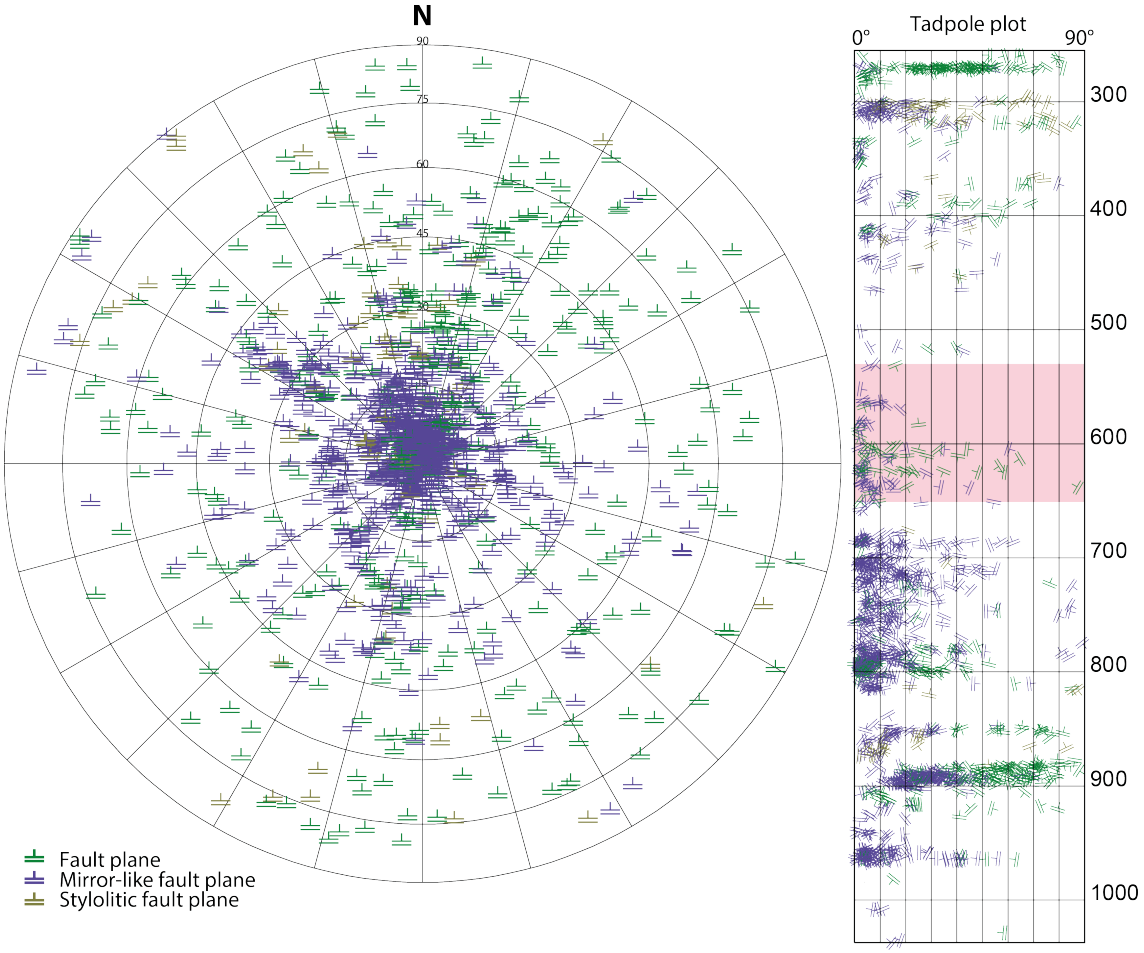


Fig. 4-5: Stereogram and depth plot of fault planes for the entire cored interval

A total of 1'351 fault planes in oriented cores are plotted: fault planes (n = 417), mirror-like fault planes (n = 857) and stylolitic fault planes (n = 77). Depth range is 255.00 m to 1'037.31 m MD (log depth). In the tadpole plot the Opalinus Clay interval is indicated by a red bar.

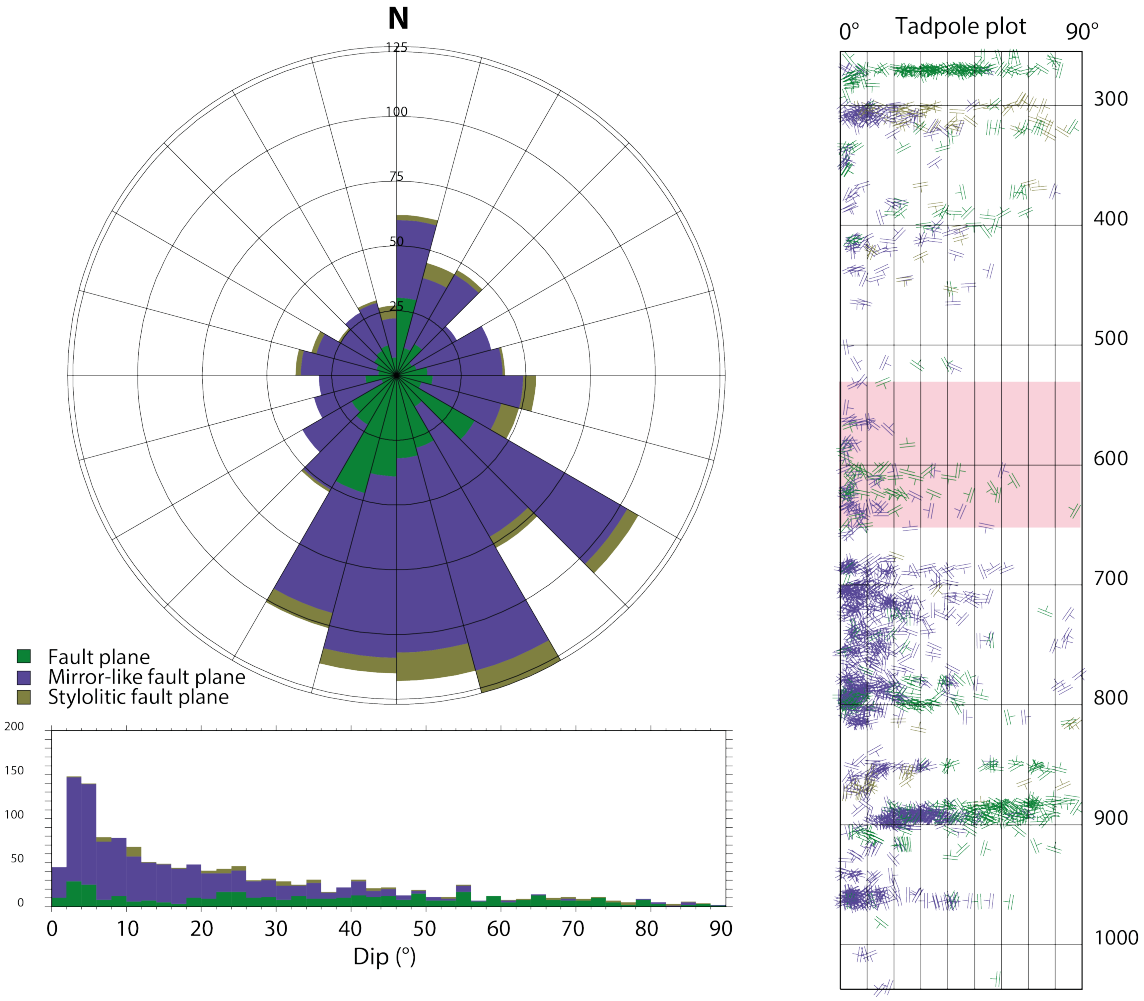


Fig. 4-6: Dip azimuth rose diagram, dip histogram and depth plot for fault planes in the entire cored interval

A total of 1'351 fault planes in oriented cores are plotted: fault planes (n = 417), mirror-like fault planes (n = 857) and stylolitic fault planes (n = 77). Depth range is 255.00 m to 1'037.31 m MD (log depth). In the tadpole plot the Opalinus Clay interval is indicated by a red bar.

Tension gashes / veins, joints and unassigned fractures

This group of structures represents extensional features without shear indicators and comprises tension gashes / veins (n = 455) and joints (n = 5). Fractures (n = 117) which could not be assigned to a specific class of structure are also included. With a total of 577 individual structures, they represent a smaller group of structural discontinuities than the fault planes. Out of these 577 structures, 567 (98%) planes were recorded in oriented cores.

The spatial distribution of tension gashes / veins, joints and unassigned fractures along the BOZ1-1 borehole and the BOZ1-1B sidetrack is presented in Fig. 4-4. Compared to faults, they reveal a considerable scatter in dip azimuth and dip as shown in Figs. 4-7 and 4-8.

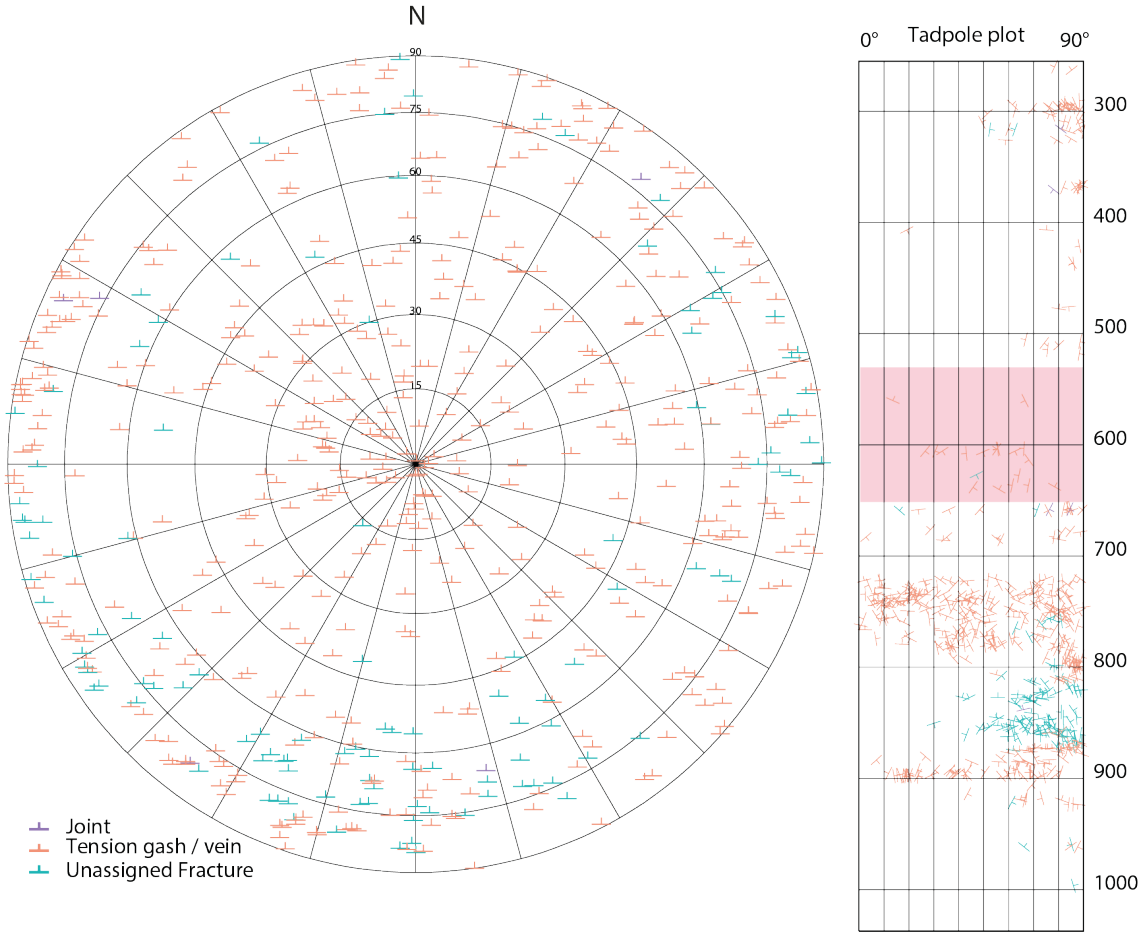


Fig. 4-7: Stereogram and depth plot for tension gashes / veins, unassigned fractures and joints in the entire cored interval

A total of 567 structures are displayed: tension gashes / veins (n = 445), joints (n = 5) and unassigned fractures (n = 117). Depth range is 255.00 m to 1'037.31 m MD (log depth). In the tadpole plot the Opalinus Clay interval is indicated by a red bar.

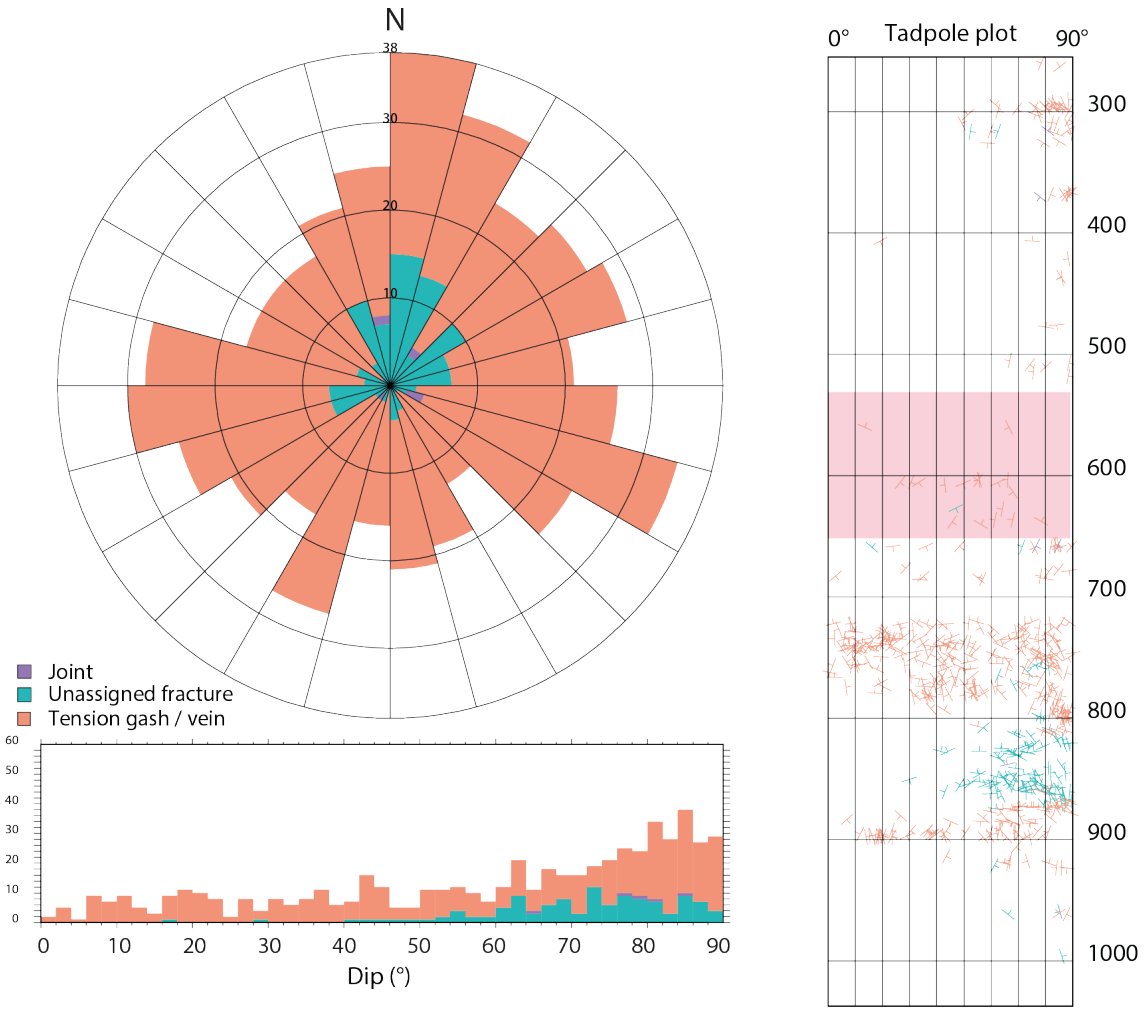


Fig. 4-8: Dip azimuth rose diagram of tension gashes / veins, unassigned fractures and joints in the entire cored interval

A total of 567 structures are displayed: tension gashes / veins (n = 445), joints (n = 5) and unassigned fractures (n = 117). Depth range is 255.00 m to 1'037.31 m MD (log depth). In the tadpole plot the Opalinus Clay interval is indicated by a red bar.

Stylolites

A total of 577 stylolites and six stylolite-rich zones were identified in the BOZ1-1 borehole and the BOZ1-1B sidetrack. Out of these, 574 (99%) were recorded in oriented cores. Particularly in stylolite-rich intervals such as the Malm and the Schinznach Formation (see Fig. 4-9), not all individual stylolites could be picked or documented, and only dominant stylolites clearly observed in core photographs were recorded and categorised. Intervals with high densities of stylolites were defined as stylolitic zones.

Stylolites show two well-developed orientation clusters (Figs. 4-9, 4-10 and Tab. 4-1): a sub-horizontal to shallow (1° to 25°) S- to SSE-dipping cluster (overall mean: 164/09; n = 209) and a steep to subvertical (50° to 90°) cluster with dip directions towards the S (overall mean: 178/74; n = 165).

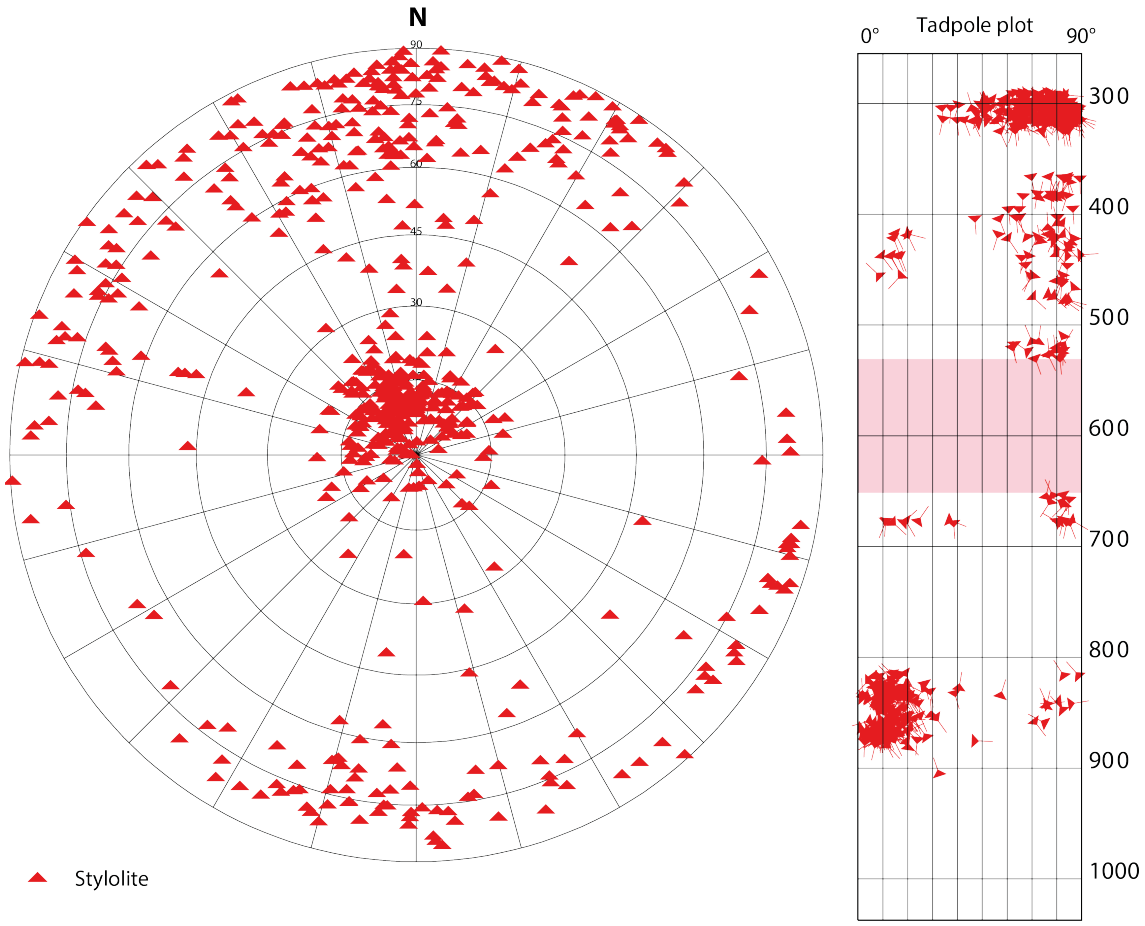


Fig. 4-9: Stereogram and depth plot for stylolites (n = 574) along the cored BOZ1-1 borehole and BOZ1-1B sidetrack

Depth range is 255.00 m to 1'037.31 m MD (log depth). In the tadpole plot the Opalinus Clay interval is indicated by a red bar.

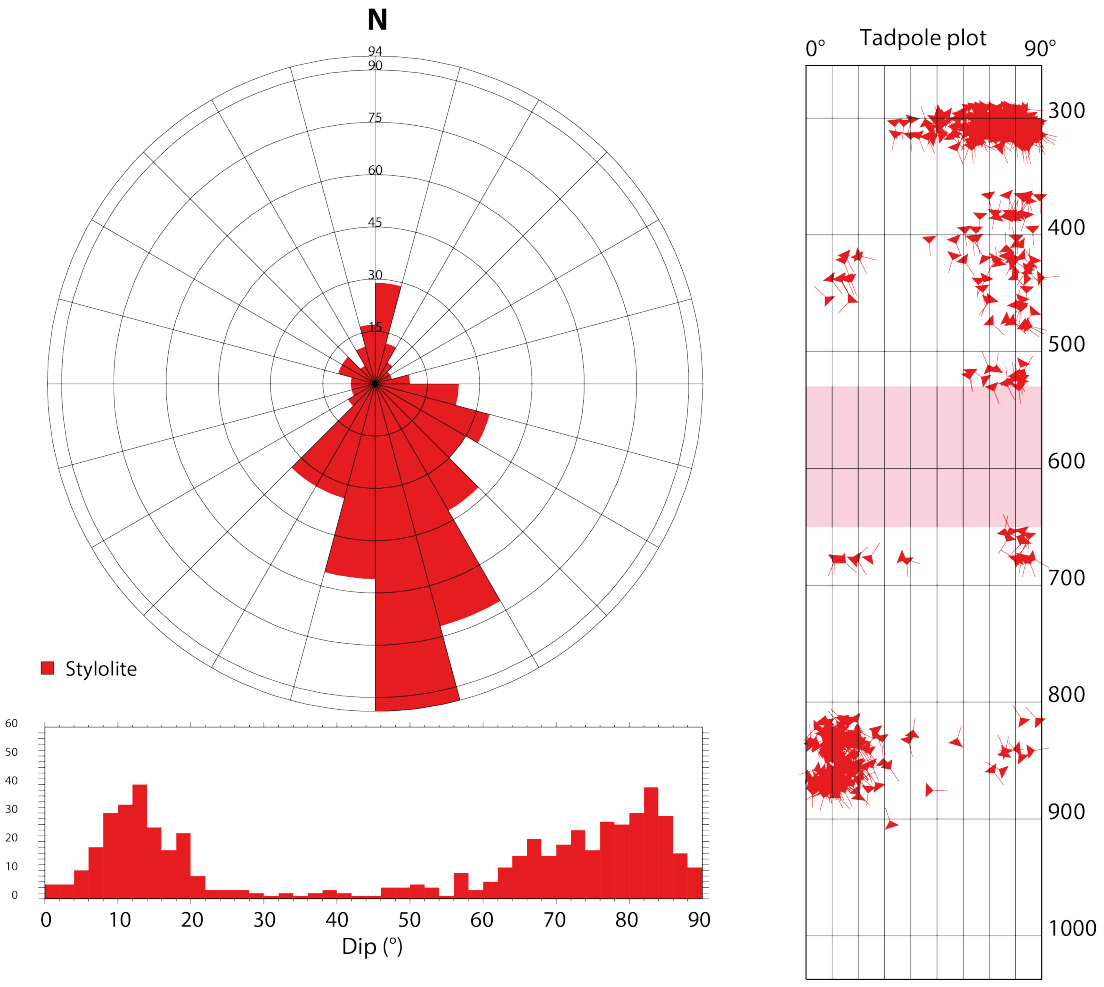


Fig. 4-10: Dip azimuth rose diagram and depth plot for stylolites in the entire cored interval

Depth range is 255.00 m to 1'037.31 m MD (log depth), n = 574. In the tadpole plot the Opalinus Clay interval is indicated by a red bar.

4.1.3 Fracture density (P32) and distribution

Density histograms were calculated in order to evaluate the spatial distribution of fractures (see Fig. 4-4). As mentioned above, structures recorded in non-oriented cores (n = 74) were considered in the fracture density calculations.

Fault planes were unevenly distributed along the cored interval. Higher fault counts were present particularly within the lower borehole interval from 680 m to 900 m MD (log depth) covering the lowermost Staffelegg Formation, the entire Keuper and the Muschelkalk down to the middle of the Zeglingen Formation. However, the highest density of fault planes with up to 47 planes per metre was observed within the fault zones in the Wildegg Formation from 269.90 m to 271.23 m MD (log depth) and in the Zeglingen Formation from 881.05 m to 922.30 m MD (log depth). Abundant faults commonly form prominent fault zones associated with intensely fractured and partly disintegrated drill cores (FDC 2 - 3; see Tab. 4-2 and Fig. 4-4). However, the average density of fault planes for the entire cored borehole section was 2.0 planes per metre.

Tension gashes / veins, joints and unassigned fractures are particularly abundant from approximately 720 m to 900 m MD (log depth) within the Bänkerjoch Formation, the Schinznach Formation and the Zeglingen Formation (see Fig. 4-4). The highest density (with up to 26 structures per metre) was encountered within the lowermost Schinznach Formation from approximately 845 m to 880 m MD (log depth) where the subvertical fractures form a distinct, open fracture zone. The average fracture density for the entire cored borehole section was about 1.5 fractures per metre.

Stylolites reveal an uneven distribution along the borehole and occur almost exclusively within the carbonate-rich lithologies of the Wildegg Formation from 290 m to 320 m MD (log depth) and in the Schinznach Formation from 815 m to 880 m MD (log depth). The highest density (with up to 38 stylolites per metre) was observed within the Wildegg Formation at 312.90 m MD (log depth). However, the average density for the entire borehole section was about 1.2 stylolites per metre.

4.1.4 Kinematic indicators

Striations could be measured on 814 fault planes. In total, 97% of the striations (n = 786) were collected in oriented cores. The orientations of the striations in oriented cores are given in Figs. 4-11 to 4-16. There is a clear predominance of S-dipping striations. The plunge of striations varies between subhorizontal to steep (1° to 50°). However, the vast majority does not exceed 10°.

Three different shear senses were distinguished for the analysed drill cores:

- up = thrusting / reverse faulting
- down = normal faulting
- dextral / sinistral = strike-slip faulting

A total of 230 shear indicators were identified as thrusts / reverse faults (Tab. 4-3), 43 faults were classified as normal faults and 23 faults were assigned to strike-slip faults. The majority of the recorded faults could not be assigned to a kinematic regime as no shear sense indicators were observed (n = 518, Tab. 4-3).

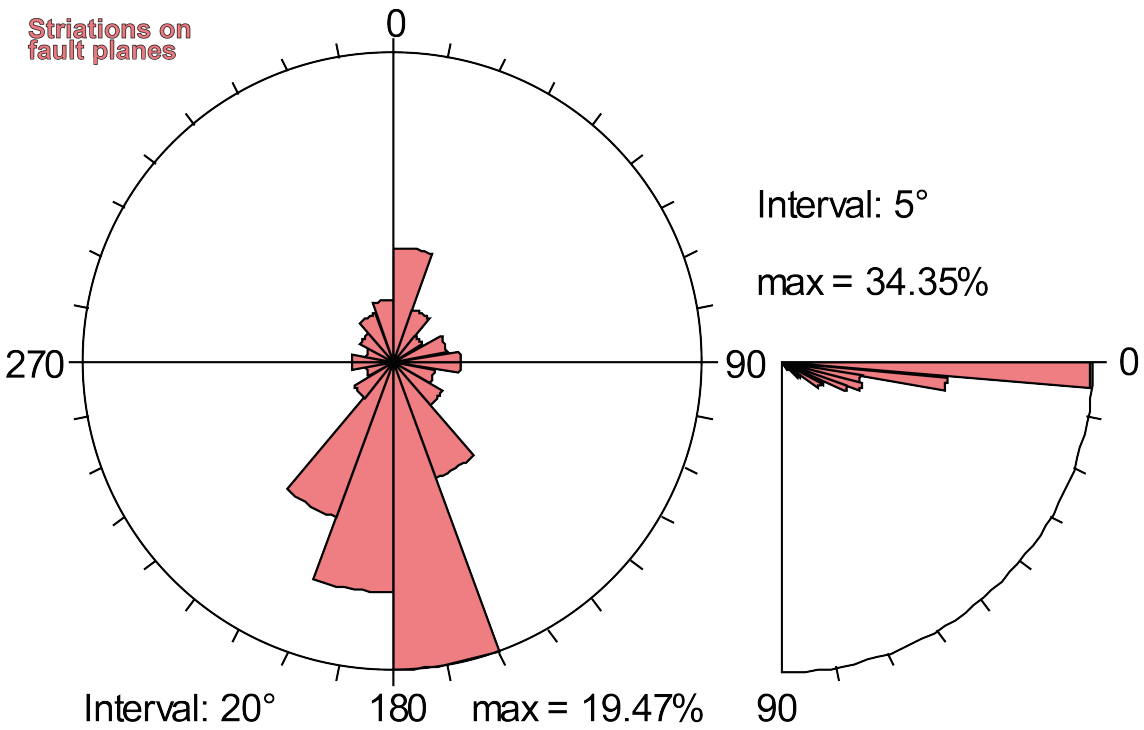


Fig. 4-11: Plunge azimuth of striations along fault planes in the entire cored interval

The striations (n = 786) from oriented cores of the entire core interval from the Malm to the Permian are presented. Left: Plunge azimuth rose diagram, right: plunge histogram. Depth range is 255.00 m to 1'037.31 m MD (log depth).

Tab. 4-3: List of all kinematic indicators in oriented and non-oriented cores

Shear sense	**Number**
Up	230
Down	43
Sinistral	12
Dextral	11
Unknown	518

In oriented cores	786
In non-oriented cores	28

Total measured lineations	814

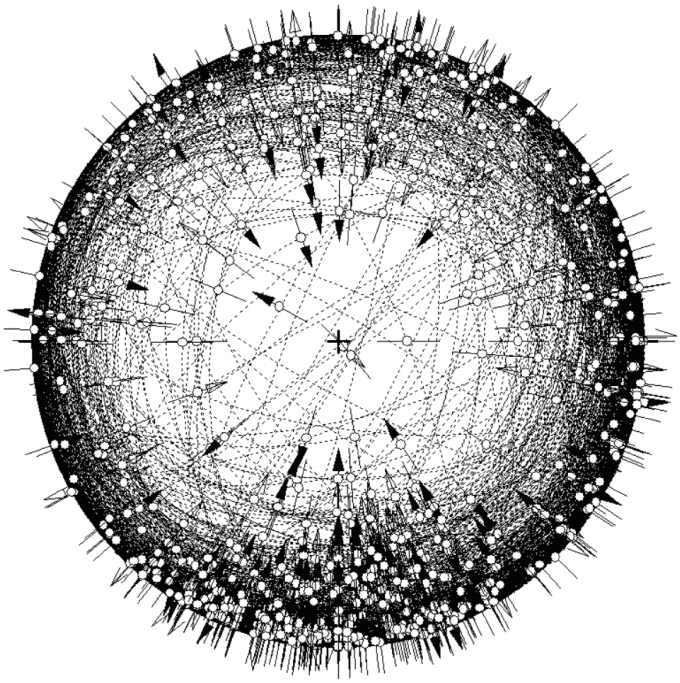


Fig. 4-12: Stereogram with striations on all oriented fault planes (including multiple lineations on a single fault plane) and associated kinematic data

Shear sense up (n = 223), down (n = 40), dextral (n = 10), sinistral (n = 10) and unknown (n = 503). Depth range is 255.00 m to 1'037.31 m MD (log depth).

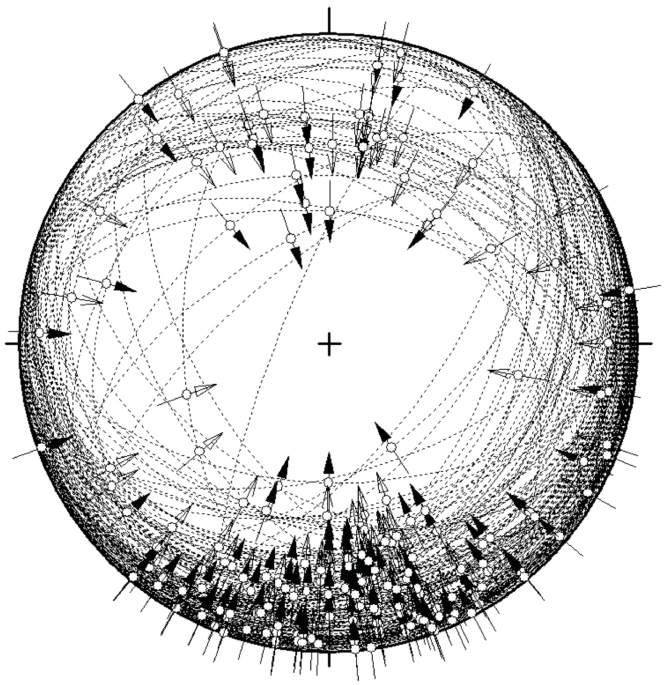


Fig. 4-13: Stereogram with all striations on oriented thrust / reverse fault planes (including multiple lineations on a single fault plane)

Shear sense up (n = 223). Depth range is 255.00 m to 1'037.31 m MD (log depth).

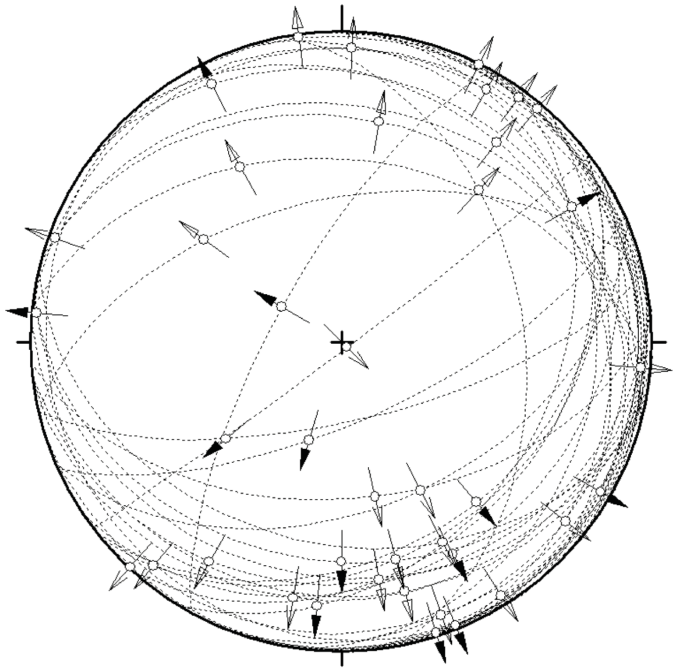


Fig. 4-14: Stereogram with all oriented normal fault planes (including multiple lineations on a single fault plane) and associated striations

Shear sense down (n = 40). Depth range is 255.00 m to 1'037.31 m MD (log depth).

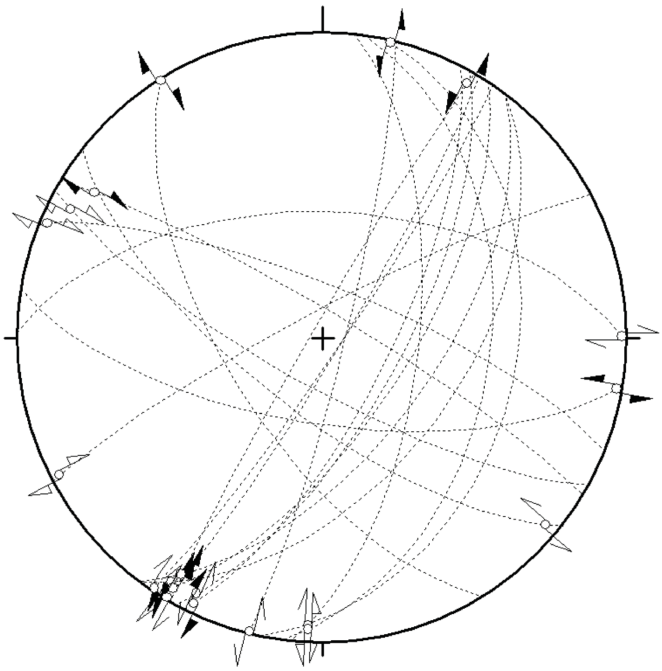


Fig. 4-15: Stereogram with all oriented strike-slip fault planes (including multiple lineations on a single fault plane) and associated striations

Shear sense dextral (n = 10) and sinistral (n = 10). Depth range is 255.00 m to 1'037.31 m MD (log depth).

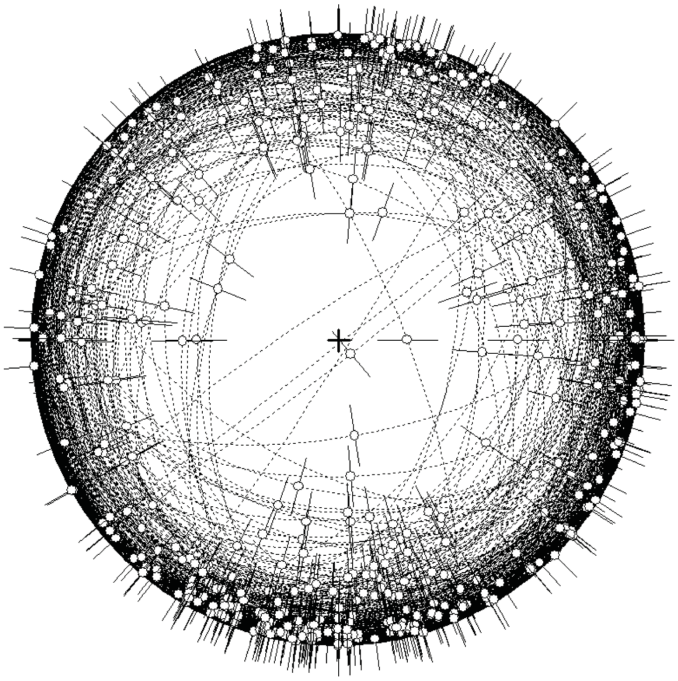


Fig. 4-16: Stereogram with all oriented fault planes (including multiple lineations on a single fault plane) with unknown shear sense

Shear sense unknown (n = 503). Depth range is 255.00 m to 1'037.31 m MD (log depth).

4.2 Malm

The cored Malm covers the interval from 255.00 m to 406.72 m MD log depth. For the detailed stereographic evaluation, only one lithostratigraphic unit (Wildegg Formation) was defined within the Malm interval. Only the data from oriented cores are presented.

4.2.1 Wildegg Formation

The orientation and spatial depth distribution of recorded structures in the Wildegg Formation (255.00 m to 406.72 m MD log depth) are shown in Figs. 4-17 to 4-23. The Wildegg Formation contains abundant fault planes and stylolites. The fault planes are generally distributed homogeneously. However, there are two zones with a higher density of fault planes from 269 m to 274 m MD (log depth) and from 299 m to 319 m MD (log depth). The fault planes show a varying dip with a preferred orientation towards the S. The stylolites show a higher concentration from 290 m to 325 m MD (log depth). They are generally steeply dipping with a dominant dip towards the S. Tension gashes and joints are rare, generally subvertical and have random orientations.

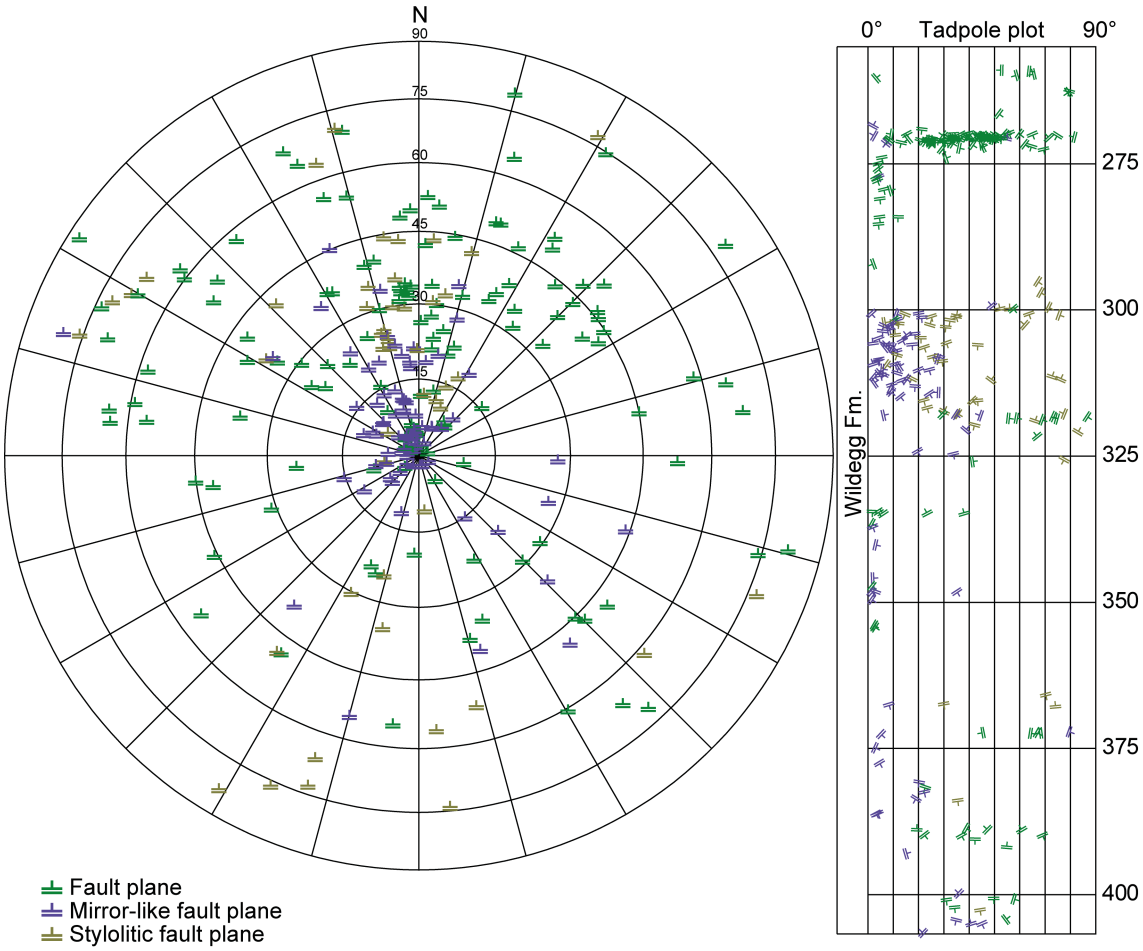


Fig. 4-17: Stereogram and depth plot of fault planes (Wildegg Formation)

Fault planes (n = 138), mirror-like fault planes (n = 82) and stylolitic fault planes (n = 47).

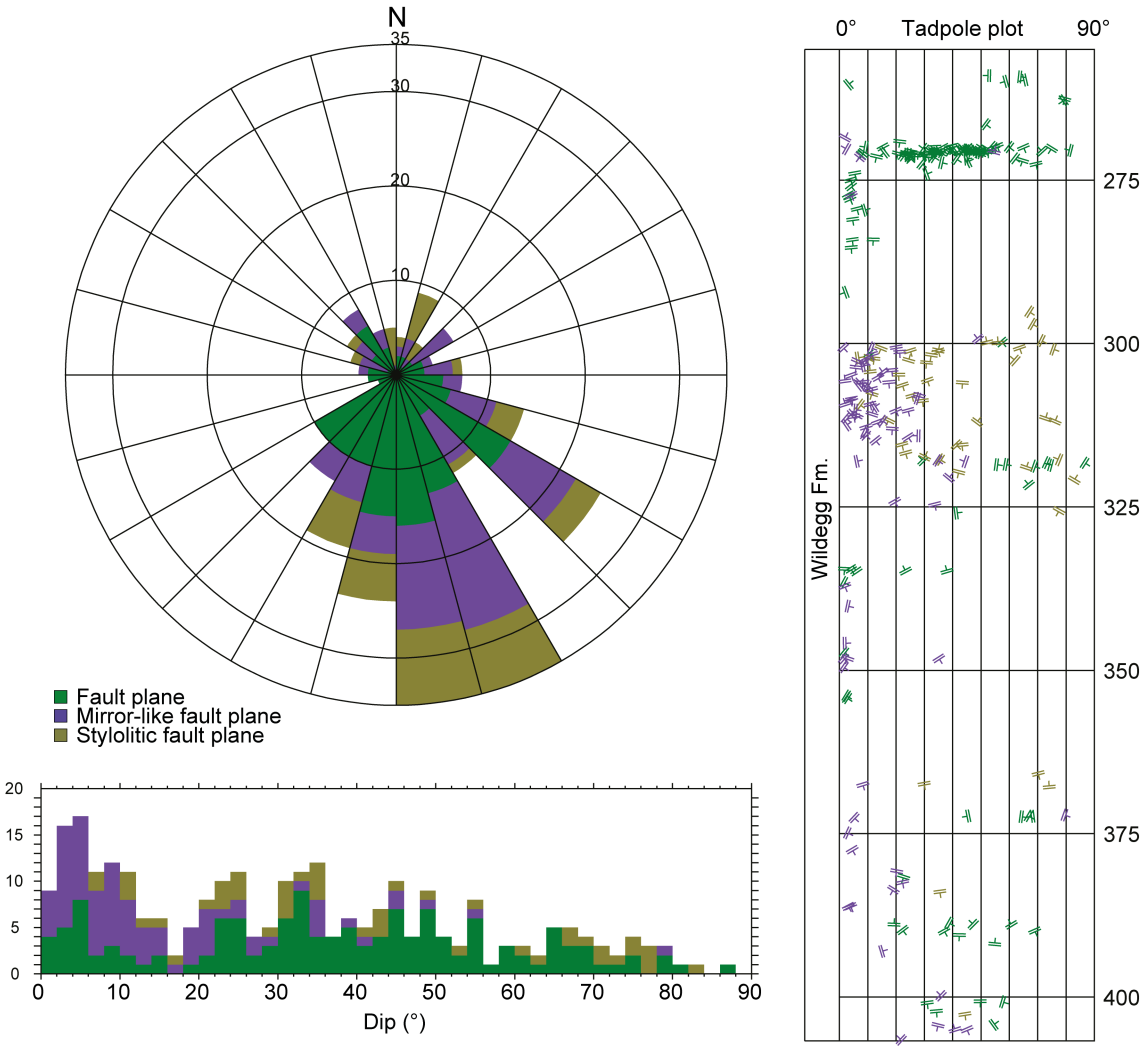


Fig. 4-18: Dip azimuth rose diagram, dip histogram and depth plot of fault planes (Wildegg Formation)

Fault planes (n = 138), mirror-like fault planes (n = 82) and stylolitic fault planes (n = 47).

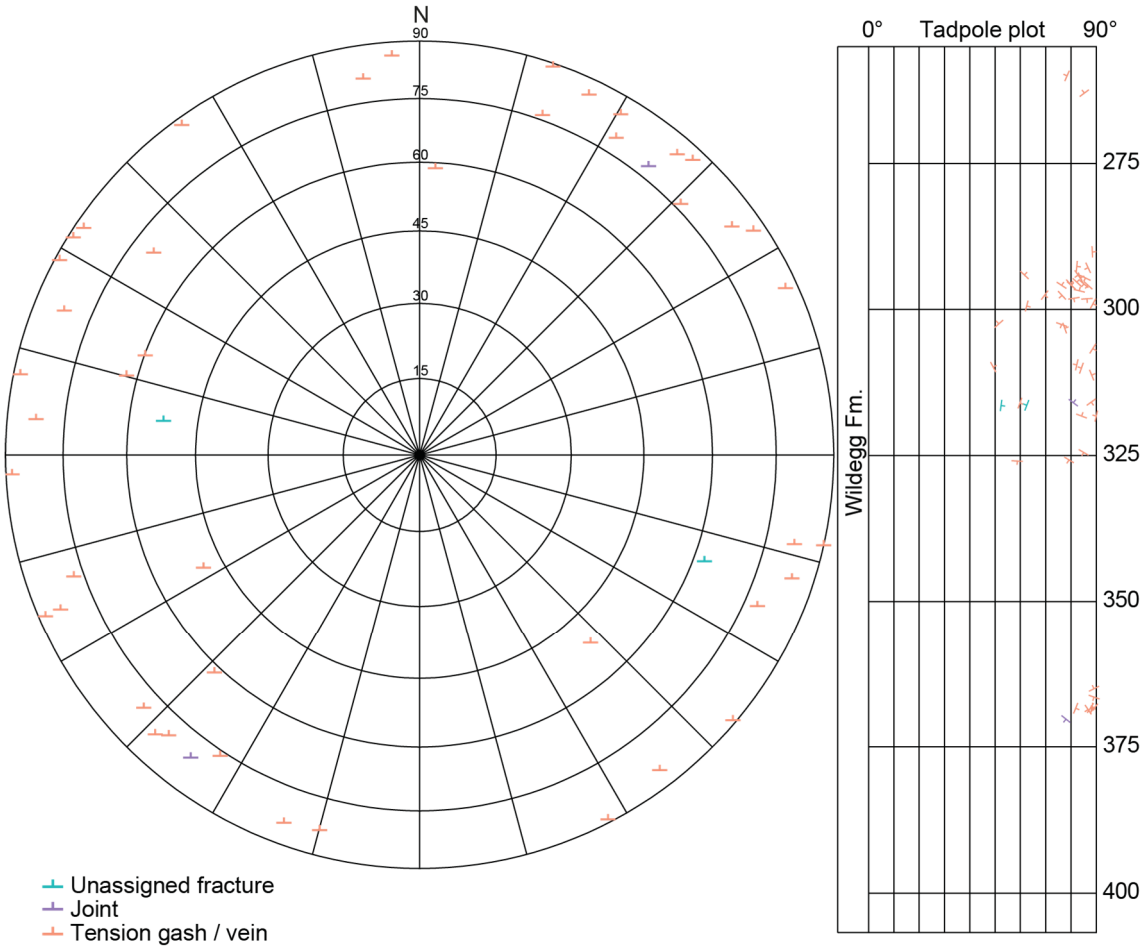


Fig. 4-19: Stereogram and depth plot of tension gashes / veins and unassigned fractures (Wildegg Formation)

Unassigned fractures (n = 2), joints (n = 2) and tension gashes / veins (n = 44).

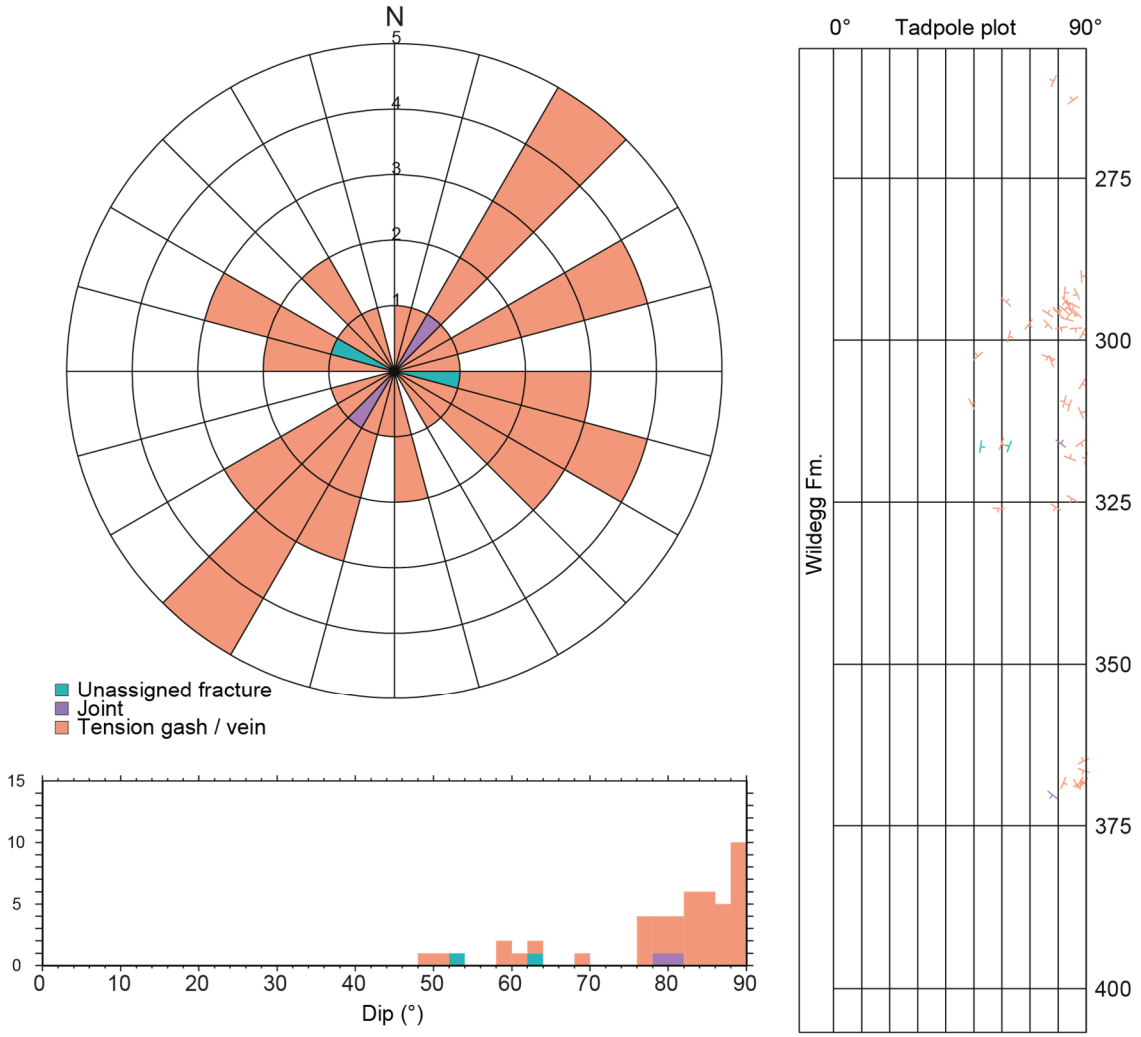


Fig. 4-20: Dip azimuth rose diagram, dip histogram and depth plot of tension gashes / veins, joints and unassigned fractures (Wildegg Formation)

Unassigned fractures (n = 2), joints (n = 2) and tension gashes / veins (n = 44).

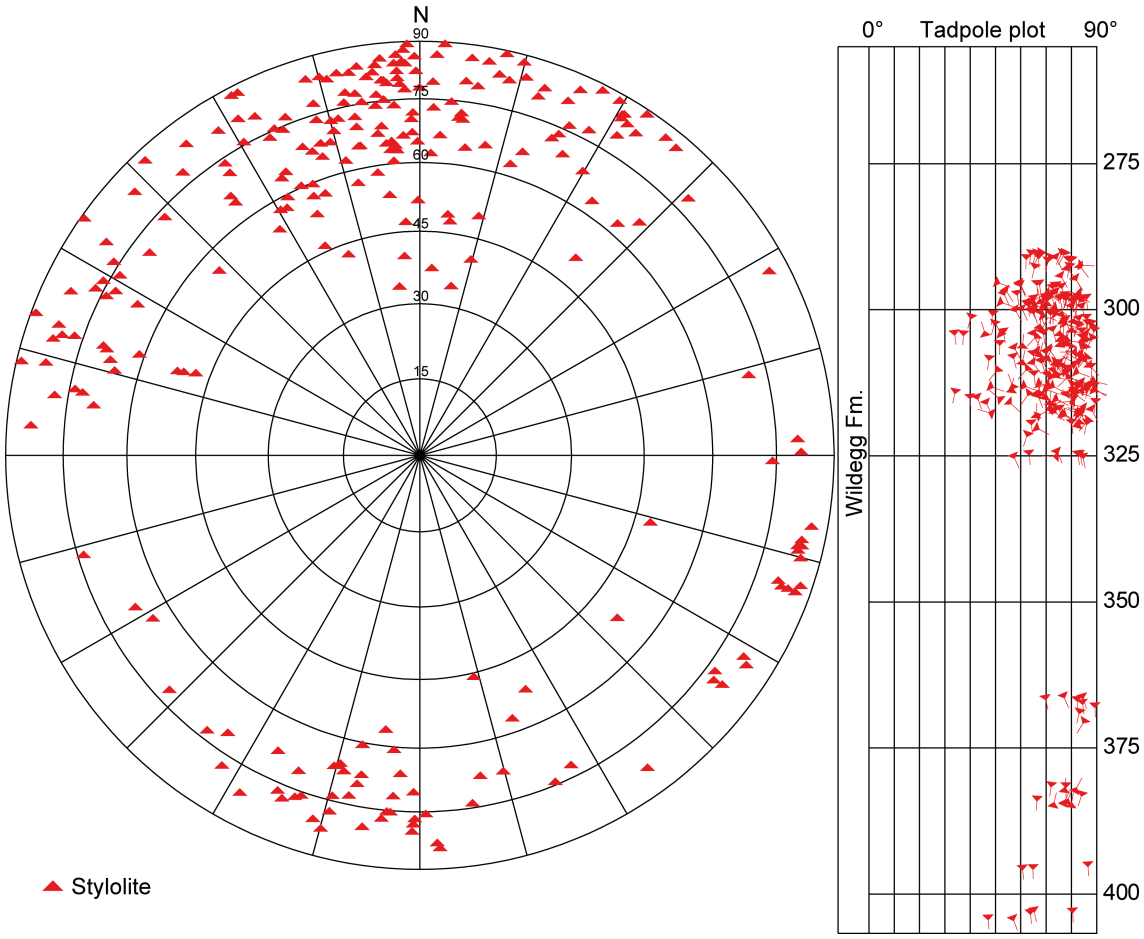


Fig. 4-21: Stereogram and depth plot of stylolites (Wildegg Formation, n = 262)

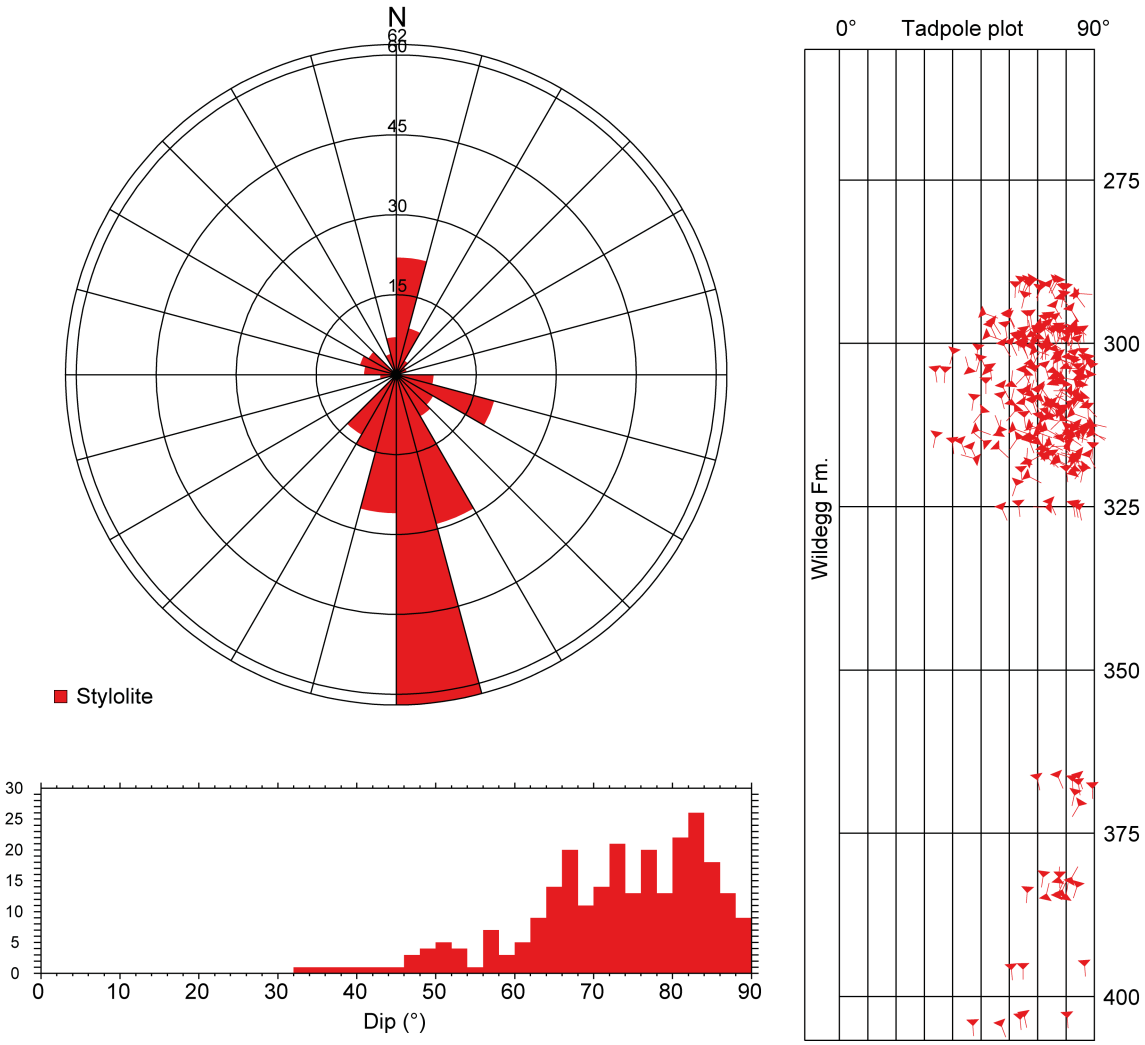


Fig. 4-22: Dip azimuth rose diagram, dip histogram and depth plot of stylolites (Wildegg Formation, n = 262)

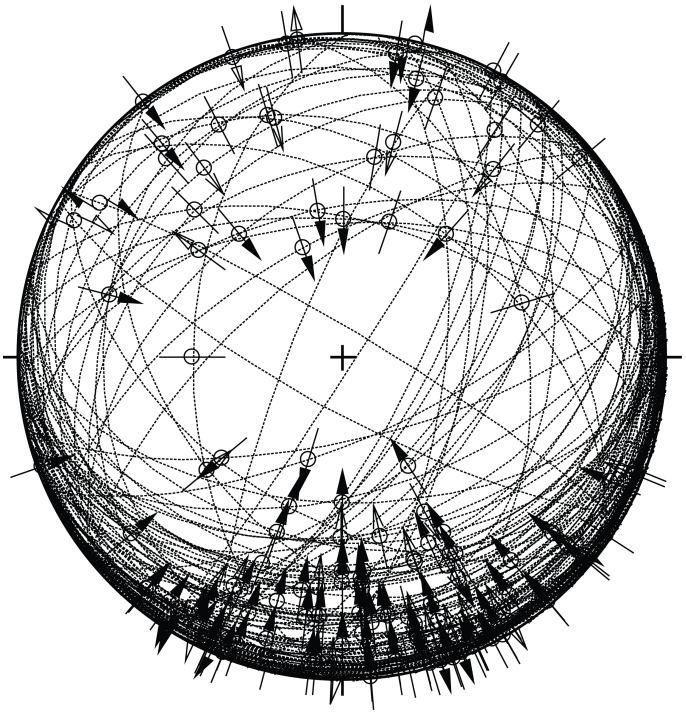


Fig. 4-23: Stereogram of fault planes with striation, including multiple lineations on a single fault plane (Wildegg Formation, n = 150)

4.3 Dogger

For the detailed stereographic evaluation, the Dogger was subdivided into three units: (1) the interval of the Hauptrogenstein to the Ifenthal Formation, (2) the Passwang Formation and (3) the Opalinus Clay. The orientation and spatial distribution of structural discontinuities within the Dogger are visualised in Figs. 4-24 to 4-39. Only the data from oriented cores are presented.

4.3.1 Hauptrogenstein to Ifenthal Formation

The cored interval of the Hauptrogenstein to the Ifenthal Formation (406.72 m to 481.55 m MD log depth) shows a moderate density of fault planes and stylolites. Both types of structures are distributed homogeneously. Fault planes generally have a flat to moderate dip and show a preferred dip towards the S. Stylolites are generally steep and show a preferred orientation towards SE to SW. Veins and joints are rare.

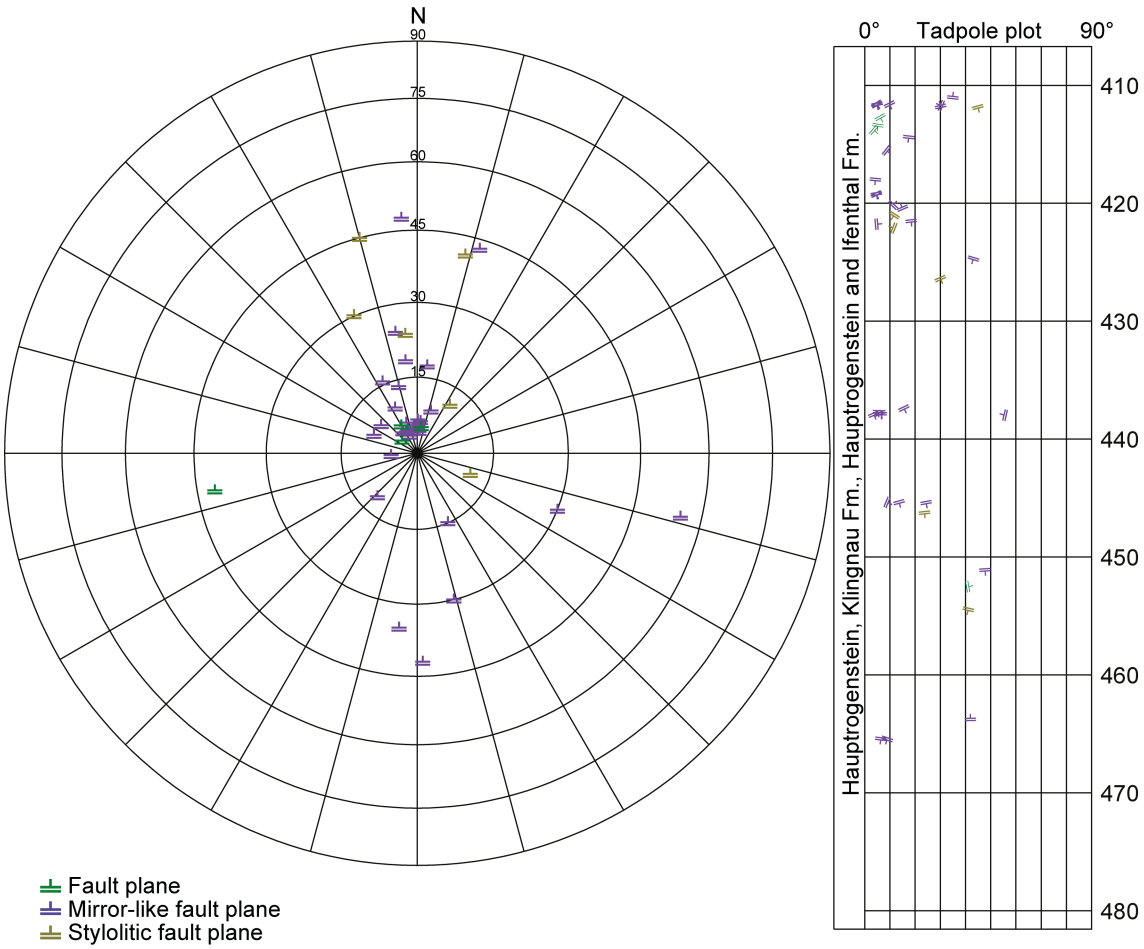


Fig. 4-24: Stereogram and depth plot of fault planes (Hauptrogenstein to Ifenthal Formation)

Fault planes (n = 4), mirror-like fault planes (n = 30) and stylolitic fault planes (n = 6).

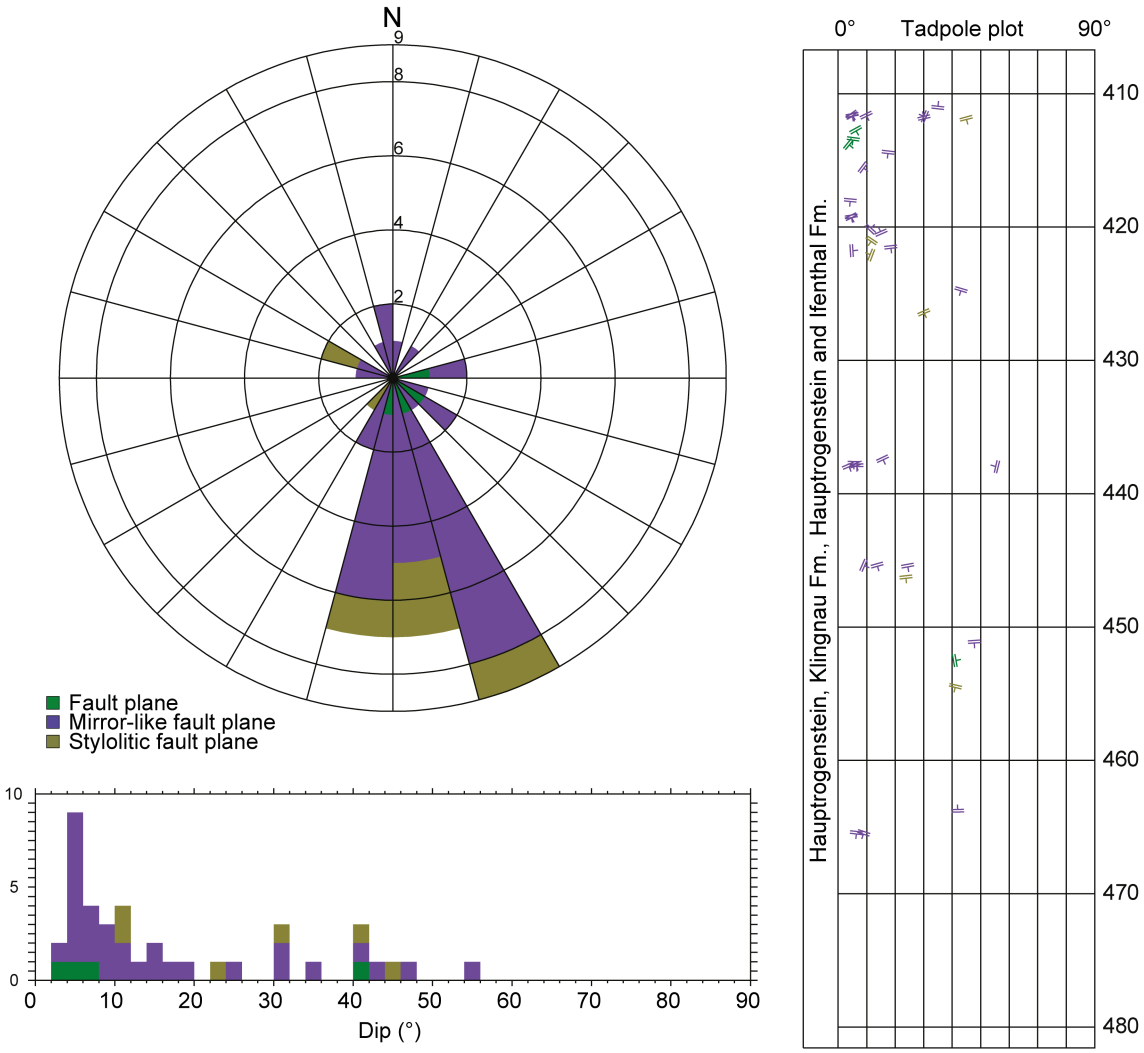


Fig. 4-25: Dip azimuth rose diagram, dip histogram and depth plot of fault planes (Hauptrogenstein to Ifenthal Formation)

Fault planes (n = 4), mirror-like fault planes (n = 30) and stylolitic fault planes (n = 6).

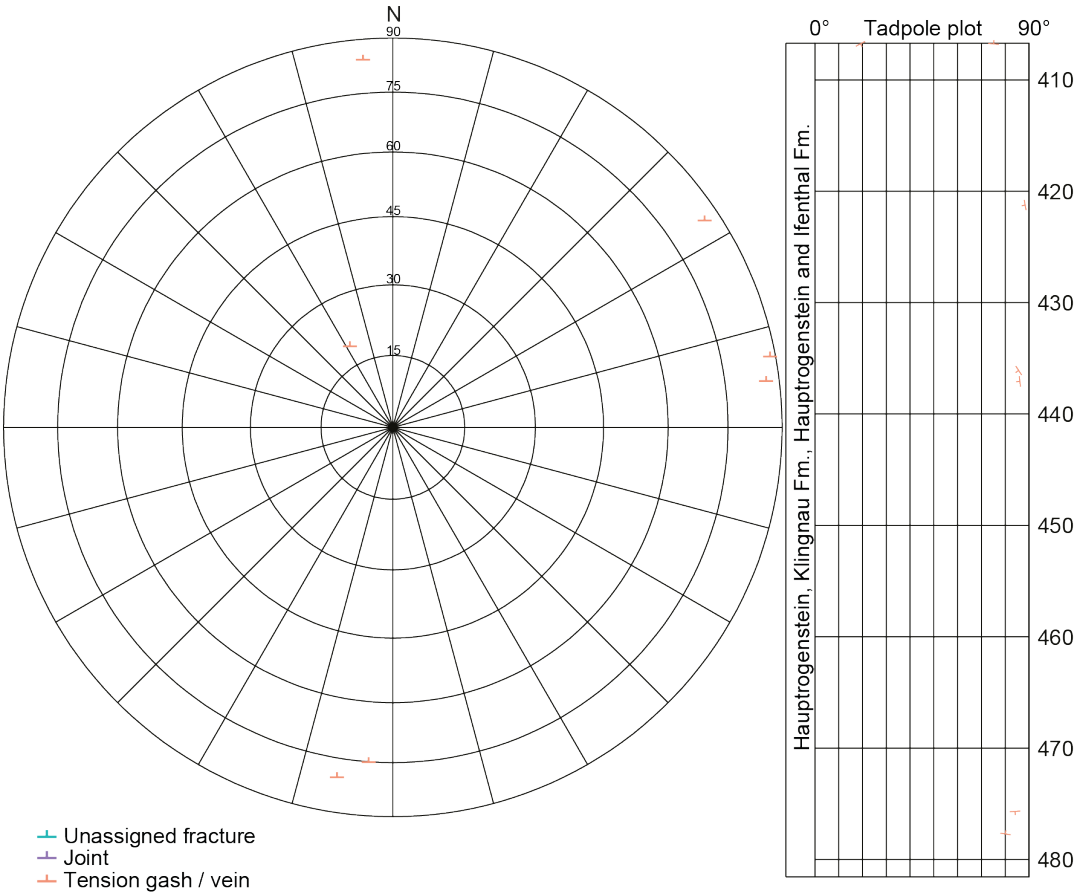


Fig. 4-26: Stereogram and depth plot of tension gashes / veins, joints and unassigned fractures (Hauptrogenstein to Ifenthal Formation)

Tension gashes / veins (n = 7); unassigned fractures and joints were not observed (n = 0).

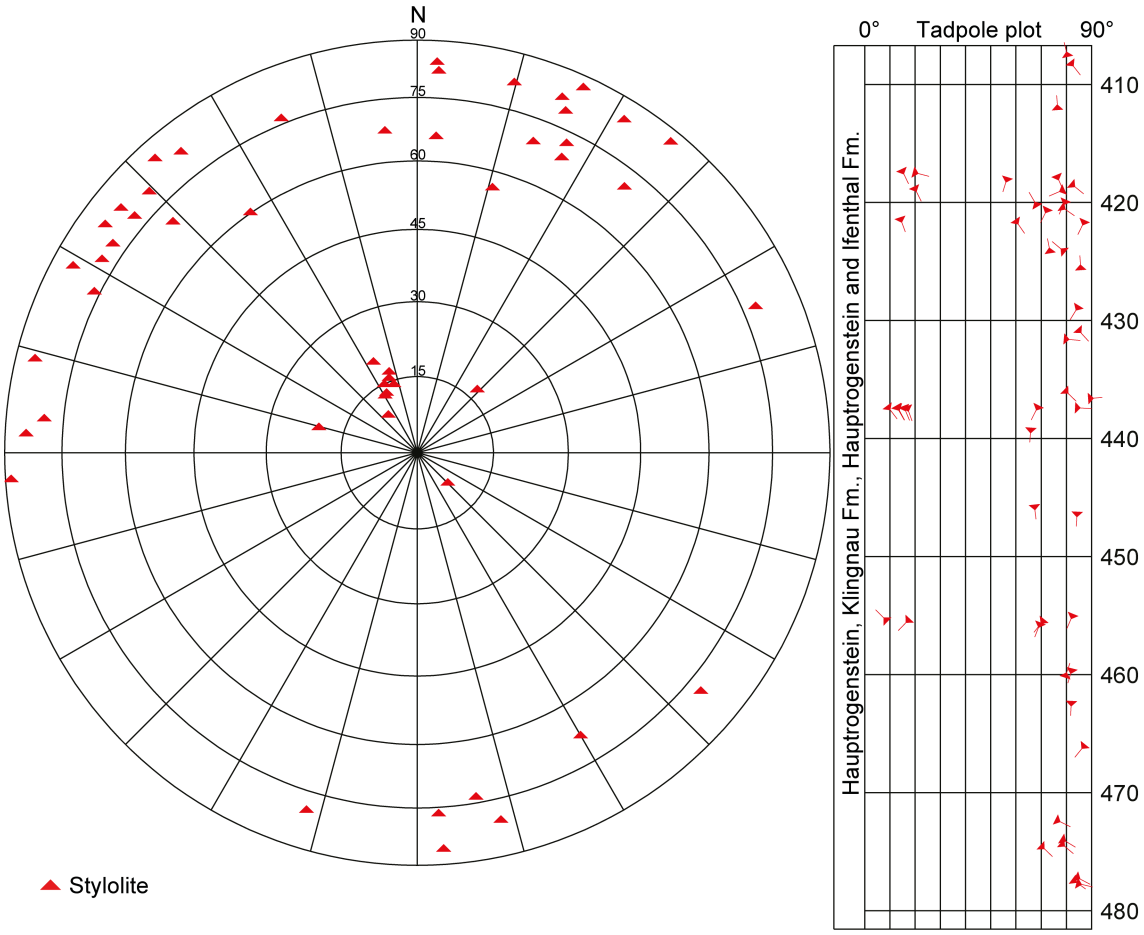


Fig. 4-27: Stereogram and depth plot of stylolites (Hauptrogenstein to Ifenthal Formation; n = 51)

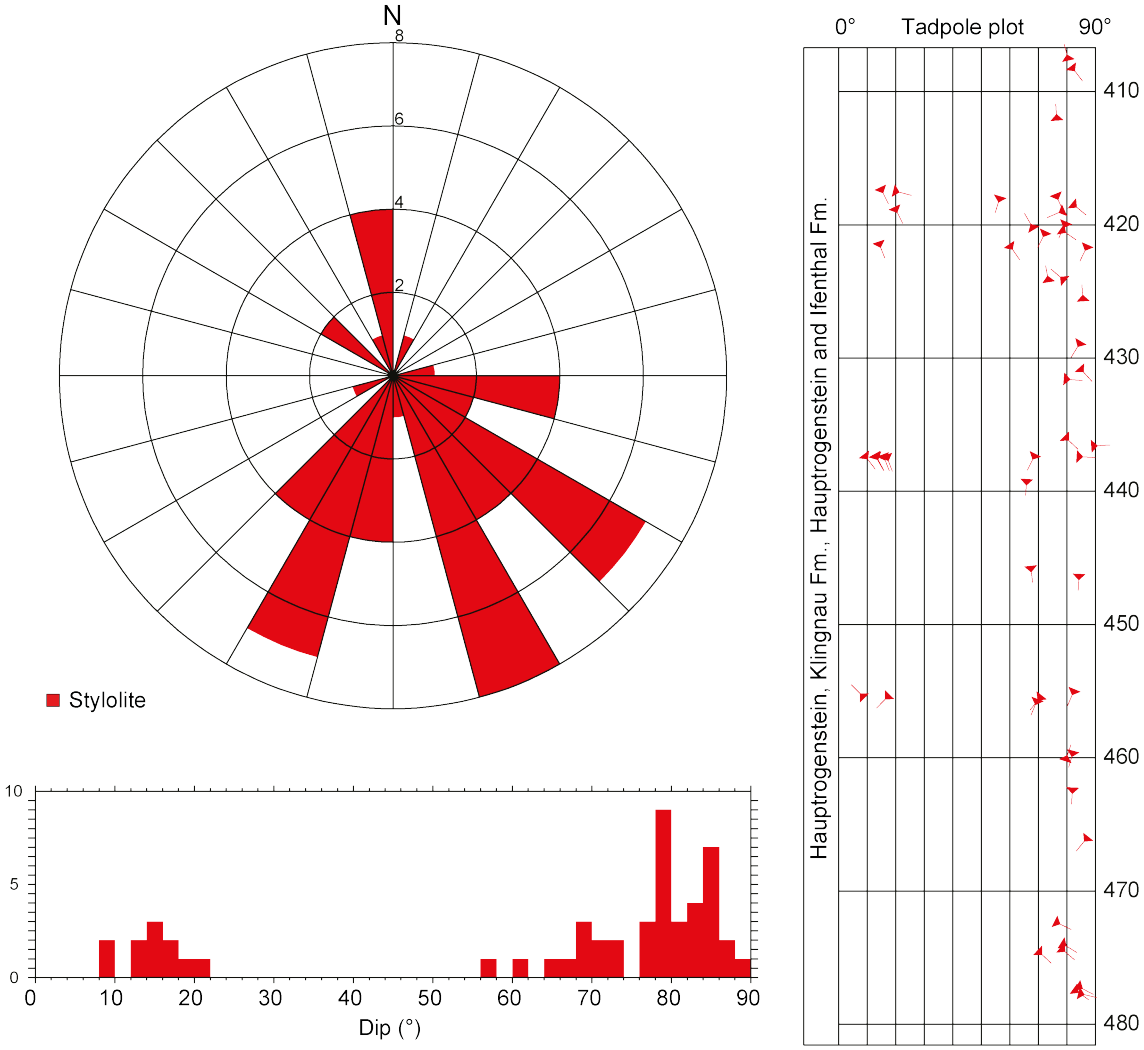


Fig. 4-28: Dip azimuth rose diagram, dip histogram and depth plot of stylolites (Hauptrogenstein to Ifenthal Formation; n = 51)

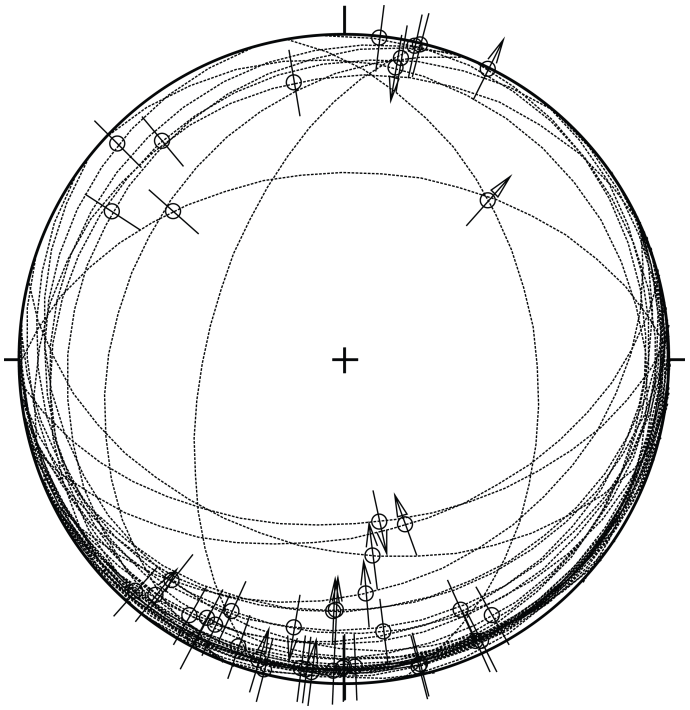


Fig. 4-29: Stereogram of fault planes with striations, including multiple lineations on a single fault plane (Hauptrogenstein to Ifenthal Formation; n = 40)

4.3.2 Passwang Formation

The Passwang Formation (481.55 m to 530.32 m MD log depth) is characterised by a low number of fractures.

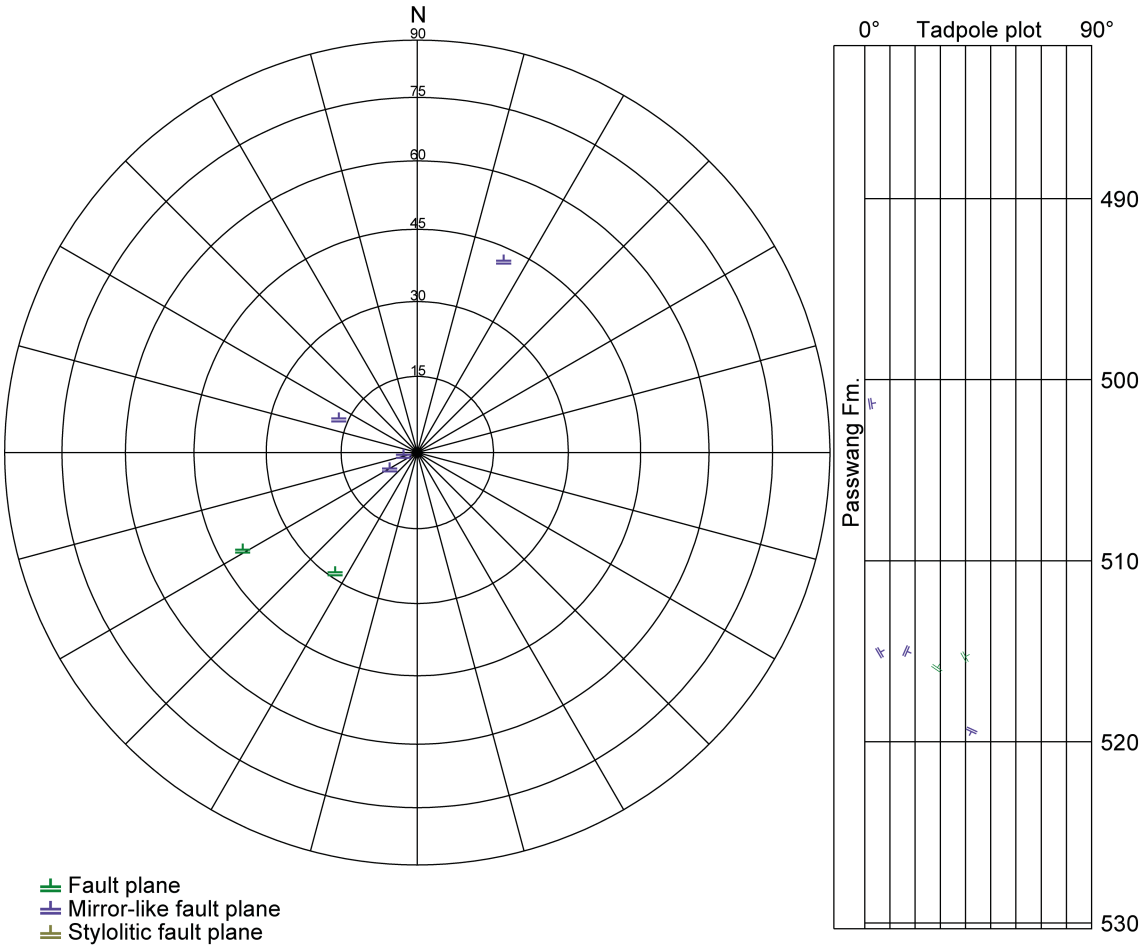


Fig. 4-30: Stereogram and depth plot of fault planes (Passwang Formation)

Fault planes (n = 2), mirror-like fault planes (n = 4); stylolitic fault planes were not observed (n = 0).

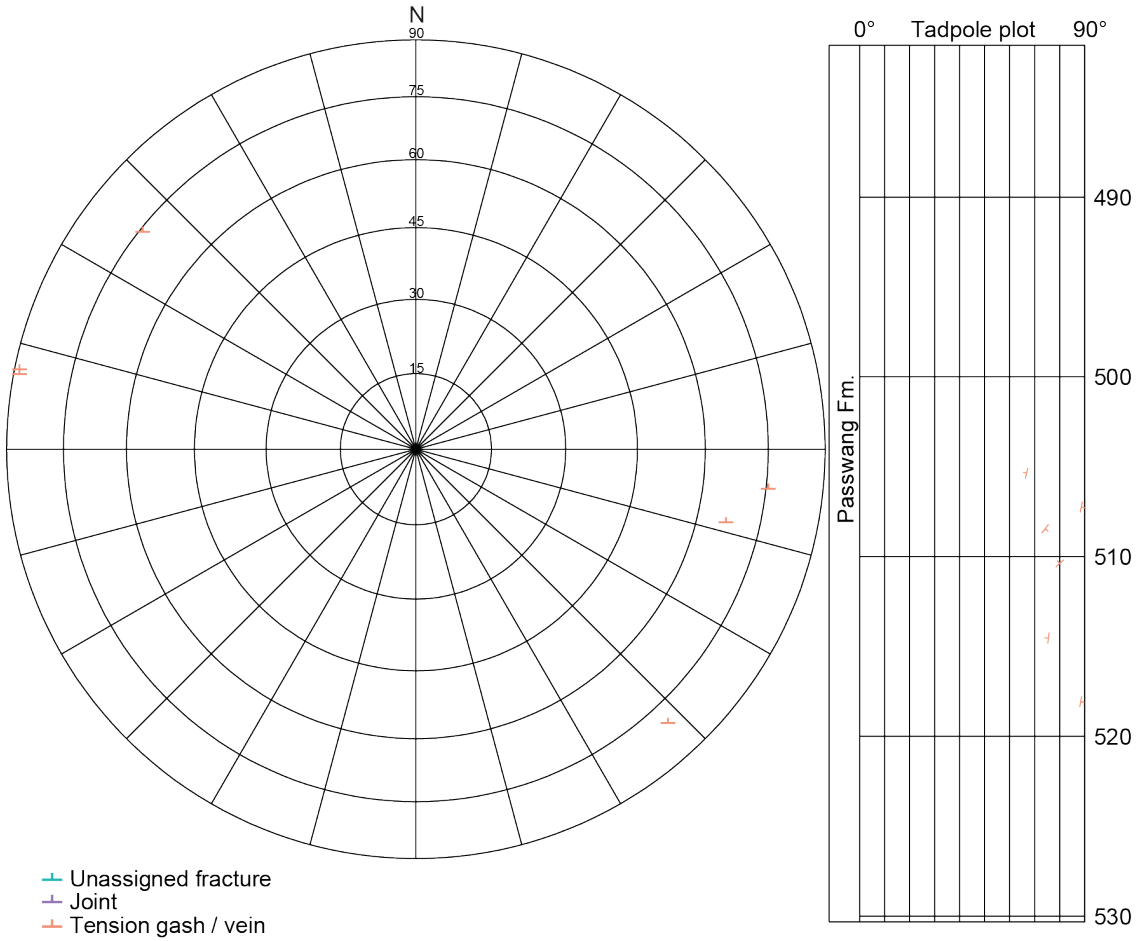


Fig. 4-31: Stereogram and depth plot of tension gashes / veins, joints and unassigned fractures (Passwang Formation)

Tension gashes / veins (n = 6); unassigned fractures and joints were not observed (n = 0).

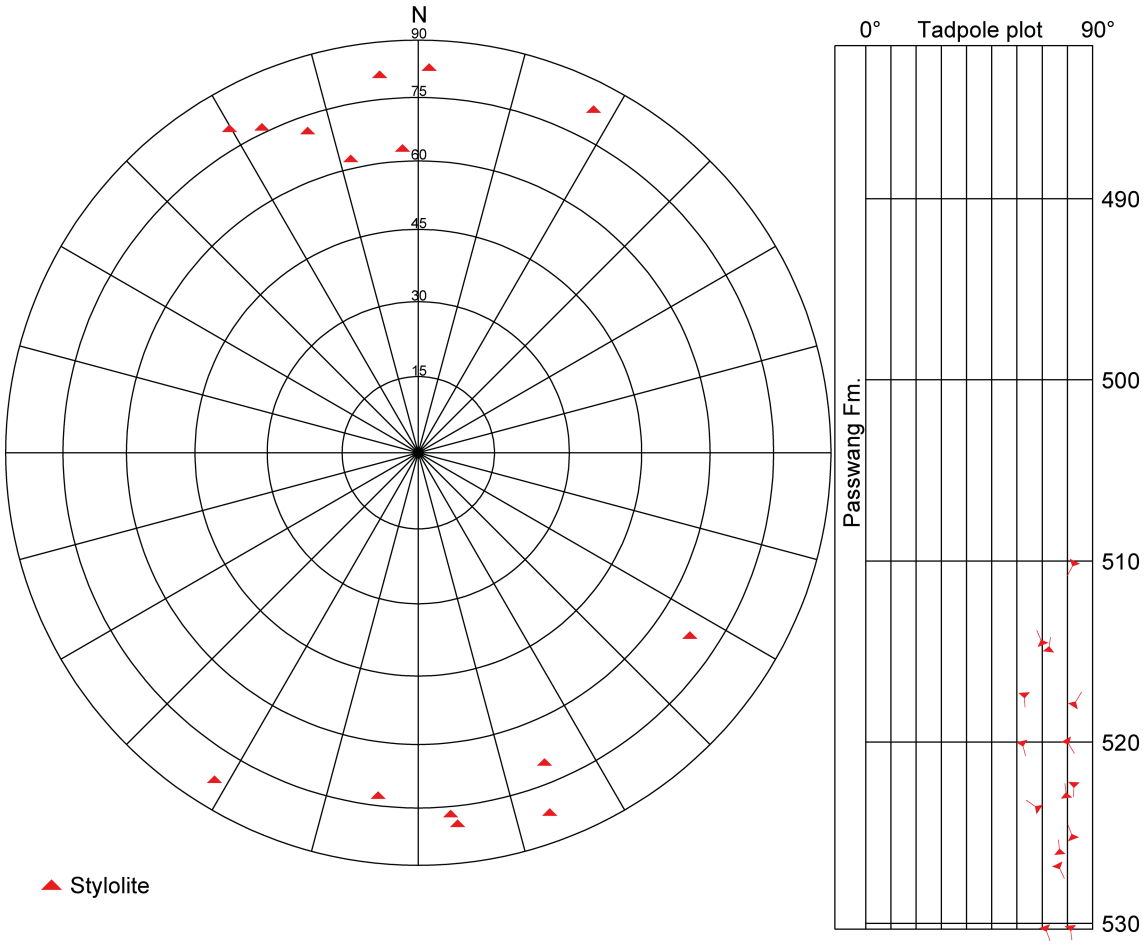


Fig. 4-32: Stereogram and depth plot of stylolites (Passwang Formation; n = 15)

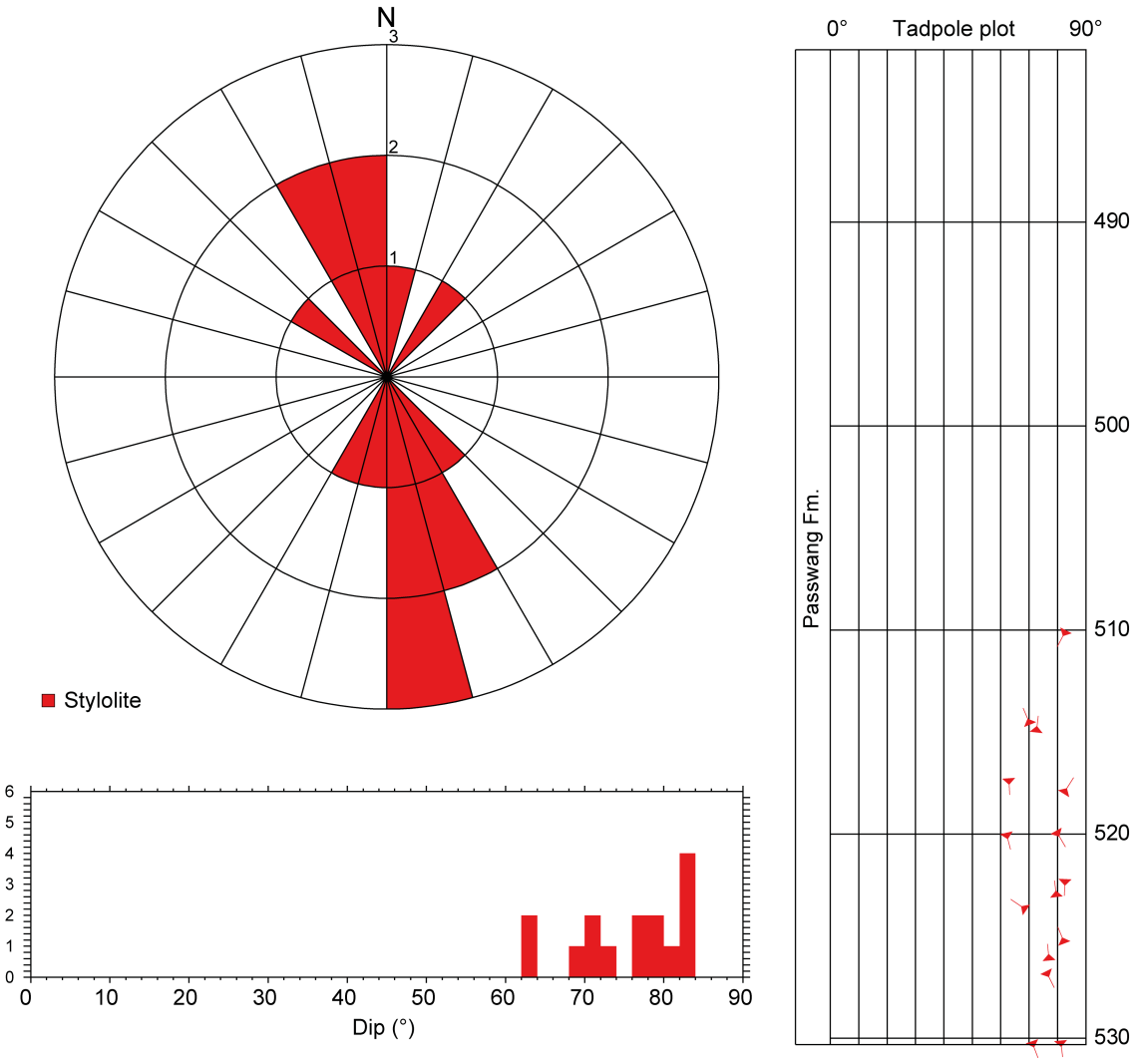


Fig. 4-33: Dip azimuth rose diagram, dip histogram and depth plot of stylolites (Passwang Formation; n = 15)

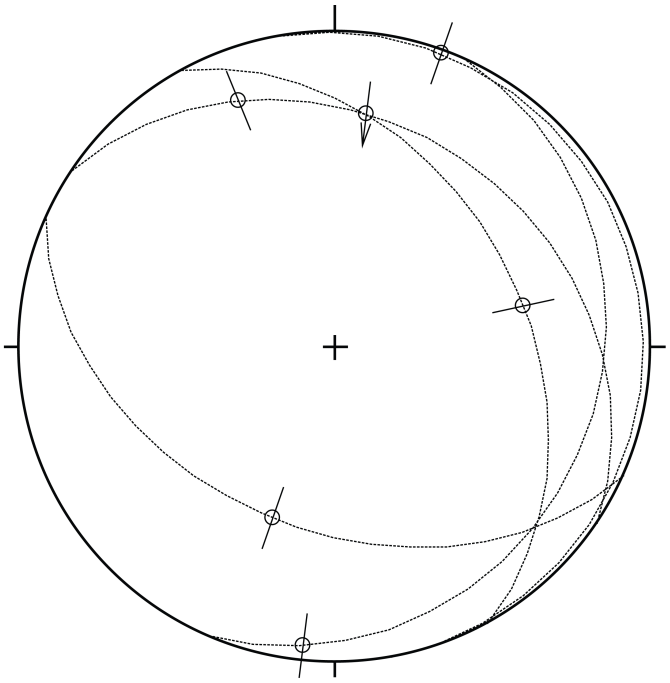


Fig. 4-34: Stereogram of fault planes with striations (Passwang Formation; n = 6)

4.3.3 Opalinus Clay

The bedding in the Opalinus Clay (530.32 m to 651.46 m MD log depth) reveals low (1° to 10°) dip magnitudes with slightly variable dip directions towards the SE, SSE, S and SSW. The variations in bedding orientation were governed by faults and fault zones, e.g. from 563.00 m to 567.00 m MD (log depth), at 588.38 m MD (log depth) and from 622.60 m to 625.00 m MD (log depth). In addition, intervals with potential soft-sediment deformation were interpreted from 568.90 m to 572.00 m MD (log depth), from 600.70 m to 607.60 m MD (log depth) and from 623.90 m to 627.26 m MD (log depth).

Most of the fractures occur in the lower half of the Opalinus Clay. In this interval, the distribution of fractures is more or less homogeneous with a predominance of fault planes. Veins are subordinate. Fault planes mostly show a shallow dip mainly towards the S. The dominant shear sense is reverse. Tension gashes are orientated randomly. Both fault planes and veins are often characterised by synkinematic calcite fillings, which are commonly less than 1 mm thick. Stylolites were not observed in the Opalinus Clay.

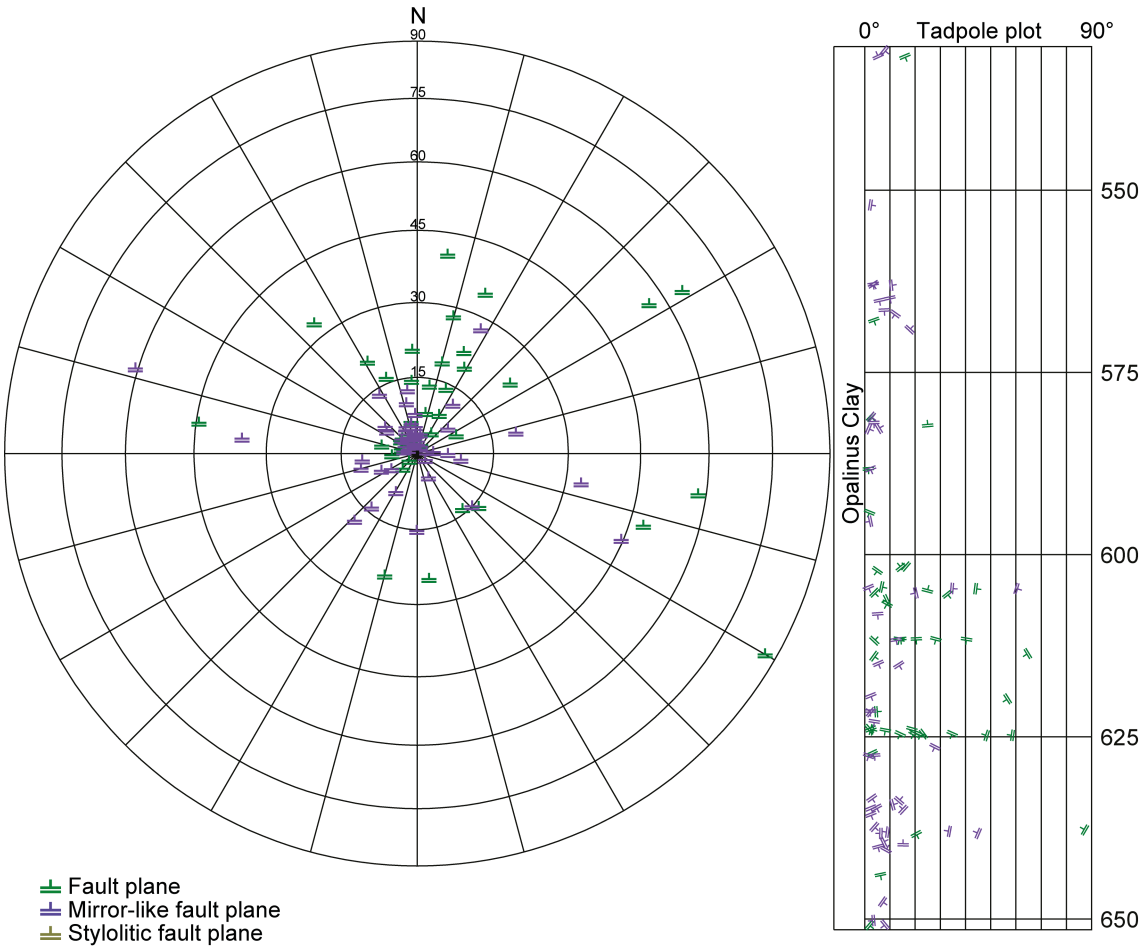


Fig. 4-35: Stereogram and depth plot of fault planes (Opalinus Clay)

Fault planes (n = 43), mirror-like fault planes (n = 51); stylolitic fault planes were not observed (n = 0).

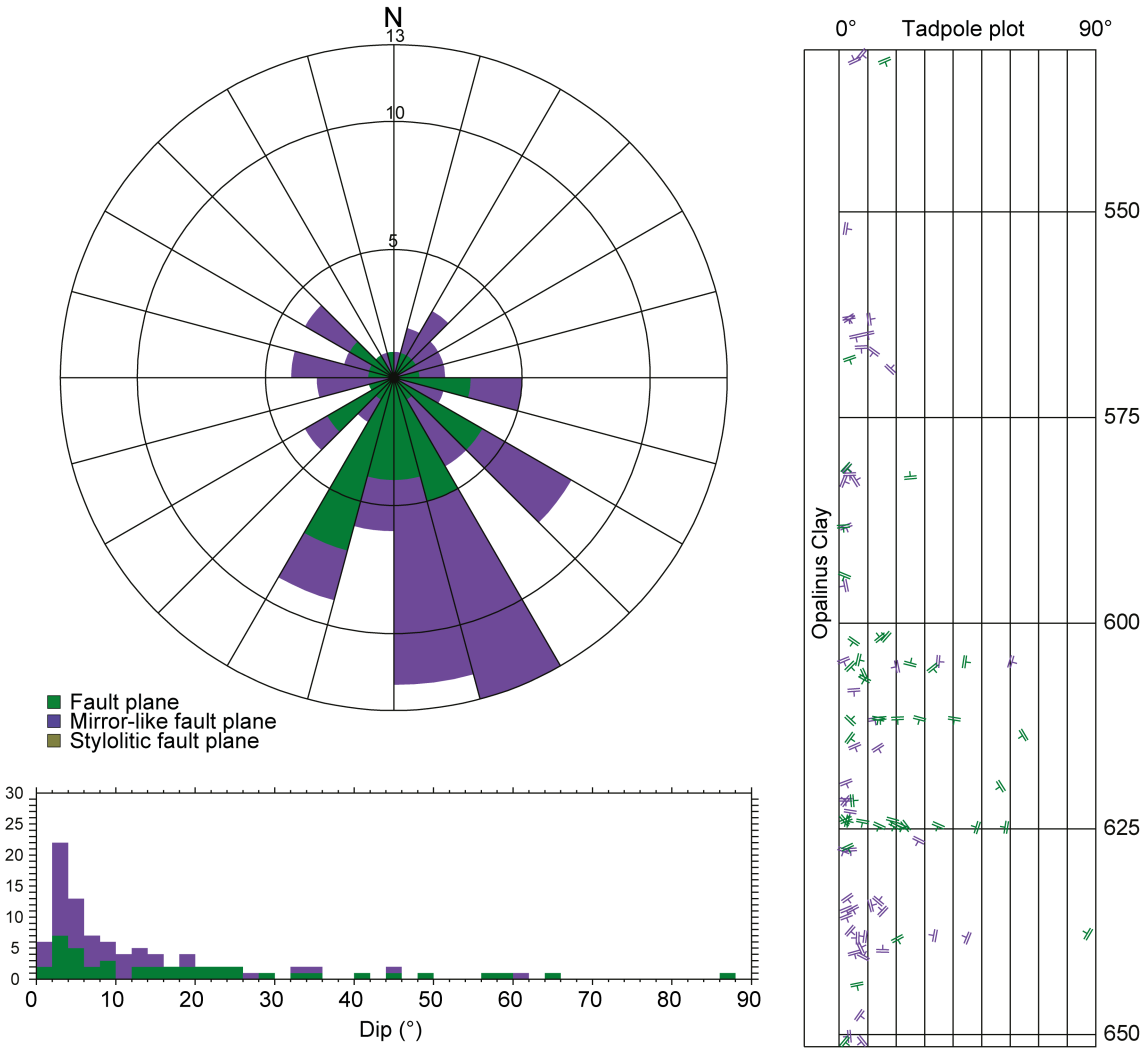


Fig. 4-36: Dip azimuth rose diagram, dip histogram and depth plot of fault planes (Opalinus Clay)

Fault planes (n = 43), mirror-like fault planes (n = 51); stylolitic fault planes were not observed (n = 0).

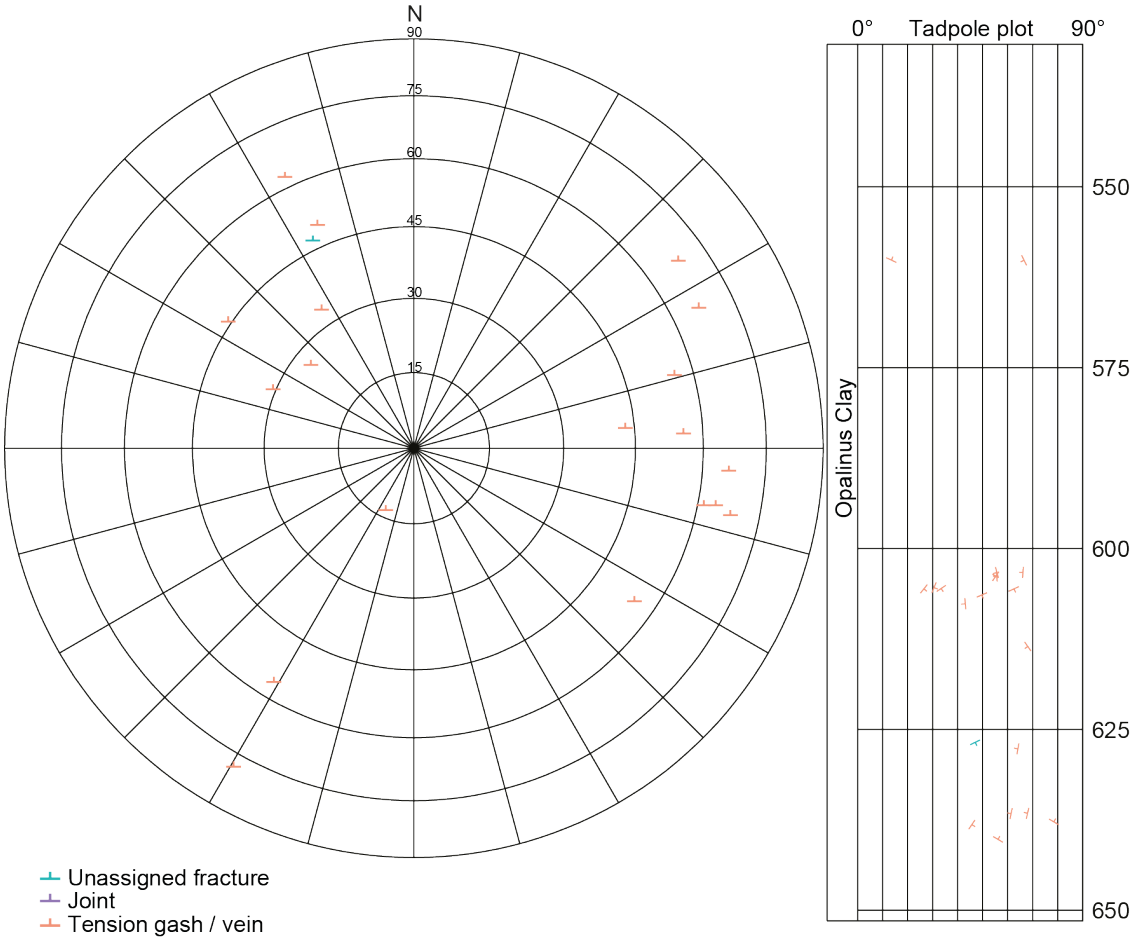


Fig. 4-37: Stereogram and depth plot of tension gashes / veins, joints and unassigned fractures (Opalinus Clay)

Unassigned fractures (n = 1) and tension gashes / veins (n = 19); joints were not observed (n = 0).

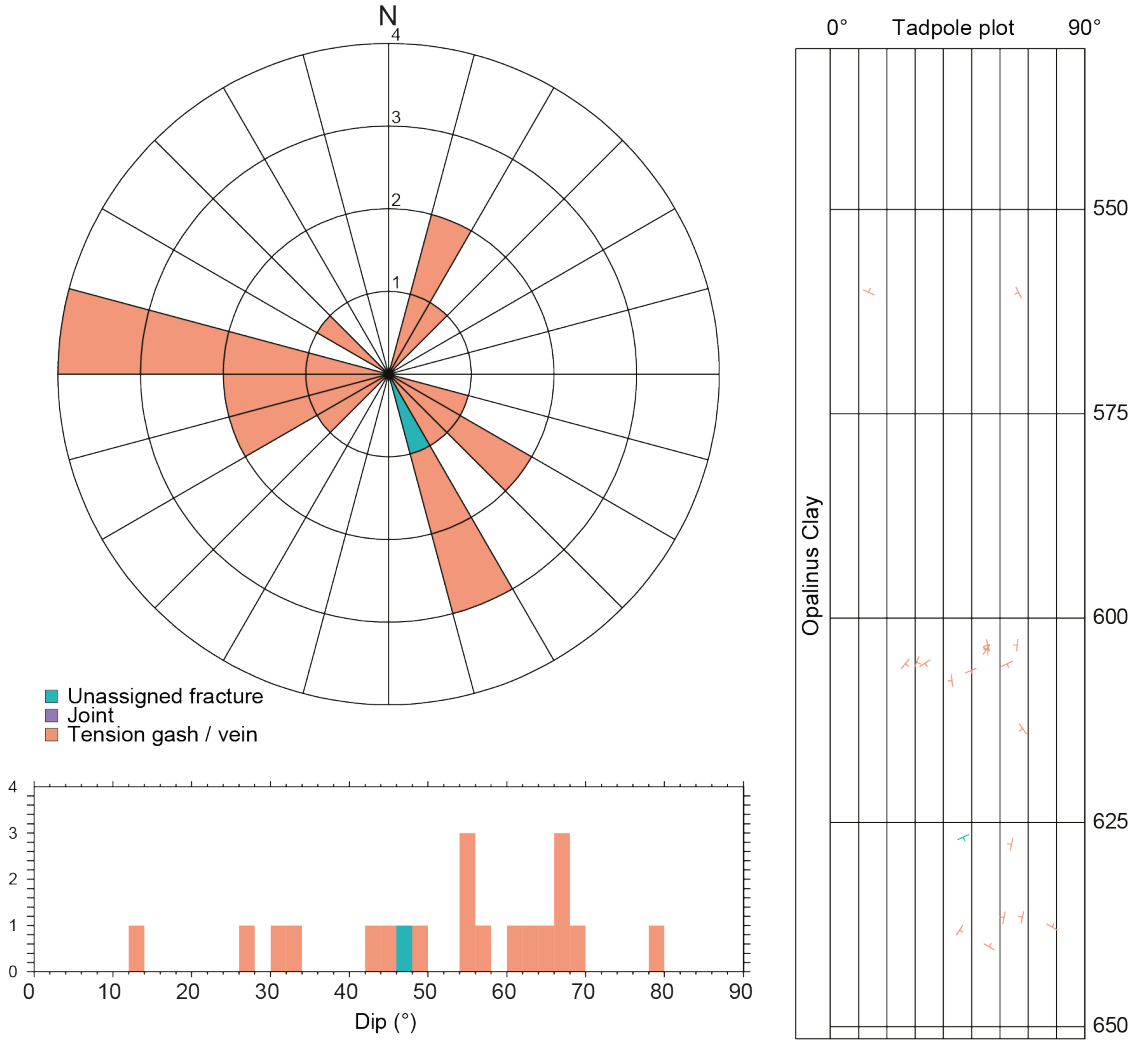


Fig. 4-38: Dip azimuth rose diagram, dip histogram and depth plot of tension gashes / veins, joints and unassigned fractures (Opalinus Clay)

Unassigned fractures (n = 1) and tension gashes / veins (n = 19); joints were not observed (n = 0).

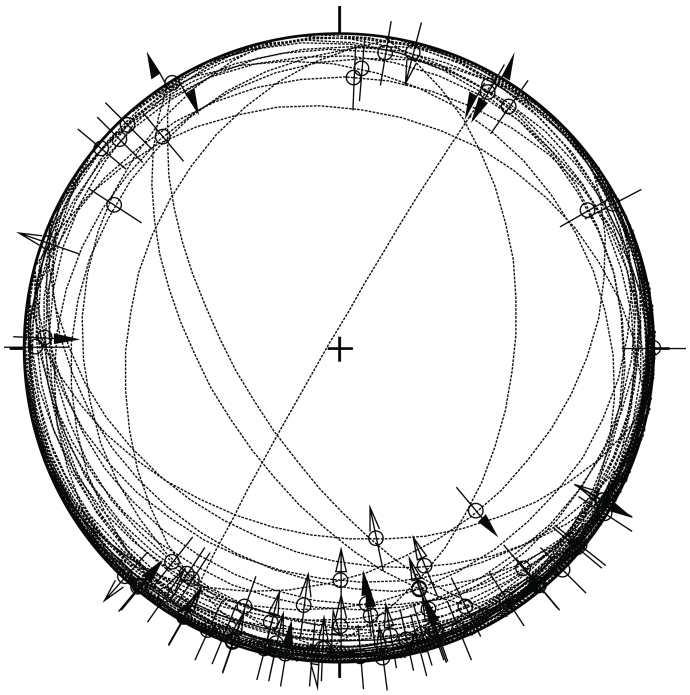


Fig. 4-39: Stereogram of fault planes with striations, including multiple lineations on a single fault plane (Opalinus Clay; n = 71)

4.4 Lias (Staffelegg Formation)

As presented in Figs. 4-40 to 4-46, the Lias (651.46 m to 688.76 m MD log depth) is characterised by a moderate number of fractures, predominantly mirror-like fault planes and subordinate stylolites and tension gashes. Stylolites and tension gashes are concentrated in calcareous beds, while the mirror-like fault planes occur in clay-rich layers in the lower part of the Staffelegg Formation. Mirror-like fault planes are mostly subhorizontal and show a preferred dip towards the SE. Stylolites and tension gashes tend to be more steeply dipping and are oriented more randomly. Only the data from oriented cores are presented.

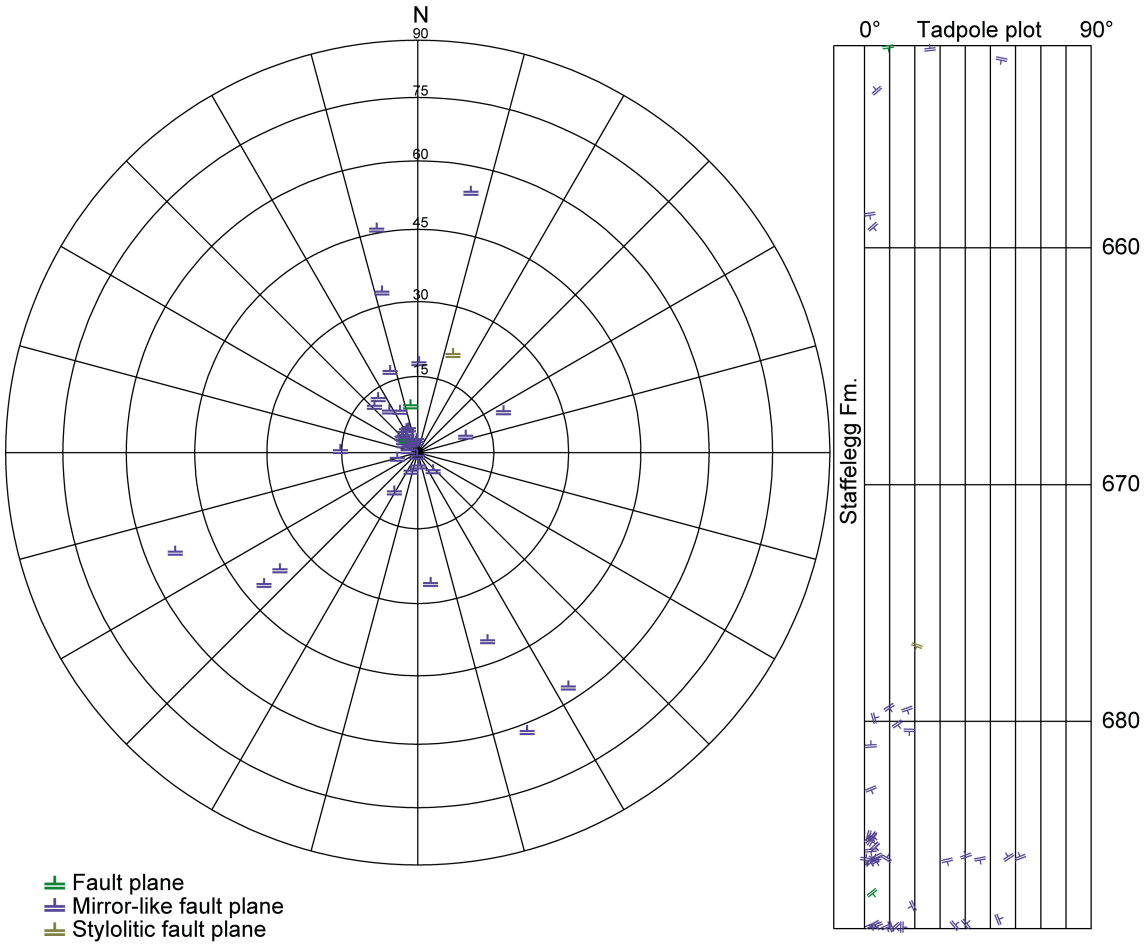


Fig. 4-40: Stereogram and depth plot of fault planes (Lias)

Fault planes (n = 2), mirror-like fault planes (n = 43) and stylolitic fault planes (n = 1).

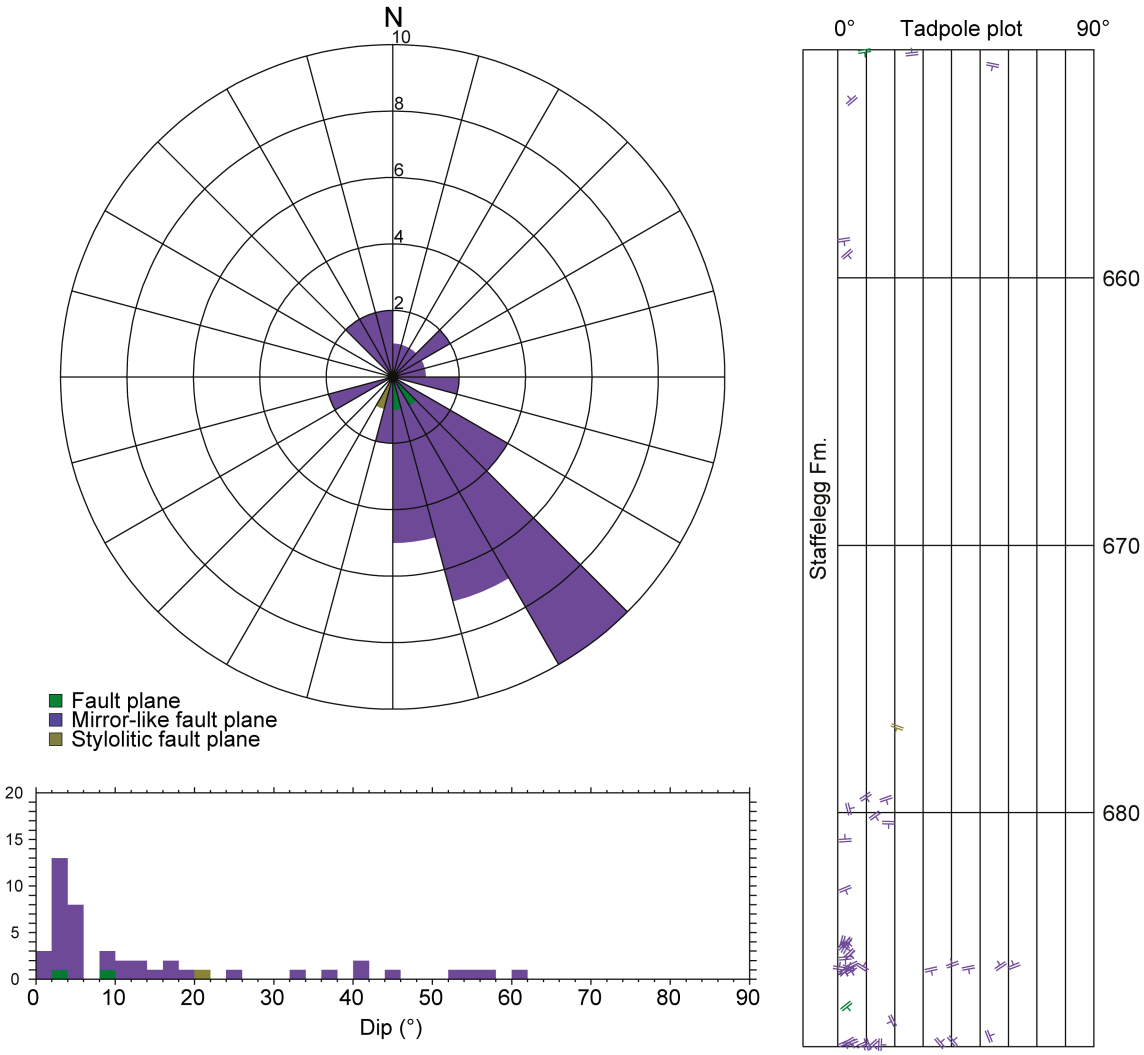


Fig. 4-41: Dip azimuth rose diagram, dip histogram and depth plot of fault planes (Lias)

Fault planes (n = 2), mirror-like fault planes (n = 43) and stylolitic fault planes (n = 1).

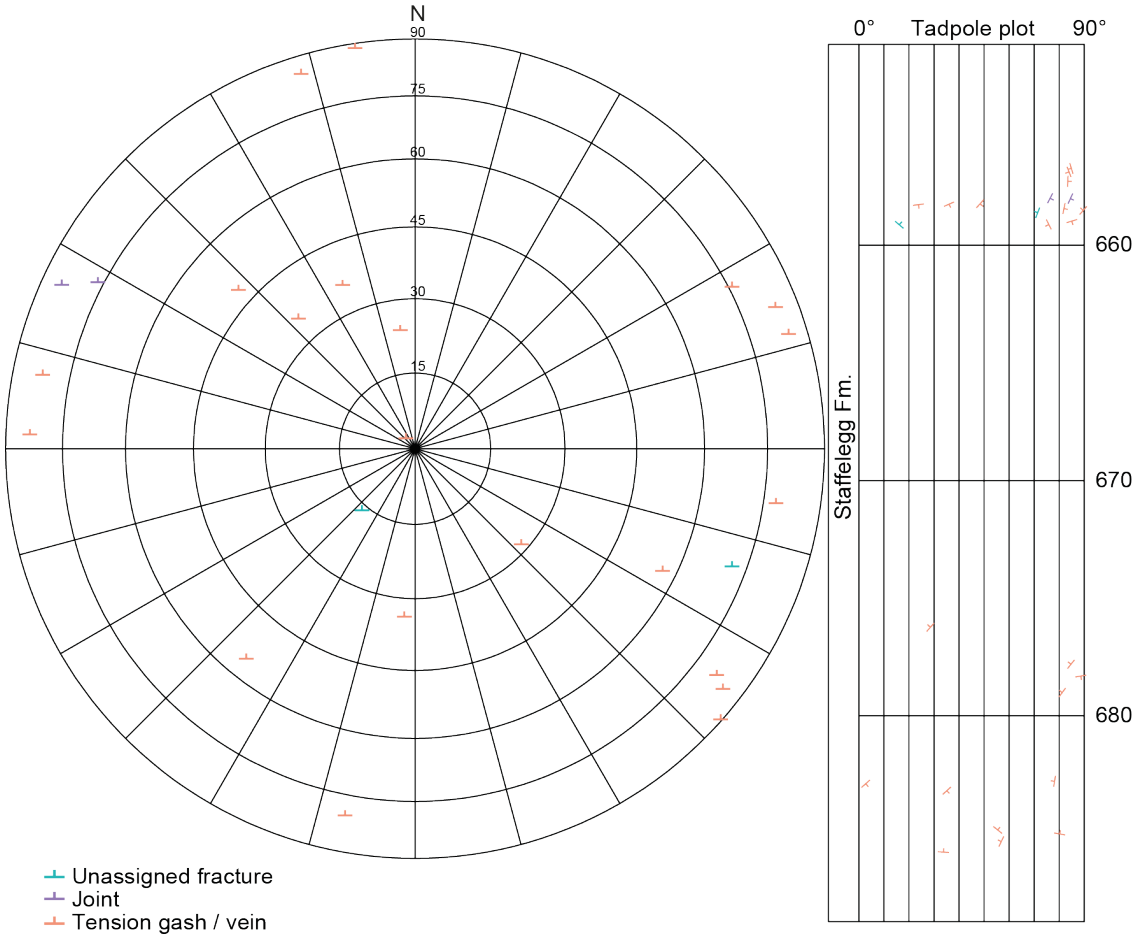


Fig. 4-42: Stereogram and depth plot of tension gashes / veins, joints and unassigned fractures (Lias)

Unassigned fractures (n = 2), joints (n = 2) and tension gashes / veins (n = 21).

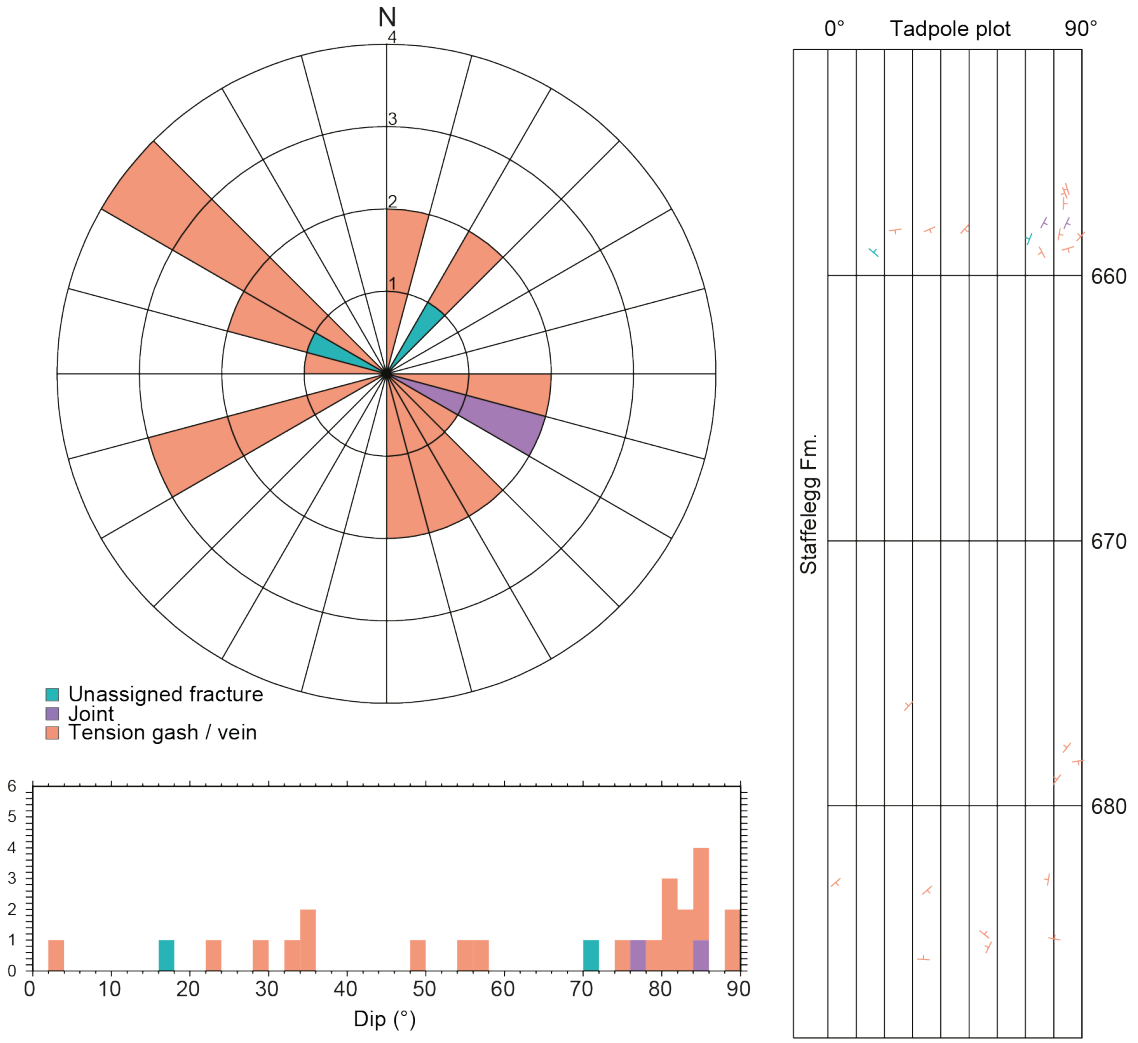


Fig. 4-43: Dip azimuth rose diagram, dip histogram and depth plot of tension gashes / veins, joints and unassigned fractures (Lias)

Unassigned fractures (n = 2), joints (n = 2) and tension gashes / veins (n = 21).

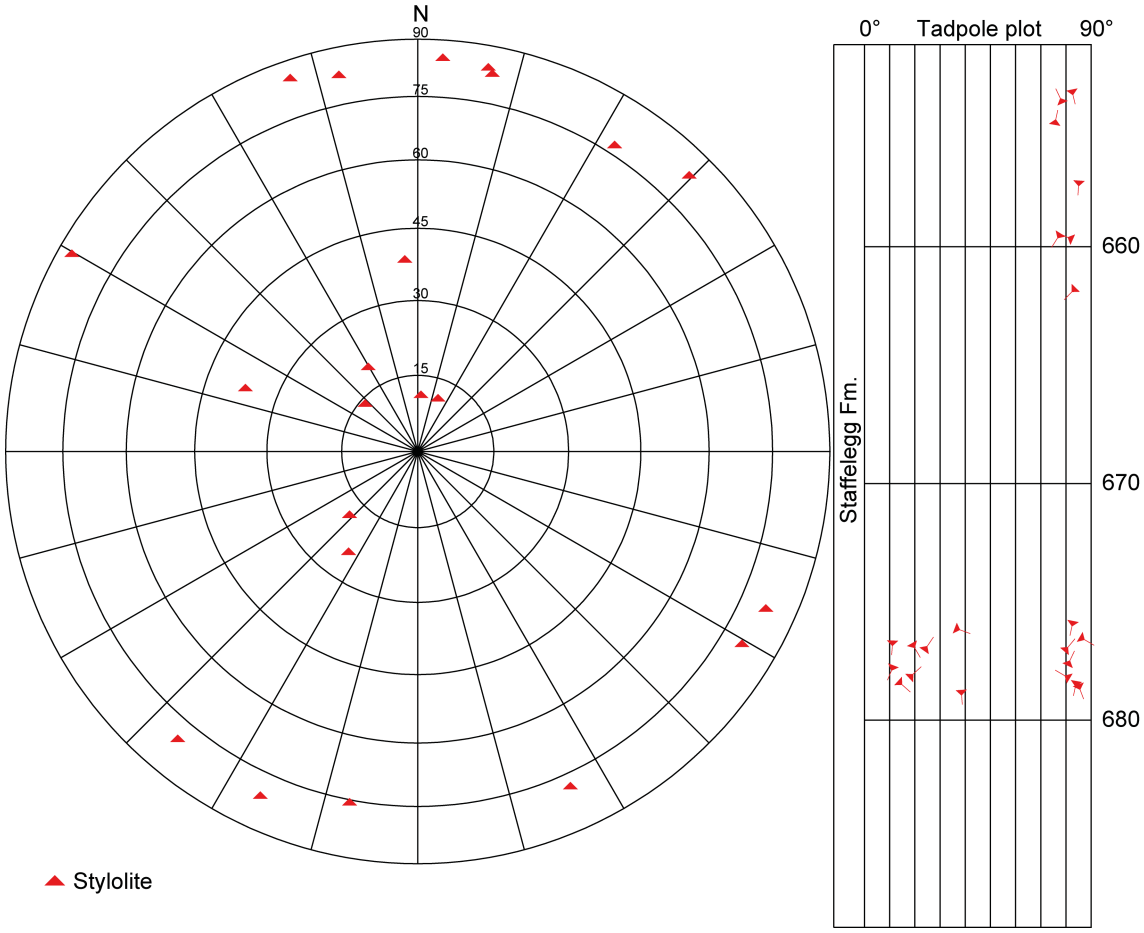


Fig. 4-44: Stereogram and depth plot of stylolites (Lias; n = 22)

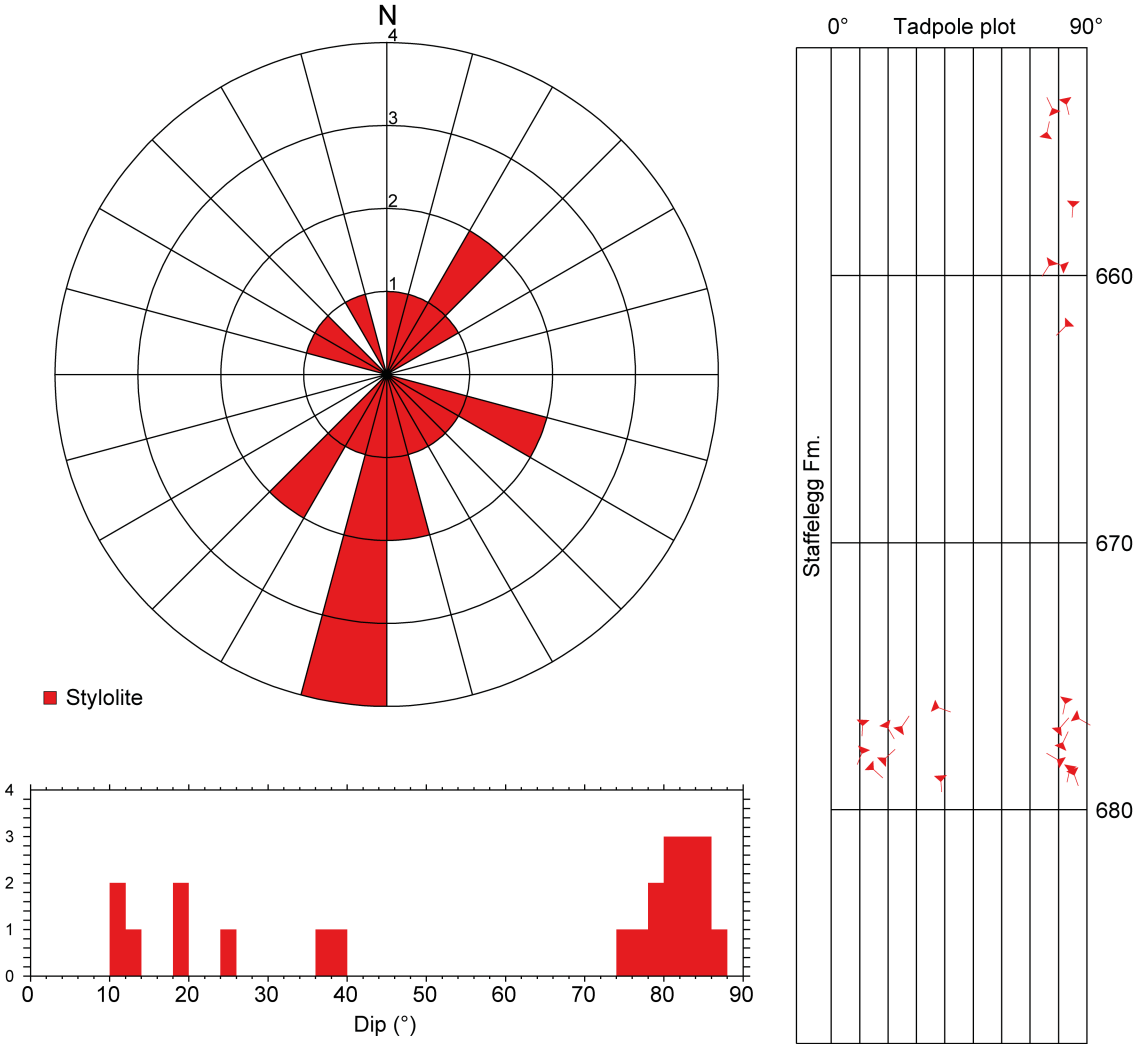


Fig. 4-45: Dip azimuth rose diagram, dip histogram and depth plot of stylolites (Lias; n = 22)

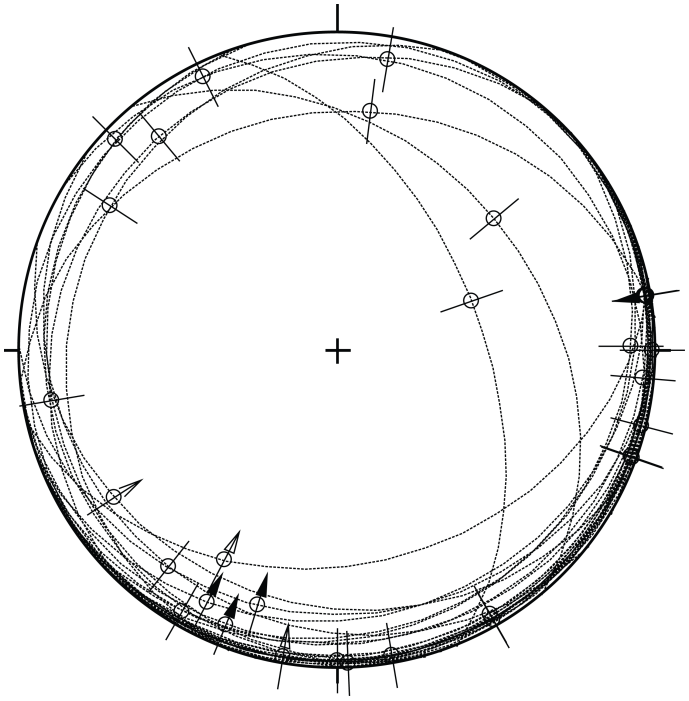


Fig. 4-46: Stereogram of fault planes with striations, including multiple lineations on a single fault plane (Lias; n = 28)

4.5 Keuper

The Keuper (688.76 m to 812.45 m MD log depth) displays the highest average fracture density of 5.9 fractures per metre. Mirror-like fault planes and tension gashes / veins prevail. The latter are mainly found within the Bänkerjoch Formation and show random orientations. The fault planes display a preferred dip of less than 50° towards the S. The shear sense is mostly reverse. Only the data from oriented cores are presented.

4.5.1 Klettgau Formation

In the Klettgau Formation (688.76 m to 720.21 m MD log depth), mirror-like fault planes are the dominant fracture type (Figs. 4-47 to 4-49). They are homogeneously distributed throughout the interval and have shallow dip angles with a slight preference for a dip direction towards the S. Tension gashes / veins, joints and stylolites were absent.

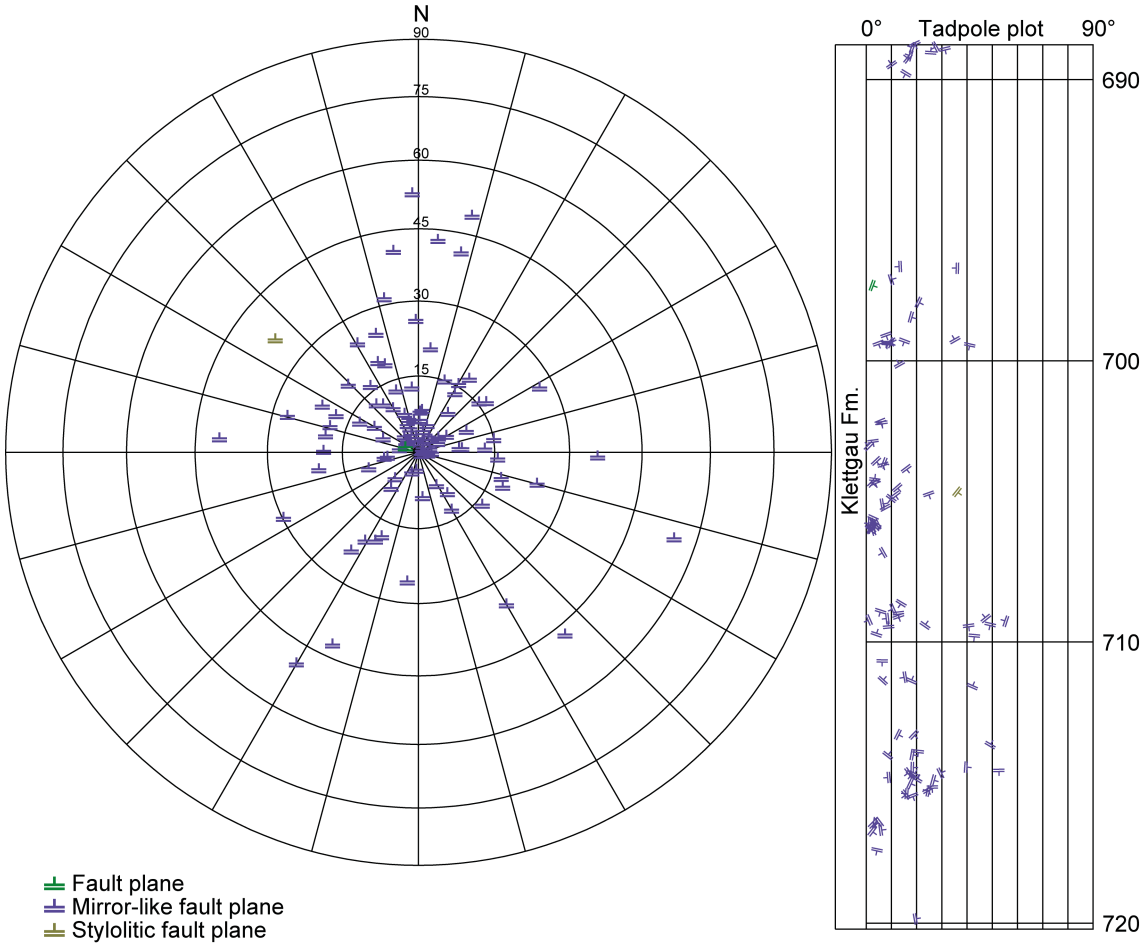


Fig. 4-47: Stereogram and depth plot of faults (Klettgau Formation)

Fault planes (n = 1), mirror-like fault planes (n = 104) and stylolitic fault planes (n = 1).

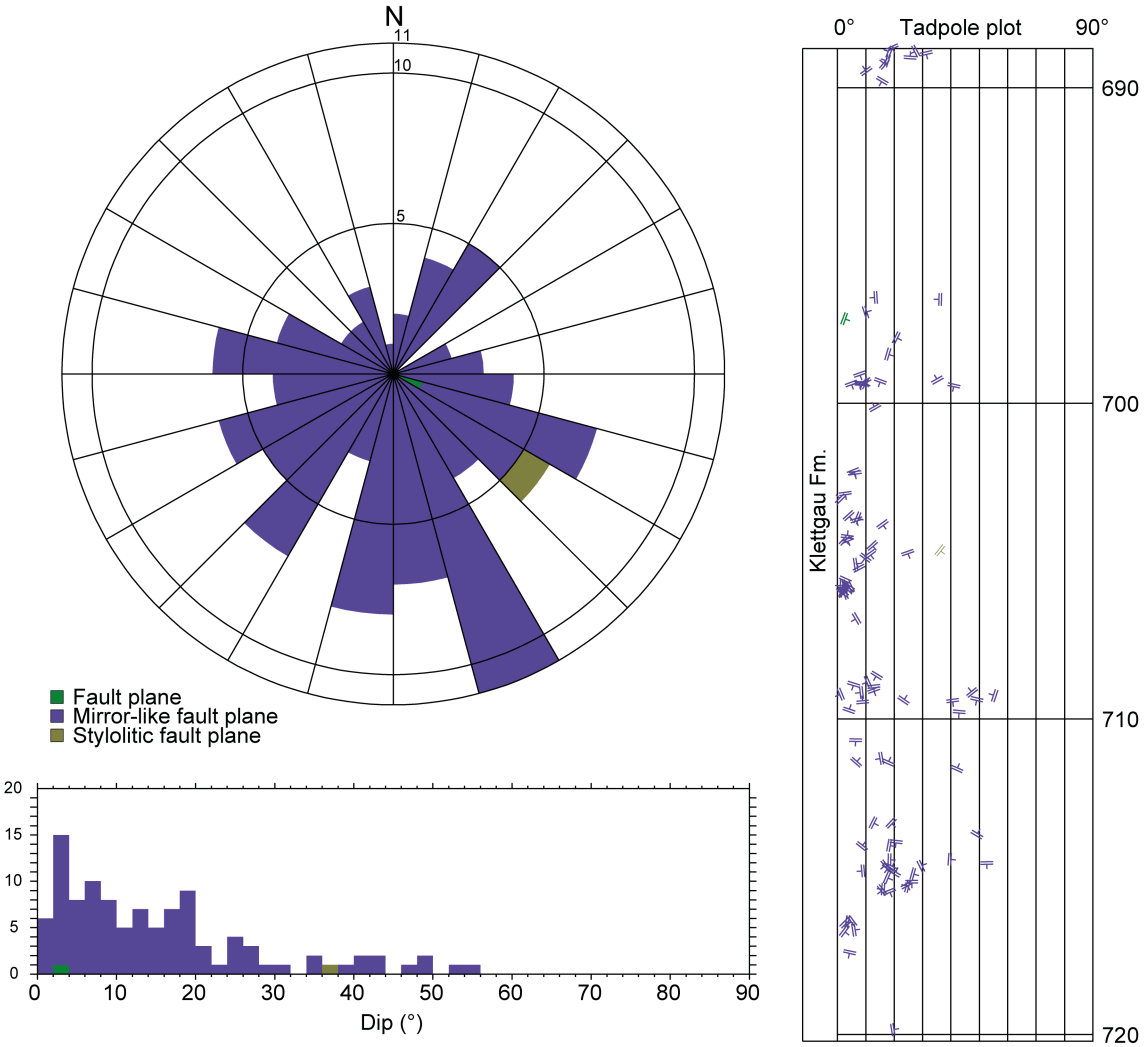


Fig. 4-48: Dip azimuth rose diagram, dip histogram and depth plot of faults (Klettgau Formation)

Fault planes (n = 1), mirror-like fault planes (n = 104) and stylolitic fault planes (n = 1).

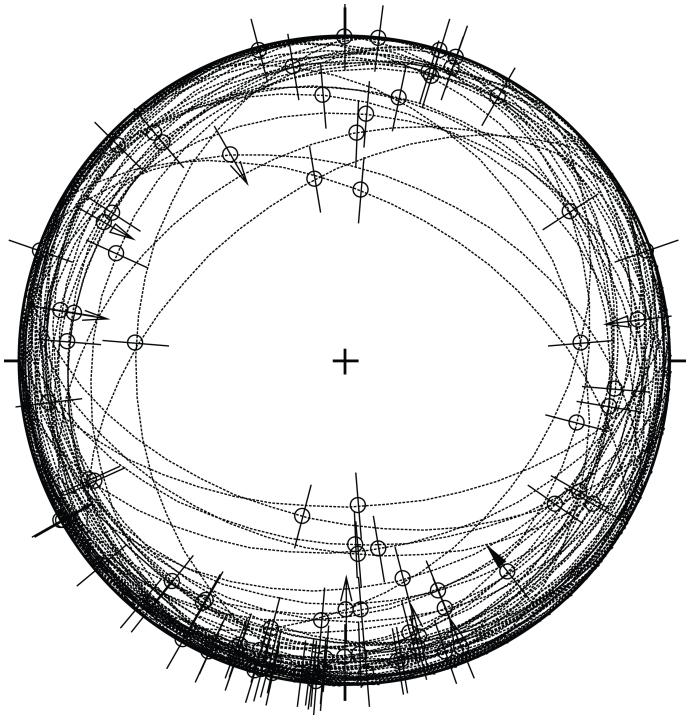


Fig. 4-49: Stereogram of fault planes with striations, including multiple lineations on a single fault plane (Klettgau Formation; n = 89)

4.5.2 Bänkerjoch Formation

The orientation and spatial distribution of the structural inventory of the Bänkerjoch Formation (720.21 m to 812.45 m MD log depth) are shown in Figs. 4-50 to 4-54.

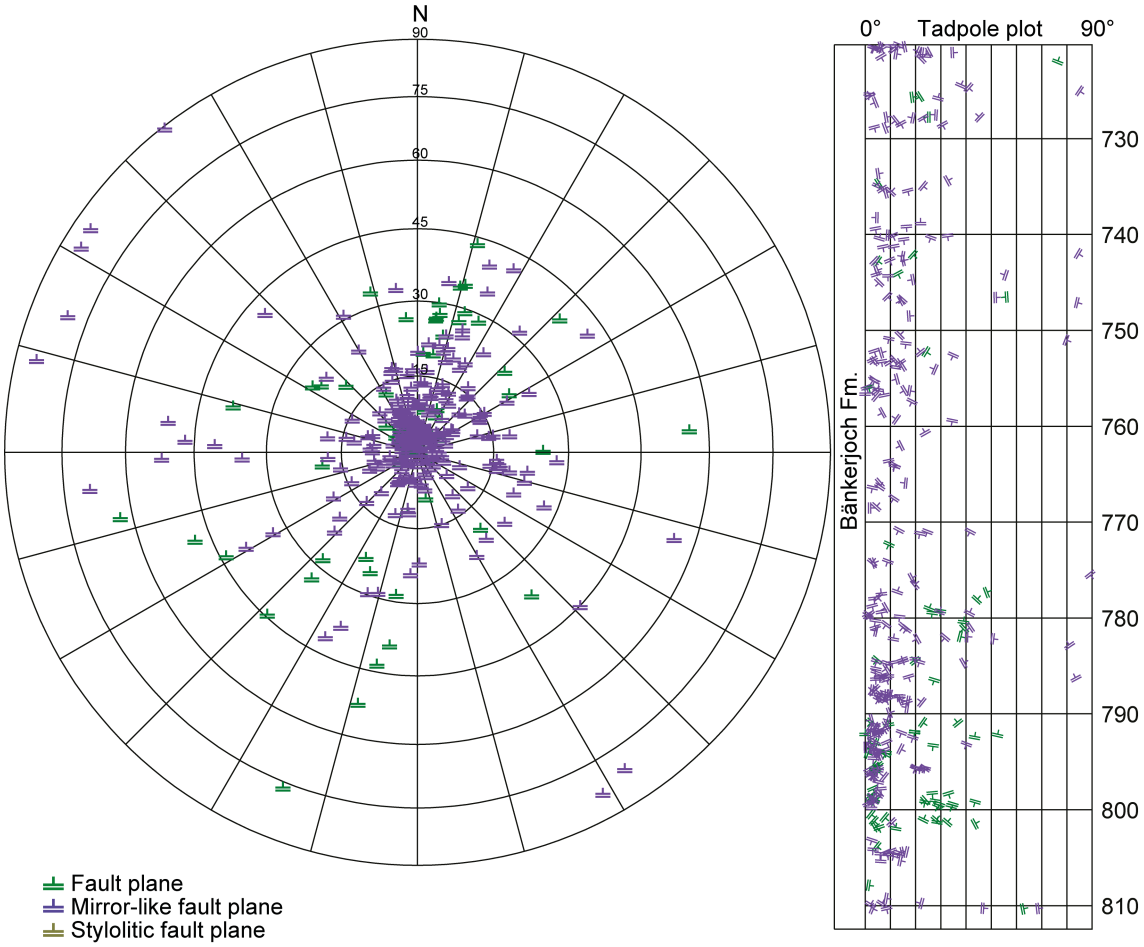


Fig. 4-50: Stereogram and depth plot of faults (Bänkerjoch Formation)

Fault planes (n = 73), mirror-like fault planes (n = 271); stylolitic fault planes were not observed (n = 0).

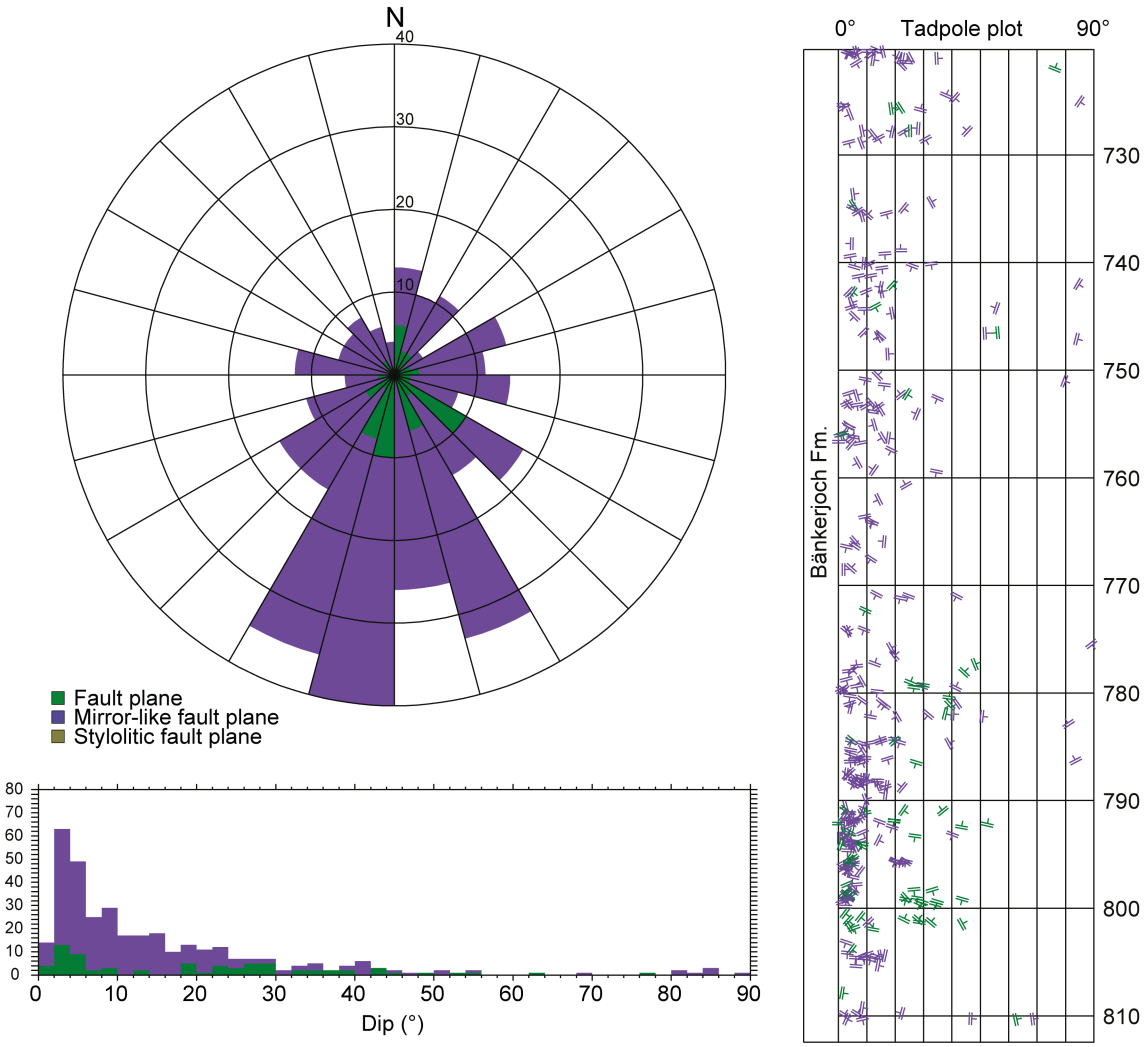


Fig. 4-51: Dip azimuth rose diagram, dip histogram and depth plot of faults (Bänkerjoch Formation)

Fault planes (n = 73), mirror-like fault planes (n = 271); stylolitic fault planes were not observed (n = 0).

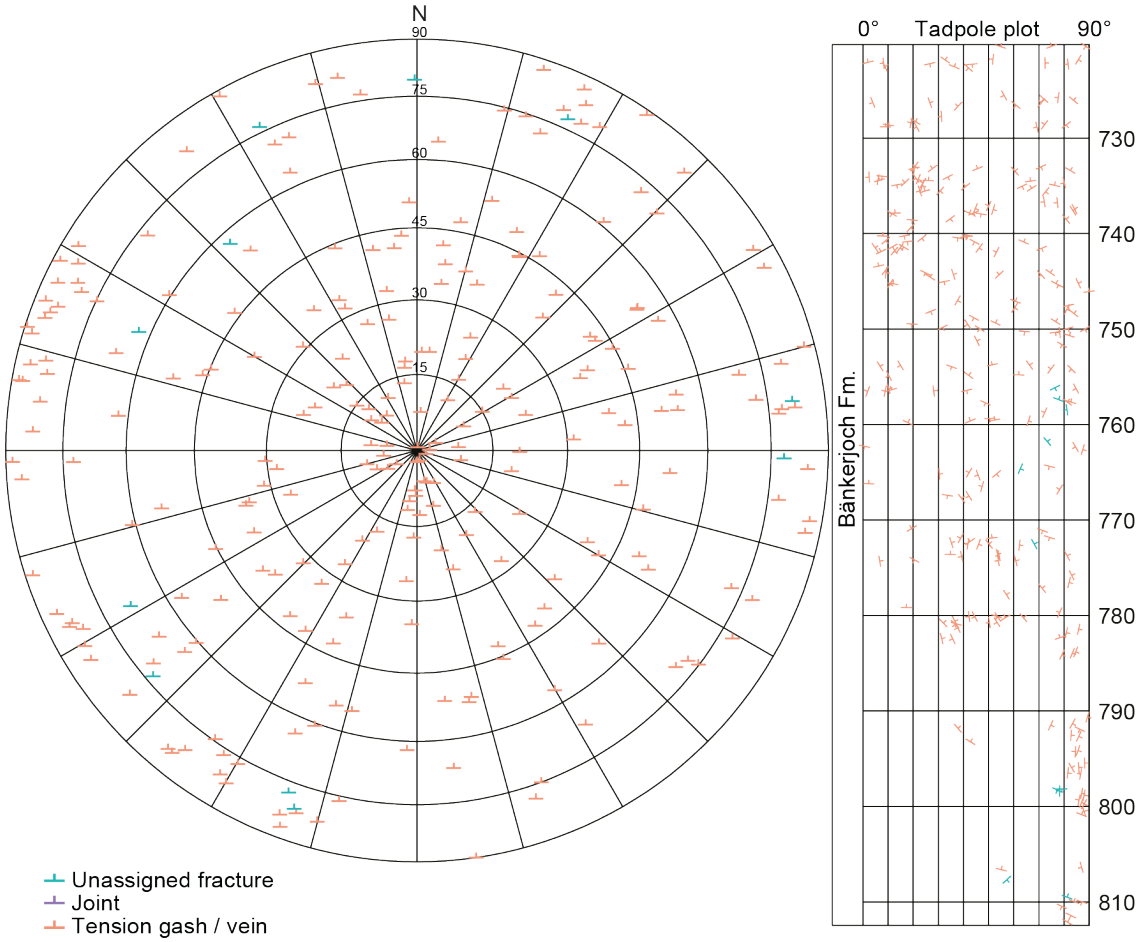


Fig. 4-52: Stereogram and depth plot of tension gashes / veins, joints and unassigned fractures (Bänkerjoch Formation)

Unassigned fractures (n = 11), tension gashes / veins (n = 252); joints were not observed (n = 0).

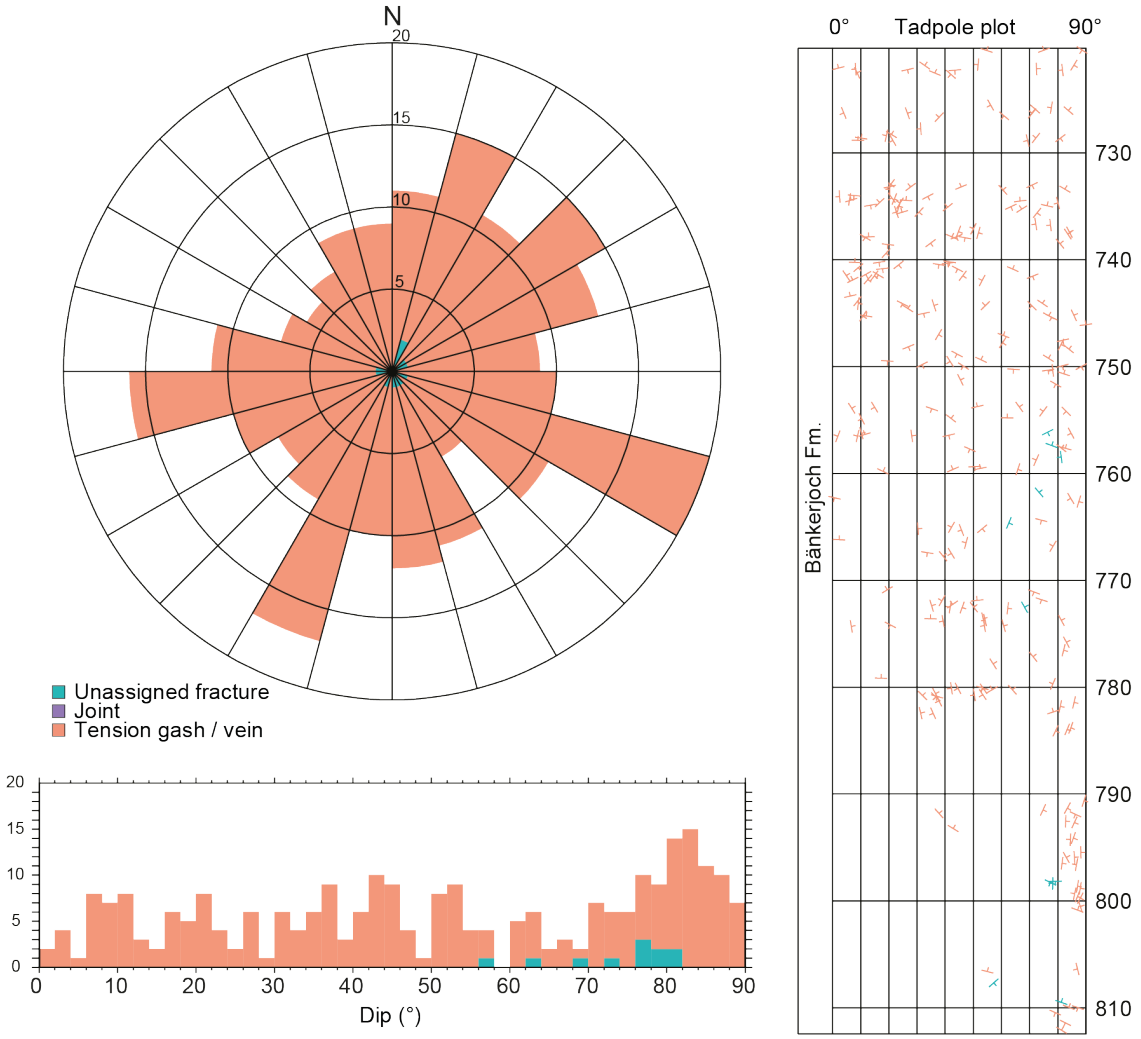


Fig. 4-53: Dip azimuth rose diagram, dip histogram and depth plot of tension gashes / veins, joints and unassigned fractures (Bänkerjoch Formation)

Unassigned fractures (n = 11), tension gashes / veins (n = 252); joints were not observed (n = 0).

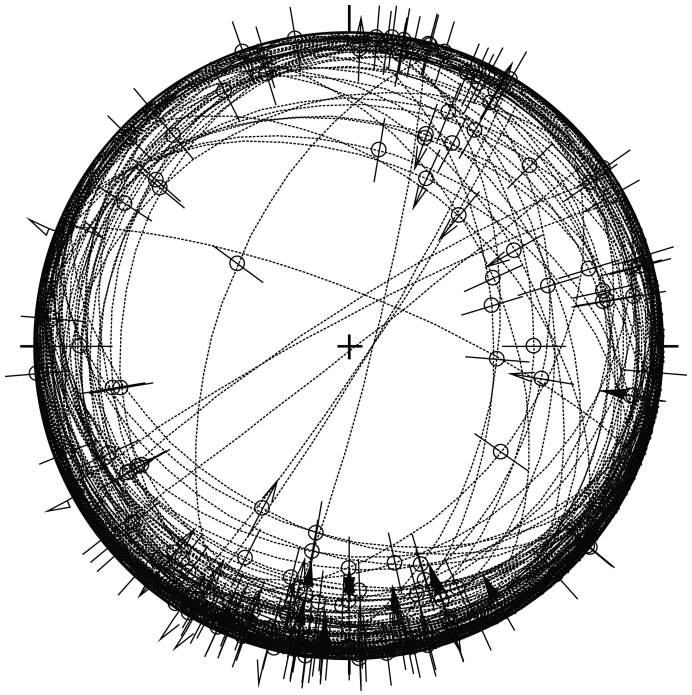


Fig. 4-54: Stereogram of fault planes with striations, including multiple lineations on a single fault plane (Bänkerjoch Formation; n = 169)

4.6 Muschelkalk

The Muschelkalk (812.45 m to 967.70 m MD log depth) shows a high density of all structure types. The dominant structures are fault planes followed by stylolites and veins / unassigned fractures. In addition, an abundance of mm- to cm-sized open pores (vugs) was observed. Only the data from oriented cores are presented.

4.6.1 Schinznach Formation

The orientations and spatial distributions of structures observed in the Schinznach Formation (812.45 m to 876.05m MD log depth) are shown in Figs. 4-55 to 4-61. The Schinznach Formation displays a high density of all structure types. While the fault planes and stylolites mostly have shallow dip angles towards the SSE, unassigned fractures and tension gashes show a predominant subvertical dip directed towards the N.

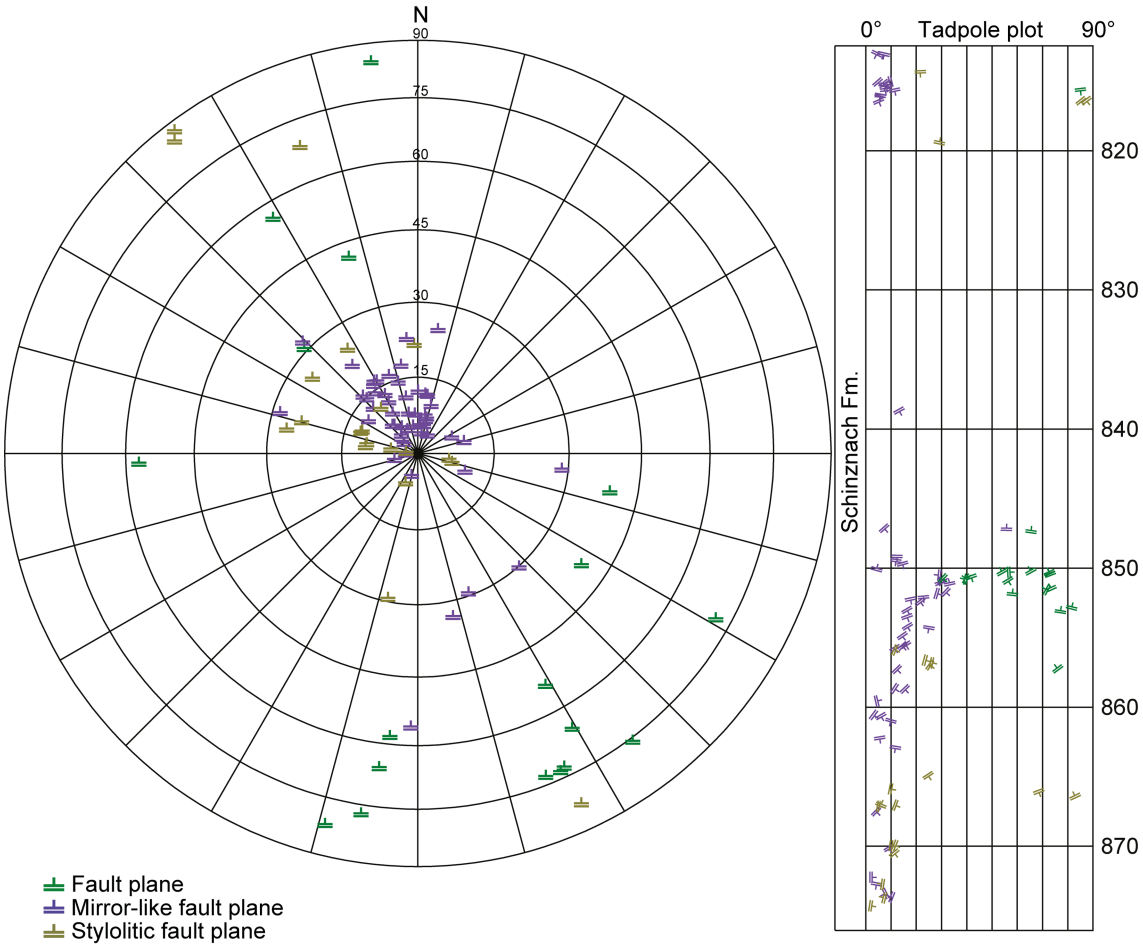


Fig. 4-55: Stereogram and depth plot of fault planes (Schinznach Formation)

Fault planes (n = 18), mirror-like fault planes (n = 52) and stylolitic fault planes (n = 21).

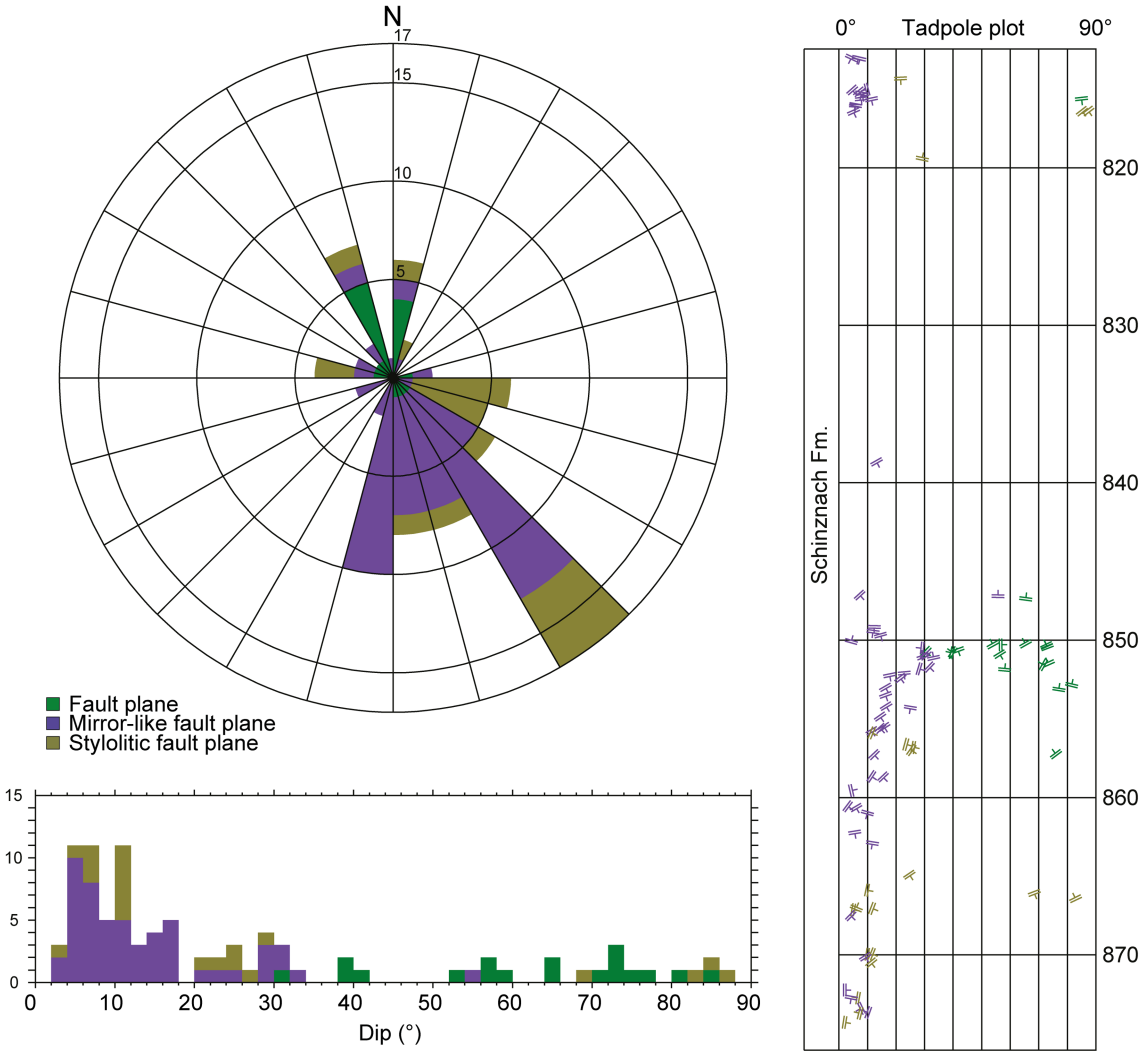


Fig. 4-56: Dip azimuth rose diagram, dip histogram and depth plot of fault planes (Schinznach Formation)

Fault planes (n = 18), mirror-like fault planes (n = 52) and stylolitic fault planes (n = 21).

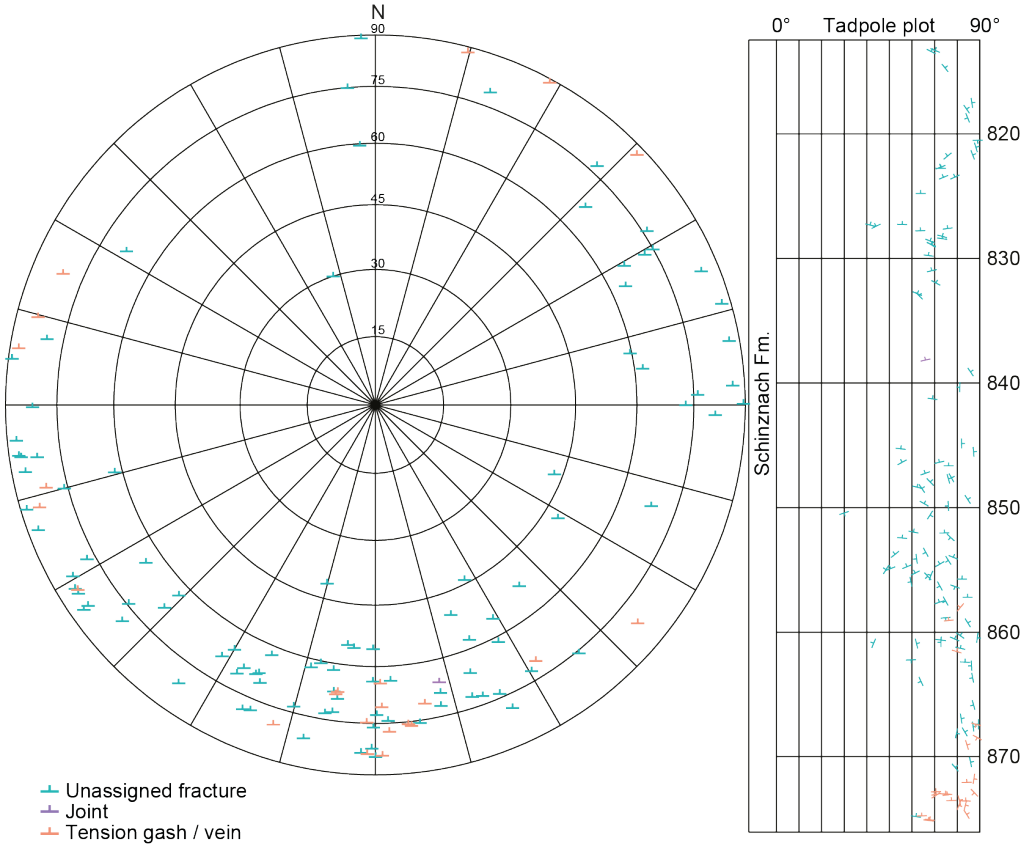


Fig. 4-57: Stereogram and depth plot of tension gashes / veins, joints and unassigned fractures (Schinznach Formation)

Unassigned fractures (n = 97), joints (n = 1) and tension gashes / veins (n = 23).

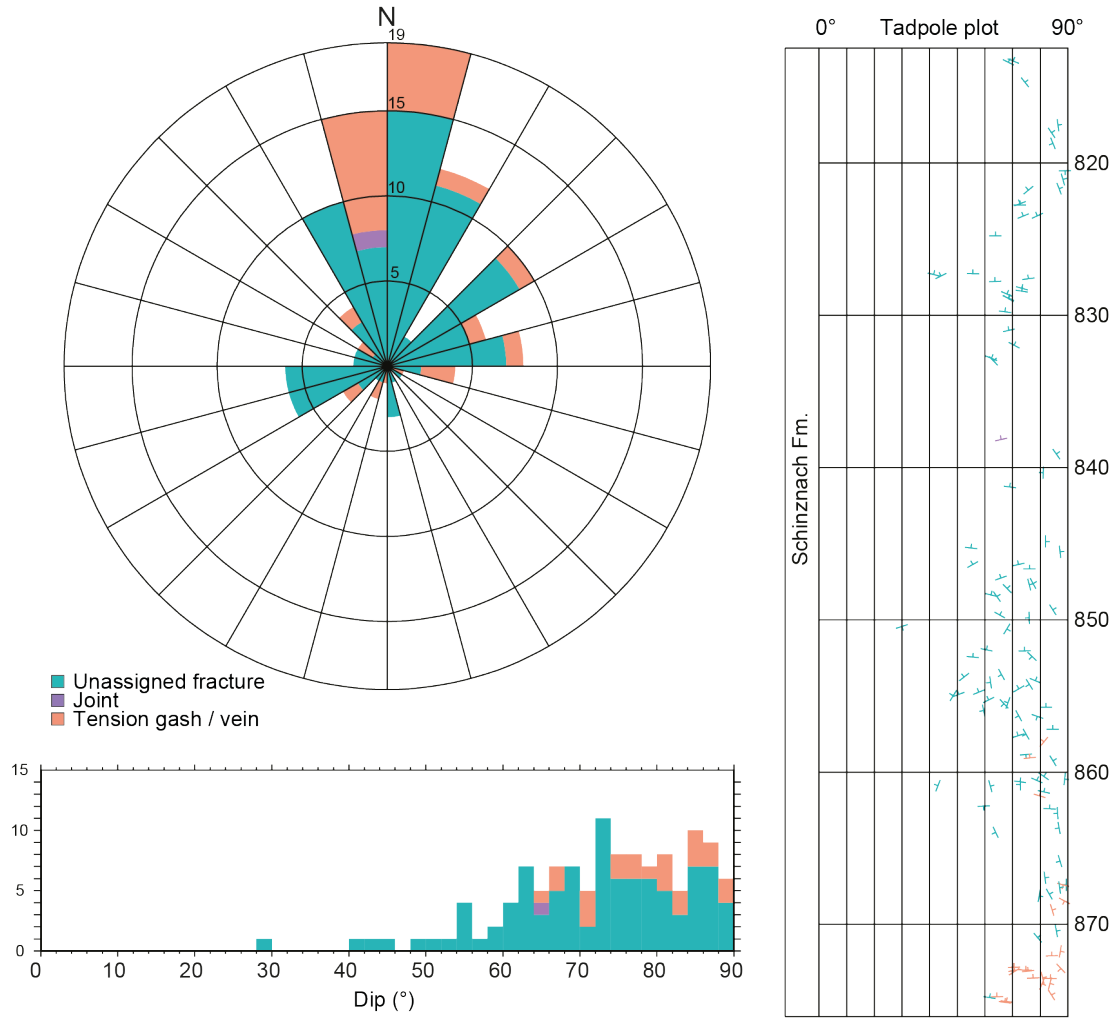


Fig. 4-58: Dip azimuth rose diagram, dip histogram and depth plot of tension gashes / veins, joints and unassigned fractures (Schinznach Formation)

Unassigned fractures (n = 97), joints (n = 1) and tension gashes / veins (n = 23).

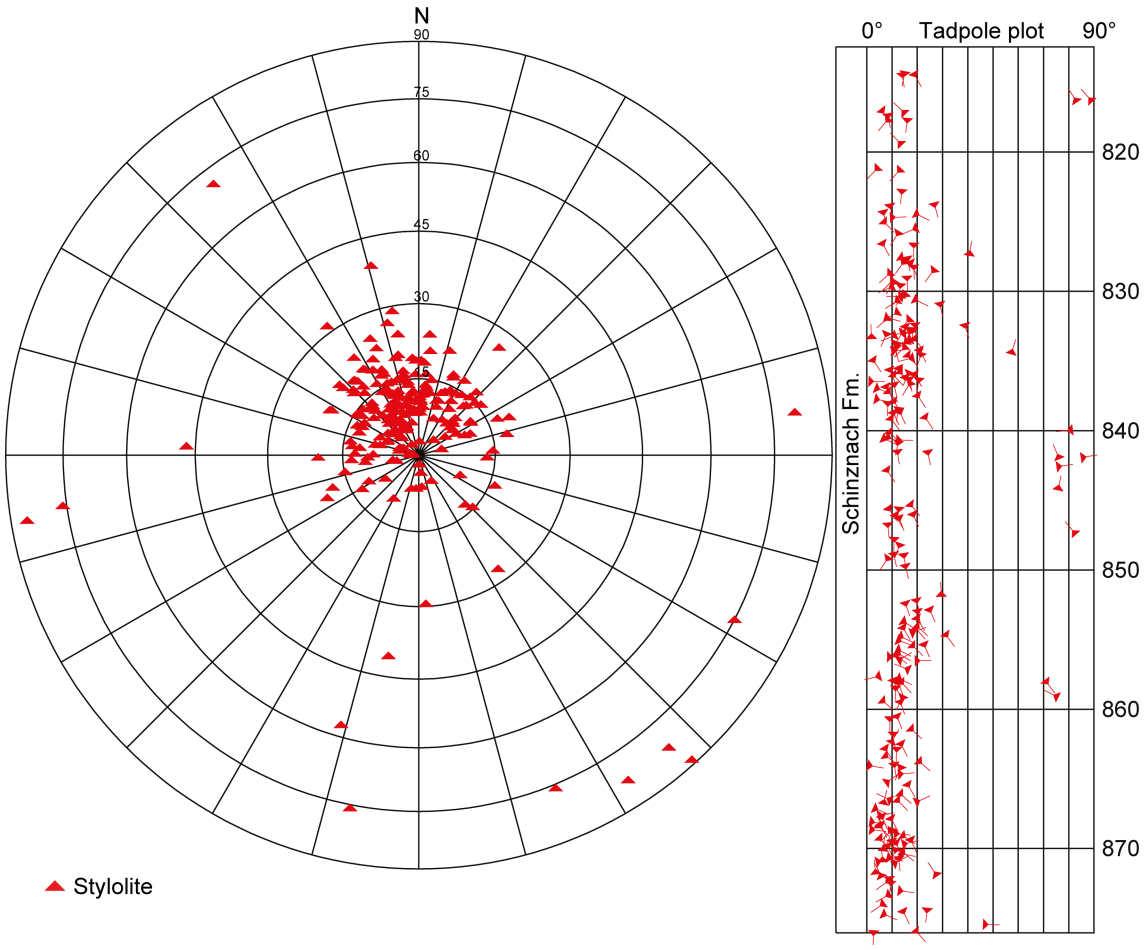


Fig. 4-59: Stereogram and depth plot of stylolites (Schinznach Formation; n = 219)

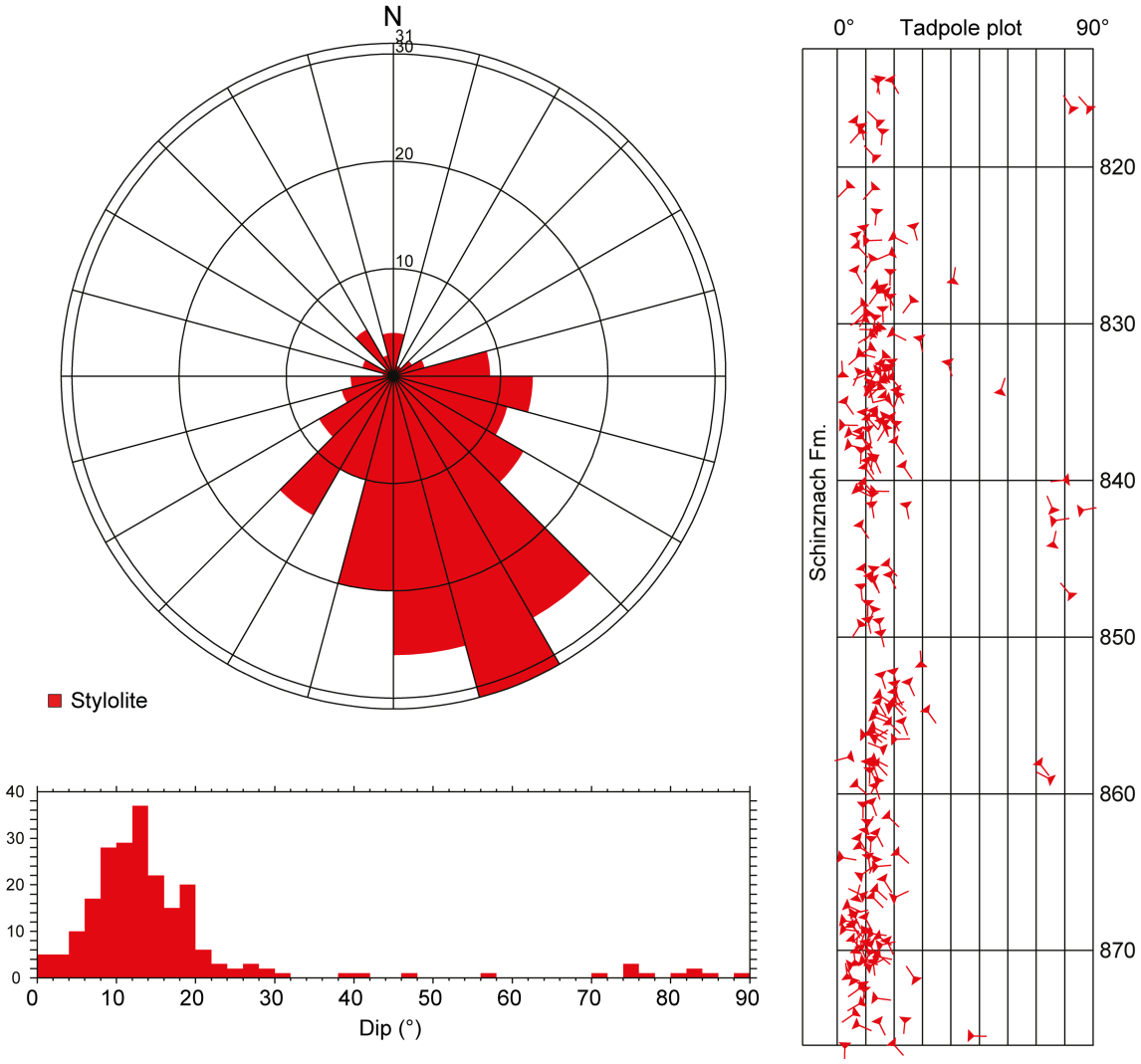


Fig. 4-60: Dip azimuth rose diagram, dip histogram and depth plot of stylolites (Schinznach Formation; n = 219)

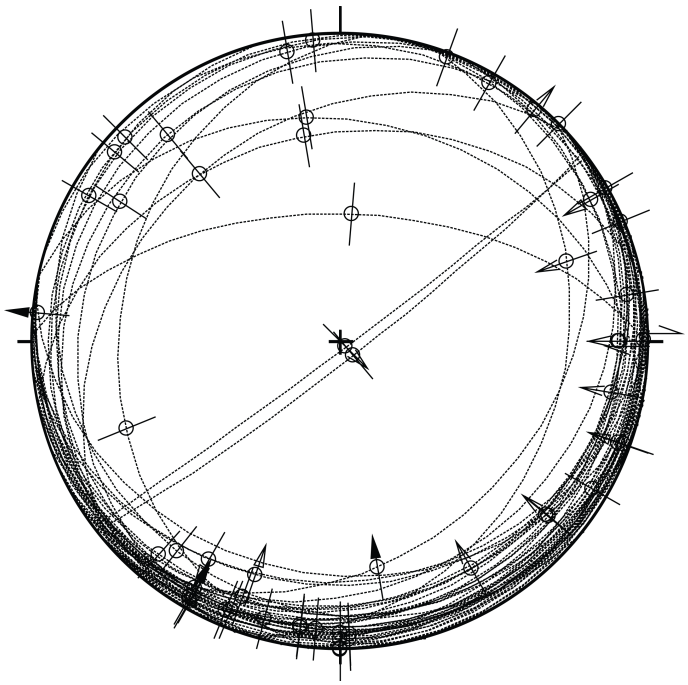


Fig. 4-61: Stereogram of fault planes with striations, including multiple lineations on a single fault plane (Schinznach Formation; n = 52)

4.6.2 Zeglingen Formation

The orientation and spatial distribution of the structures observed in the Zeglingen Formation (876.05 m to 922.30 m MD log depth) are shown in Figs. 4-62 to 4-67. This formation is rich in fault planes and veins. The structures are concentrated in the upper half of the formation where they are evenly distributed. They show no obvious preferred orientation.

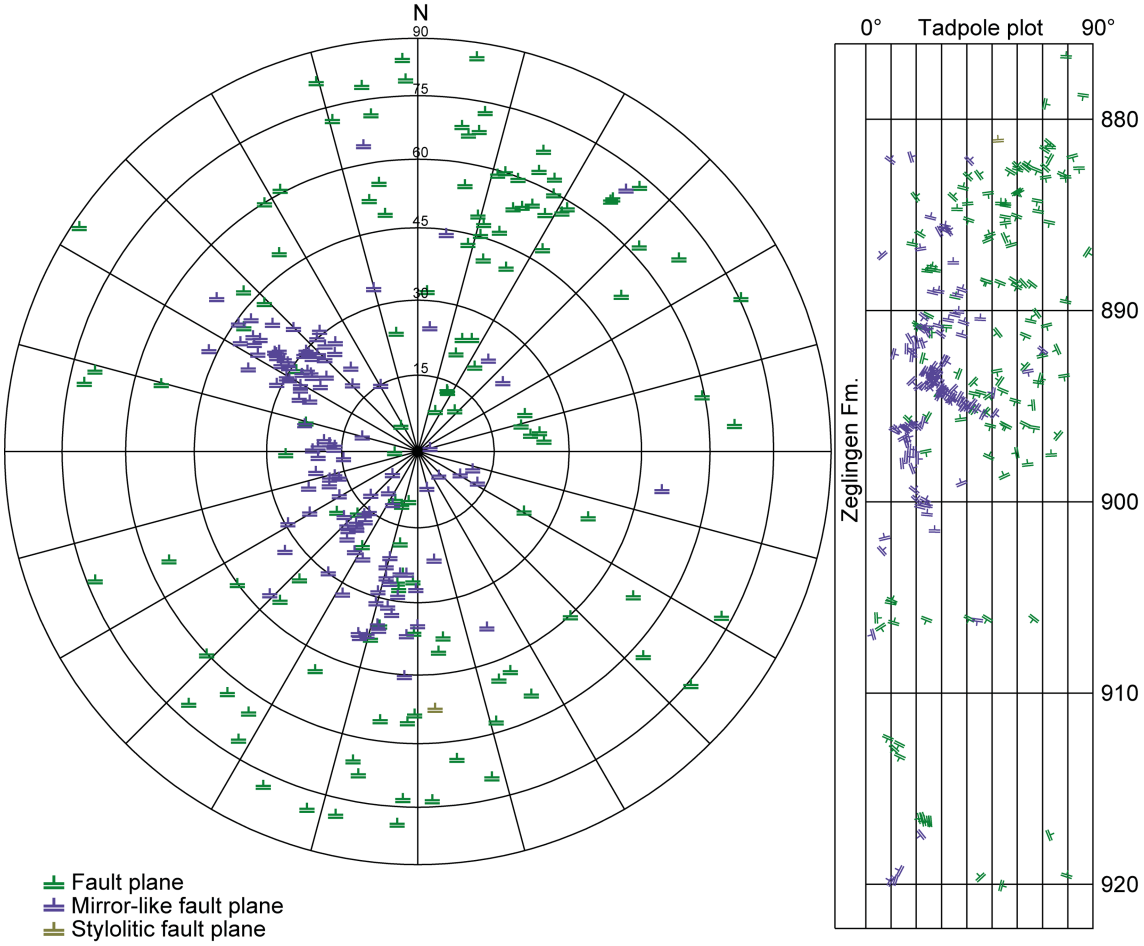


Fig. 4-62: Stereogram and depth plot of fault planes (Zeglingen Formation)

Fault planes (n = 126), mirror-like fault planes (n = 125) and stylolitic fault planes (n = 1).

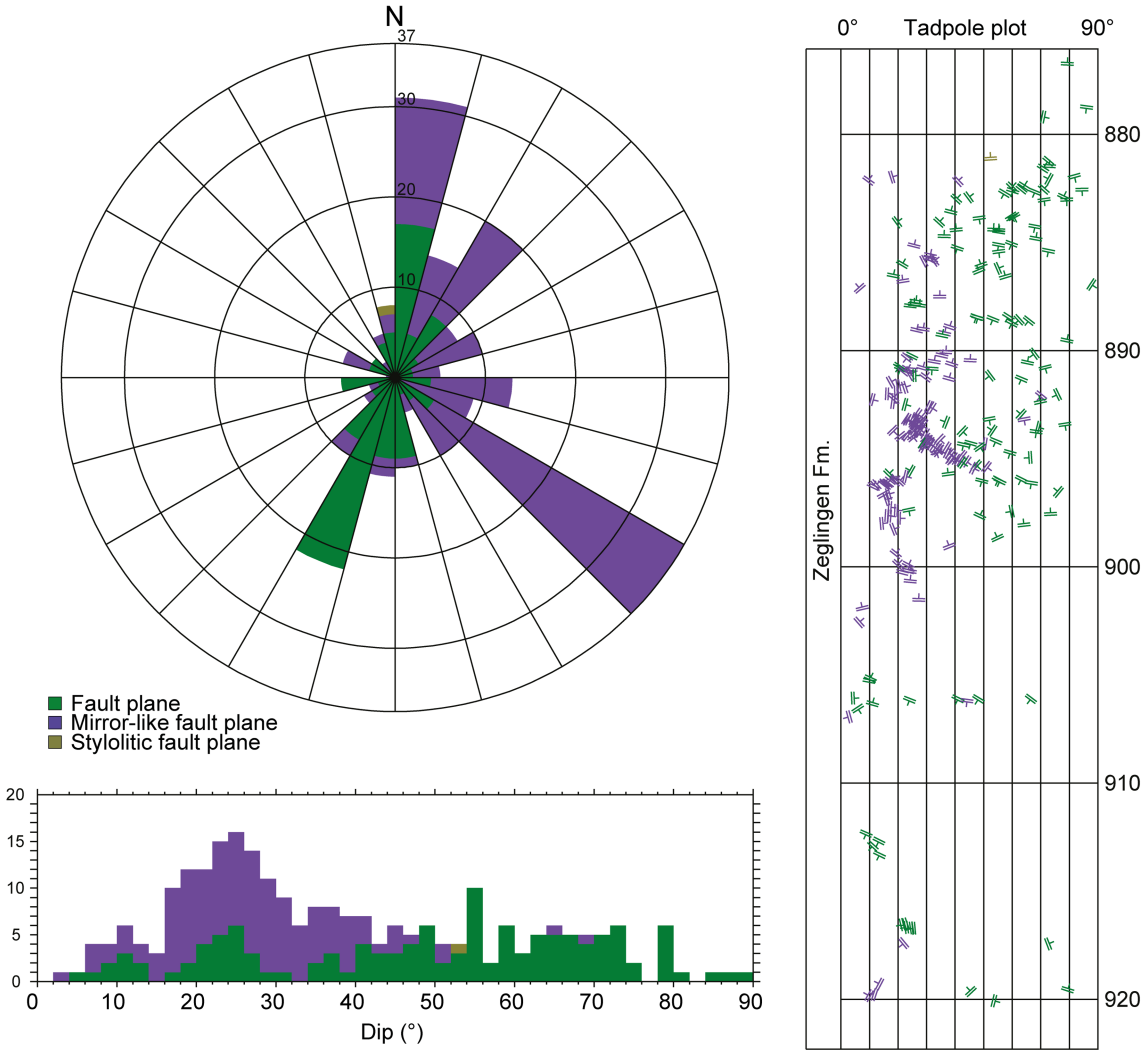


Fig. 4-63: Dip azimuth rose diagram, dip histogram and depth plot of fault planes (Zeglingen Formation)

Fault planes (n = 126), mirror-like fault planes (n = 125) and stylolitic fault planes (n = 1).

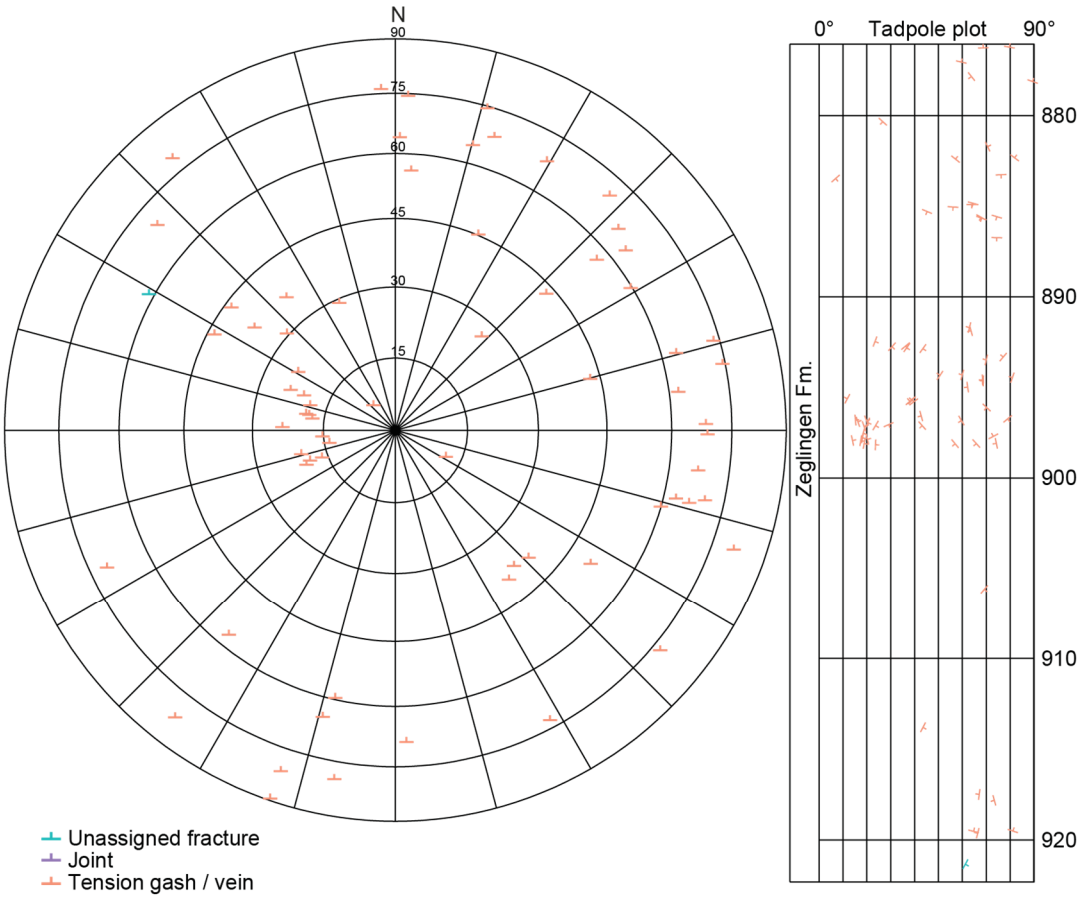


Fig. 4-64: Stereogram and depth plot of tension gashes / veins, joints and unassigned fractures (Zeglingen Formation)

Unassigned fractures (n = 1), tension gashes / veins (n = 68); joints were not observed (n = 0).

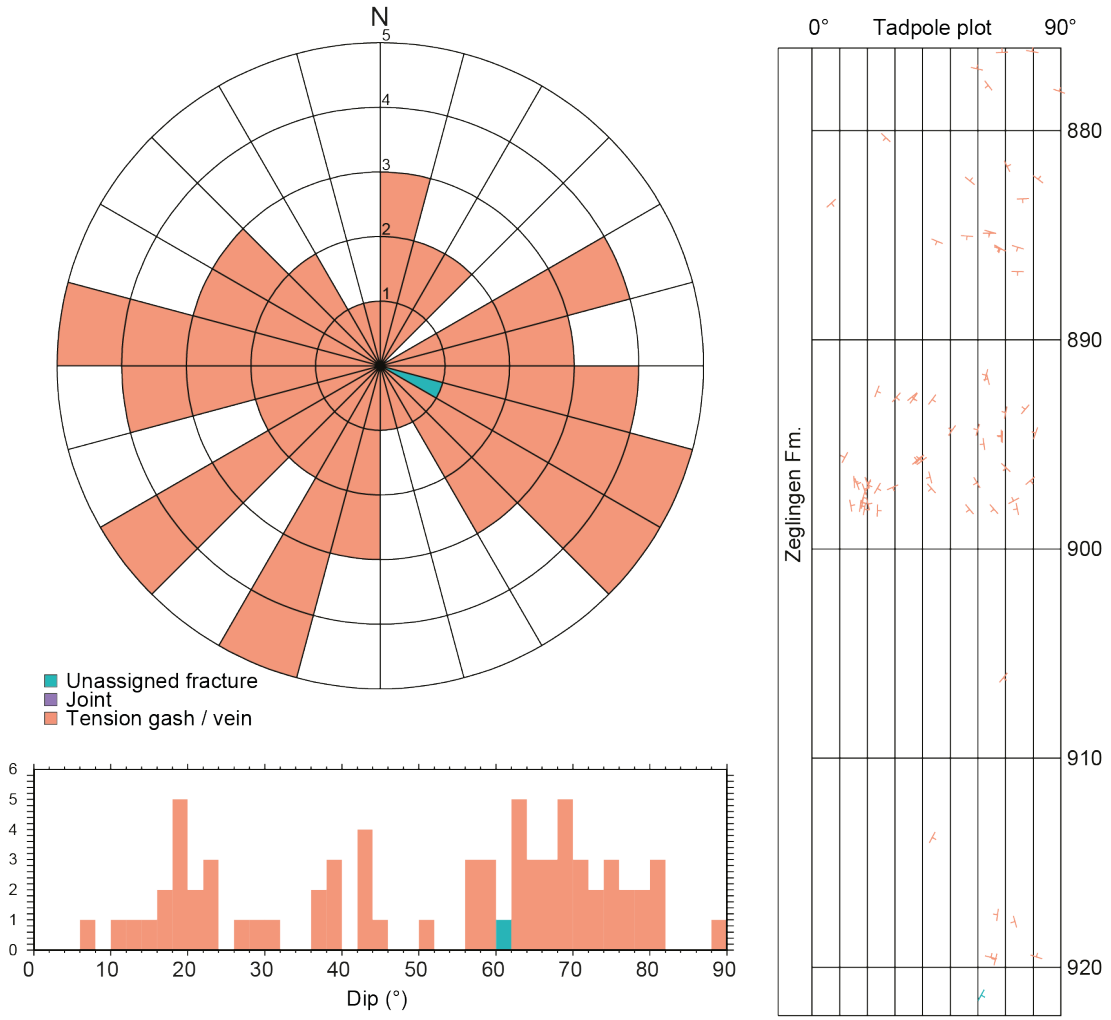


Fig. 4-65: Dip azimuth rose diagram, dip histogram and depth plot of tension gashes / veins, joints and unassigned fractures (Zeglingen Formation)

Unassigned fractures (n = 1), tension gashes / veins (n = 68); joints were not observed (n = 0).

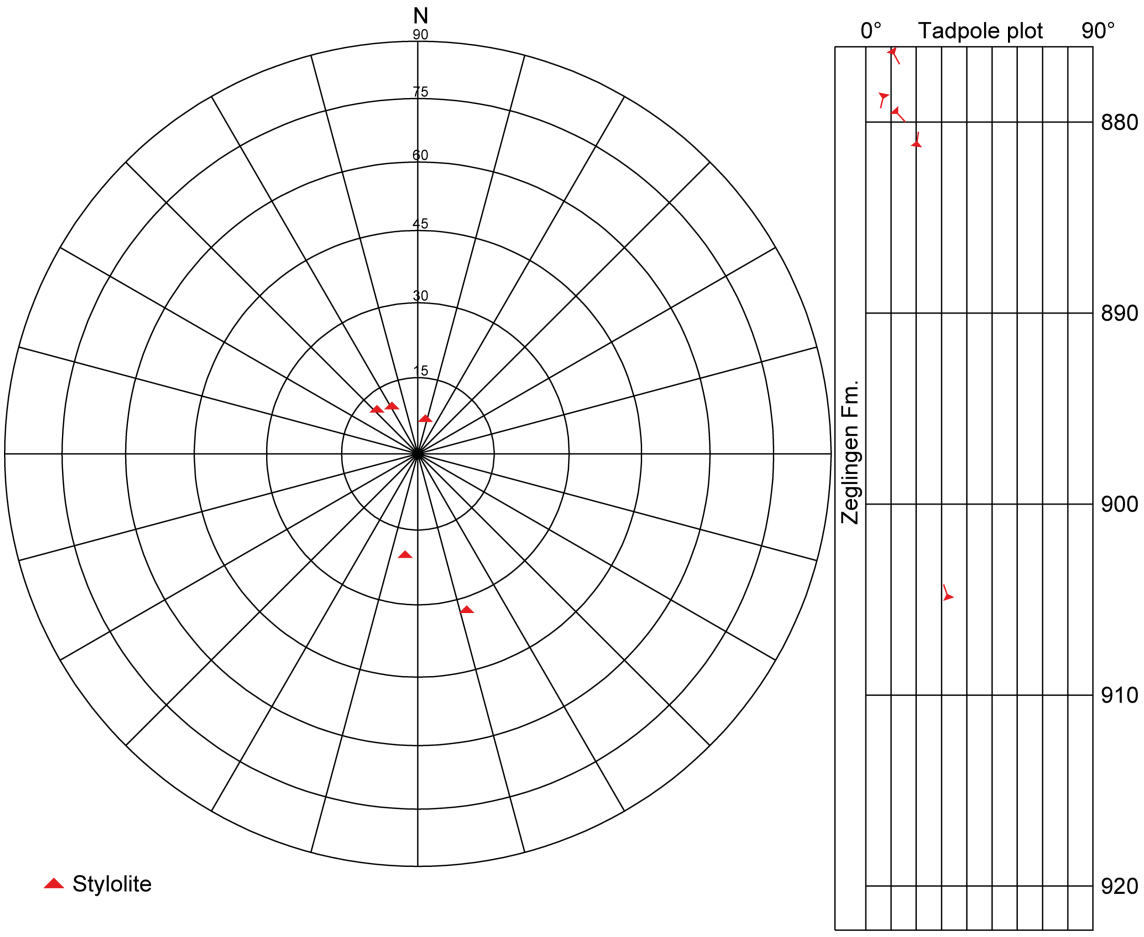


Fig. 4-66: Stereogram and depth plot of stylolites (Zeglingen Formation; n = 5)

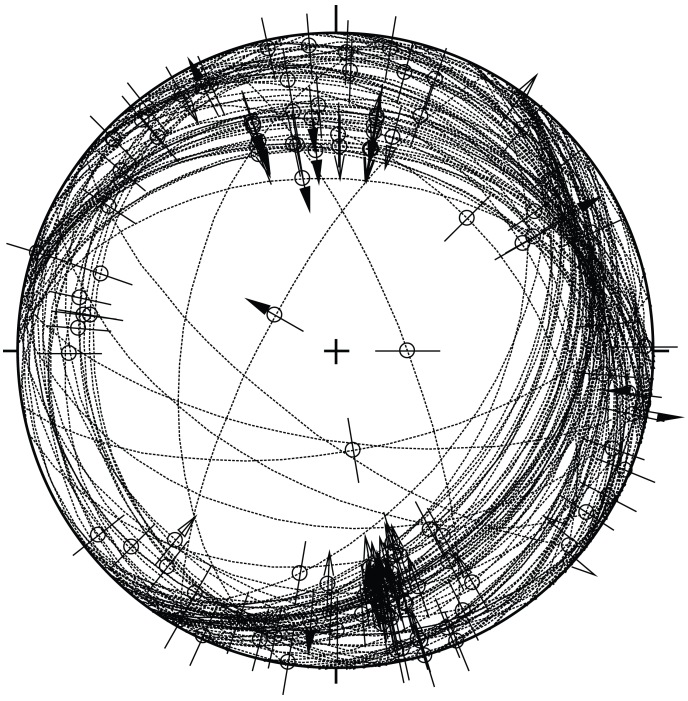


Fig. 4-67: Stereogram of fault planes with striations, including multiple lineations on a single fault plane (Zeglingen Formation; n = 132)

4.6.3 Kaiseraugst Formation

The orientations and spatial distributions of the structures observed in the Kaiseraugst Formation (922.30 m to 967.70 m MD log depth) are shown in Figs. 4-68 to 4-71. The dominant structures are mirror-like fault planes. They mostly show shallow dip angles and dip towards the E, S and W. Stylolites are absent.

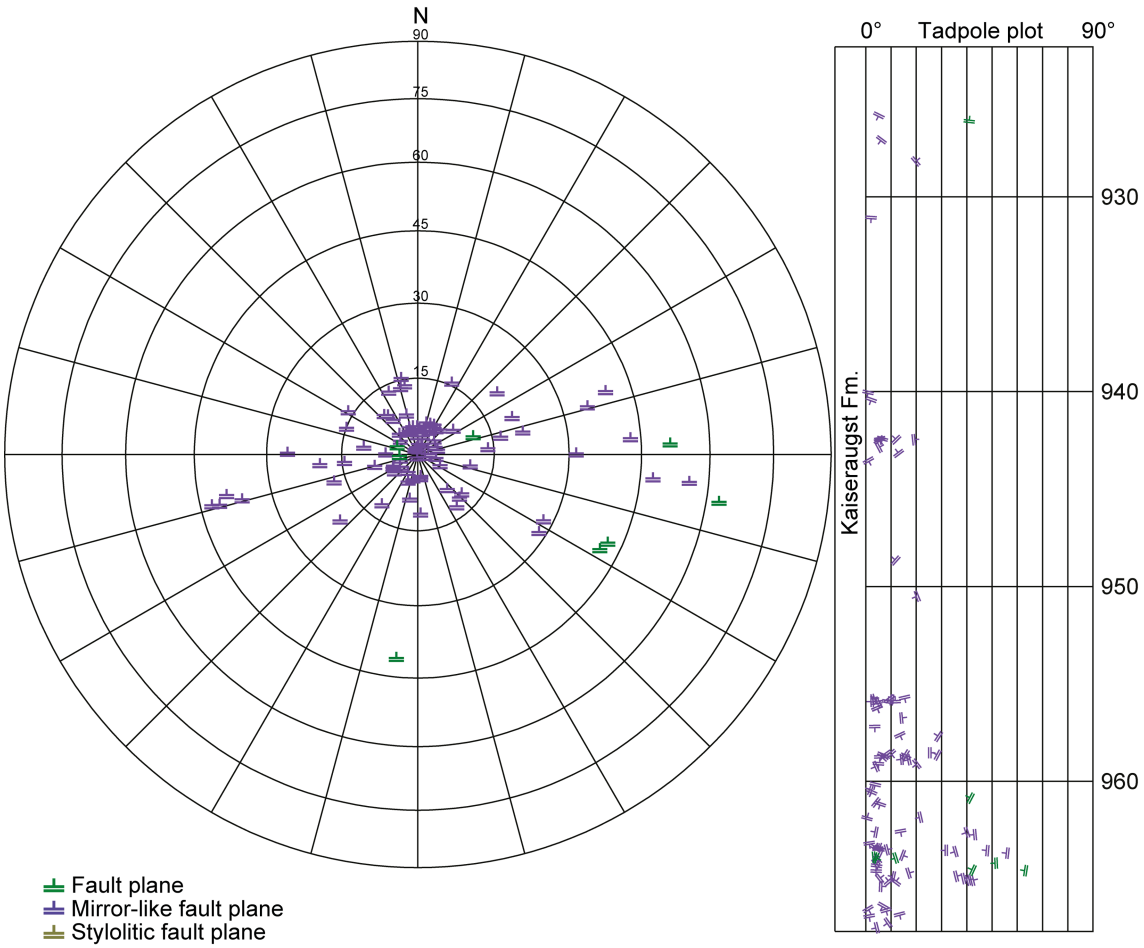


Fig. 4-68: Stereogram and depth plot of fault planes (Kaiseraugst Formation)

Fault planes (n = 8), mirror-like fault planes (n = 90); stylolitic fault planes were not observed (n = 0).

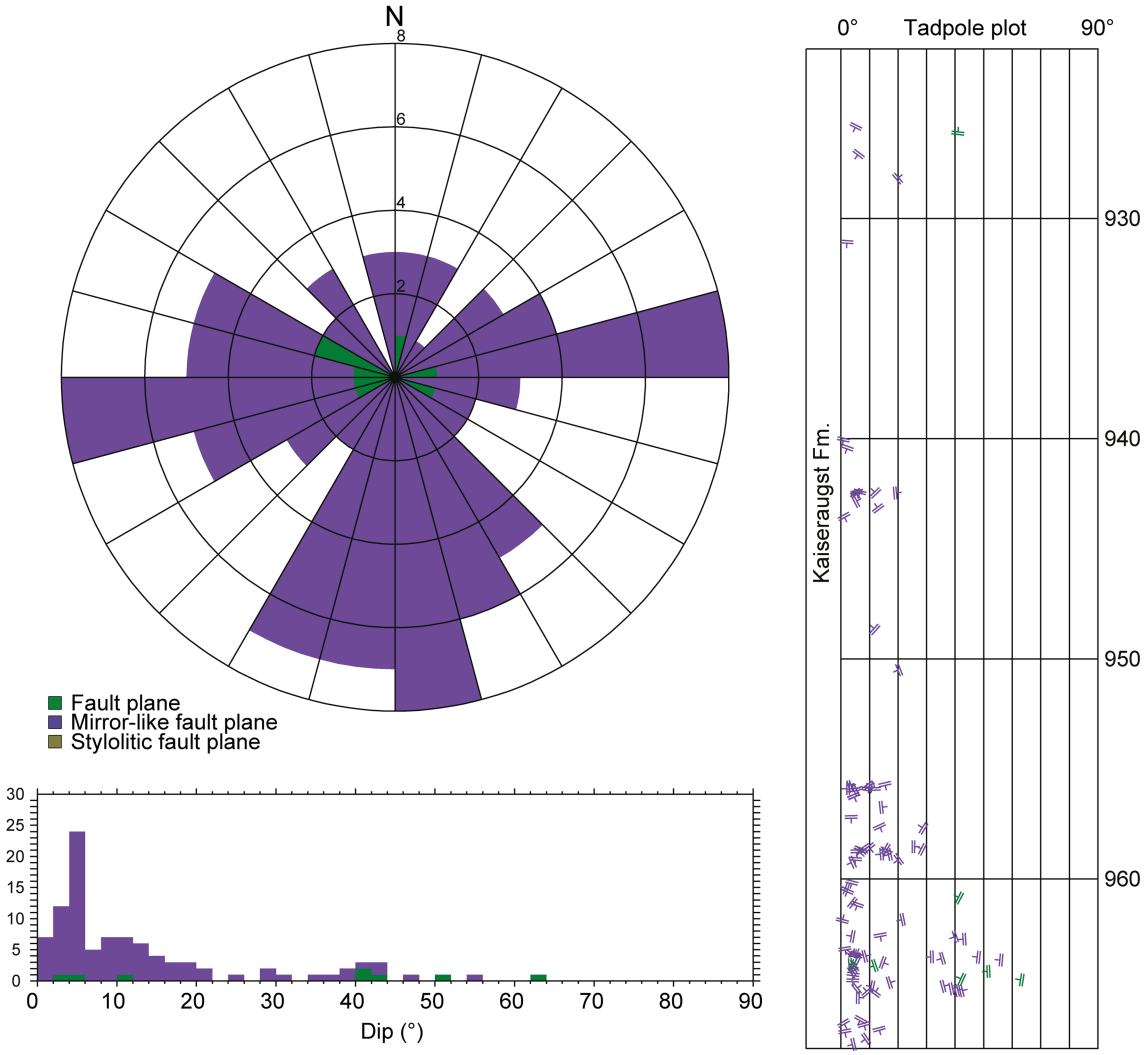


Fig. 4-69: Dip azimuth rose diagram, dip histogram and depth plot of fault planes (Kaiseraugst Formation)

Fault planes (n = 8), mirror-like fault planes (n = 90); stylolitic fault planes were not observed (n = 0).

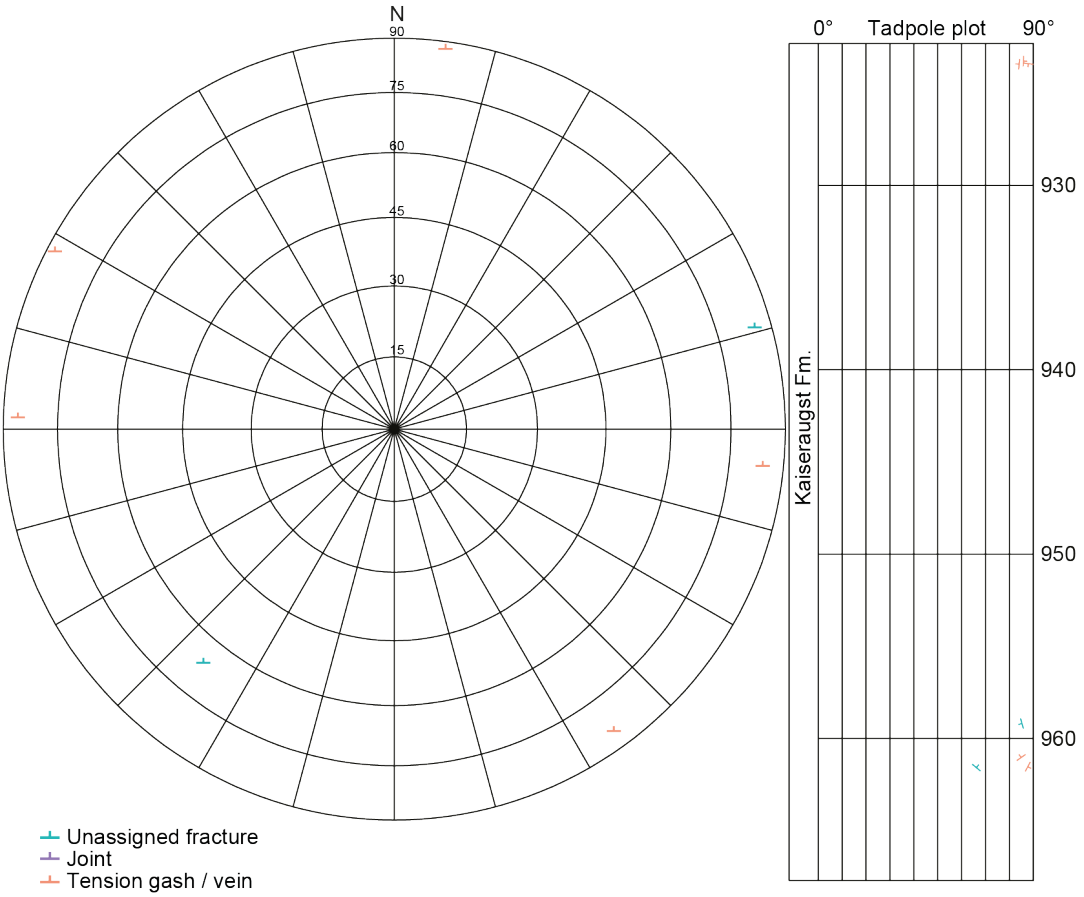


Fig. 4-70: Stereogram and depth plot of tension gashes / veins, joints and unassigned fractures (Kaiseraugst Formation)

Unassigned fractures (n = 2), tension gashes / veins (n = 5); joints were not observed (n = 0).

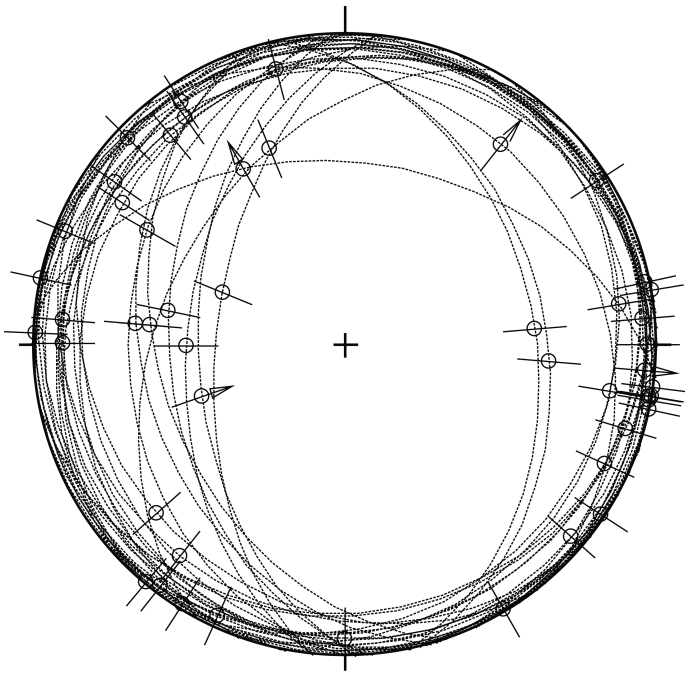


Fig. 4-71: Stereogram of fault planes with striations, including multiple lineations on a single fault plane (Kaiseraugst Formation; n = 45)

4.7 Dinkelberg Formation and Weitenau Formation

The orientation and spatial distribution of the structures observed in the Dinkelberg Formation and Weitenau Formation (967.70 m to 1'037.31 m MD log depth; base of cored section) are shown in Figs. 4-72 to 4-74. This zone is characterised by a very low number of structures. Numerous mm- to cm-sized open pores / vugs were observed in the Dinkelberg Formation. Joints, tension gashes / veins and stylolites are absent.

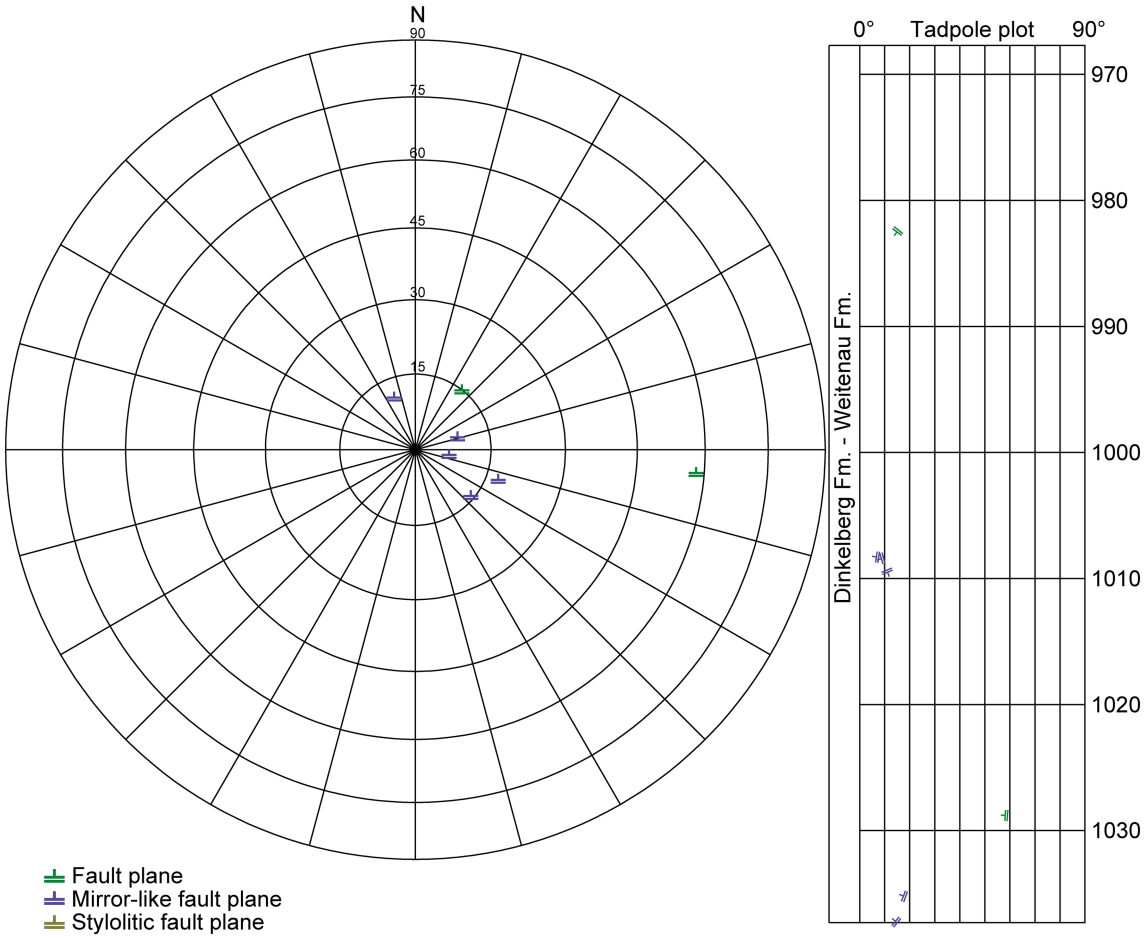


Fig. 4-72: Stereogram and depth plot of fault planes (Dinkelberg Formation and Weitenau Formation)

Fault planes (n = 2), mirror-like fault planes (n = 5); stylolitic fault planes were not observed (n = 0).

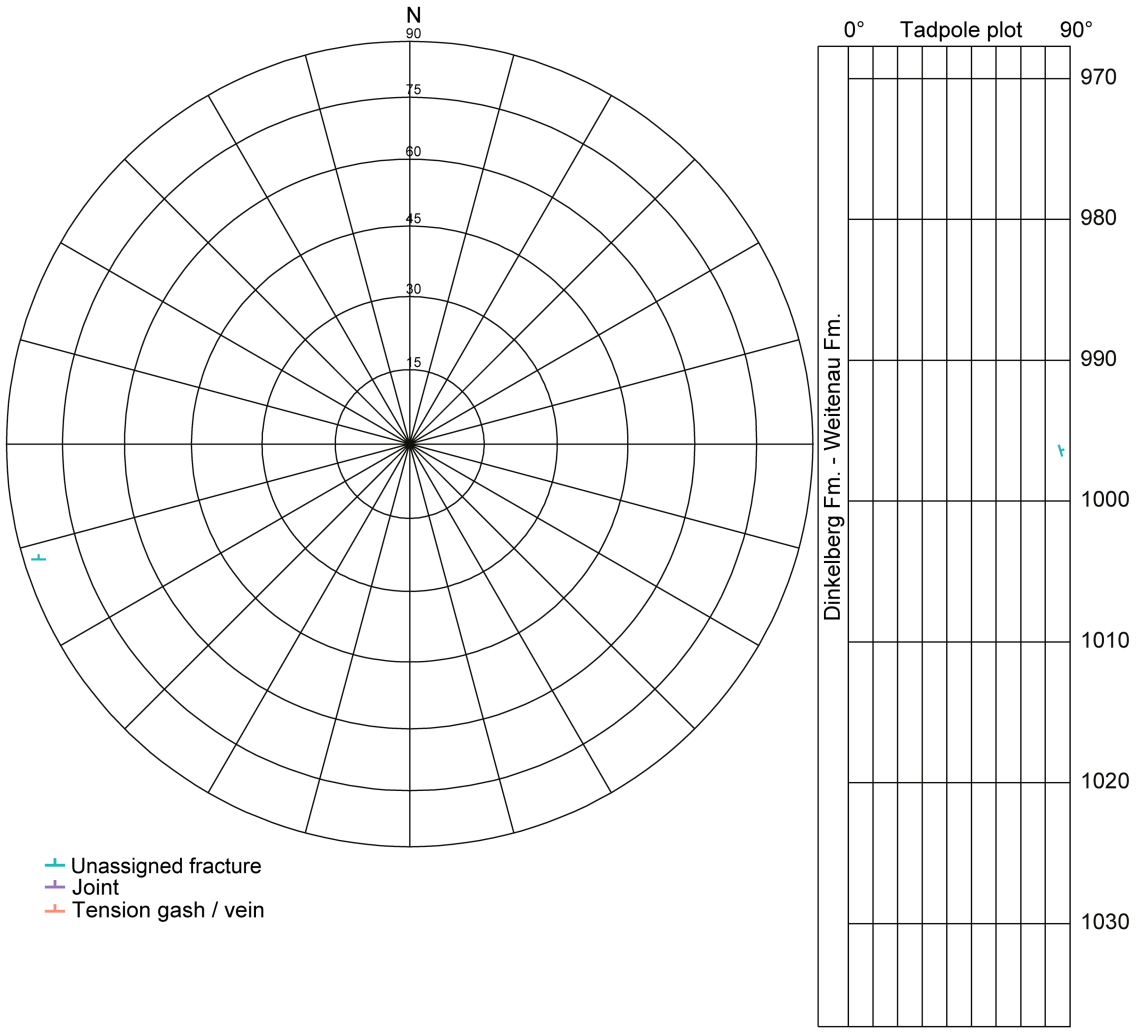


Fig. 4-73: Stereogram and depth plot of tension gashes / veins, joints and unassigned fractures (Dinkelberg Formation and Weitenau Formation)

Unassigned fractures (n = 1). Joints and tension gashes / veins were not observed (n = 0).

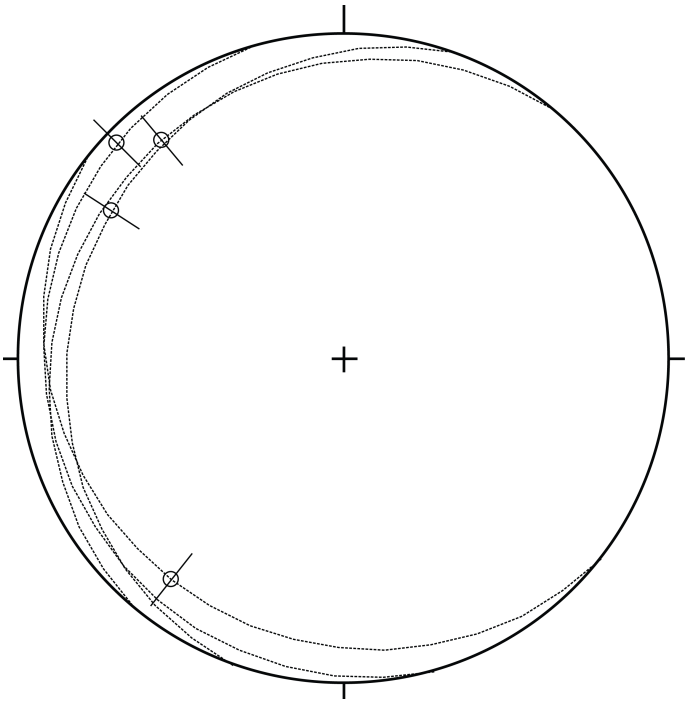


Fig. 4-74: Stereogram of fault planes with striations (Dinkelberg Formation and Weitenau Formation; n = 4)

5 Main structural findings

Among the relevant geological features within the study interval from 255.00 m to 1'037.31 m MD log depth presented in Chapters 3 and 4, a few particularly prominent structures and zones deserve a more detailed examination.

5.1 Deformed bedding within the Opalinus Clay

In the BOZ1-1 borehole, the Opalinus Clay was encountered from 530.32 m to 651.46 m MD (log depth) with a thickness of 121.14 m. This clay-rich succession is predominantly subhorizontally bedded with bedding planes dipping at angles between 1° and 5°. However, it also contains three intervals up to 7 m thick with deformed bedding (see Fig. 5-1):

- 568.90 m to 572.00 m MD (log depth)
- 600.70 m to 607.60 m MD (log depth)
- 623.90 m to 627.26 m MD (log depth)

These borehole intervals are characterised by beds with locally dipping angles of up to 65° and variable dip directions. The dip orientation often changes abruptly. Internally, the beds reveal bulls-eye structures with a sharp base and truncated upper boundaries, most likely representing soft-sediment deformation.

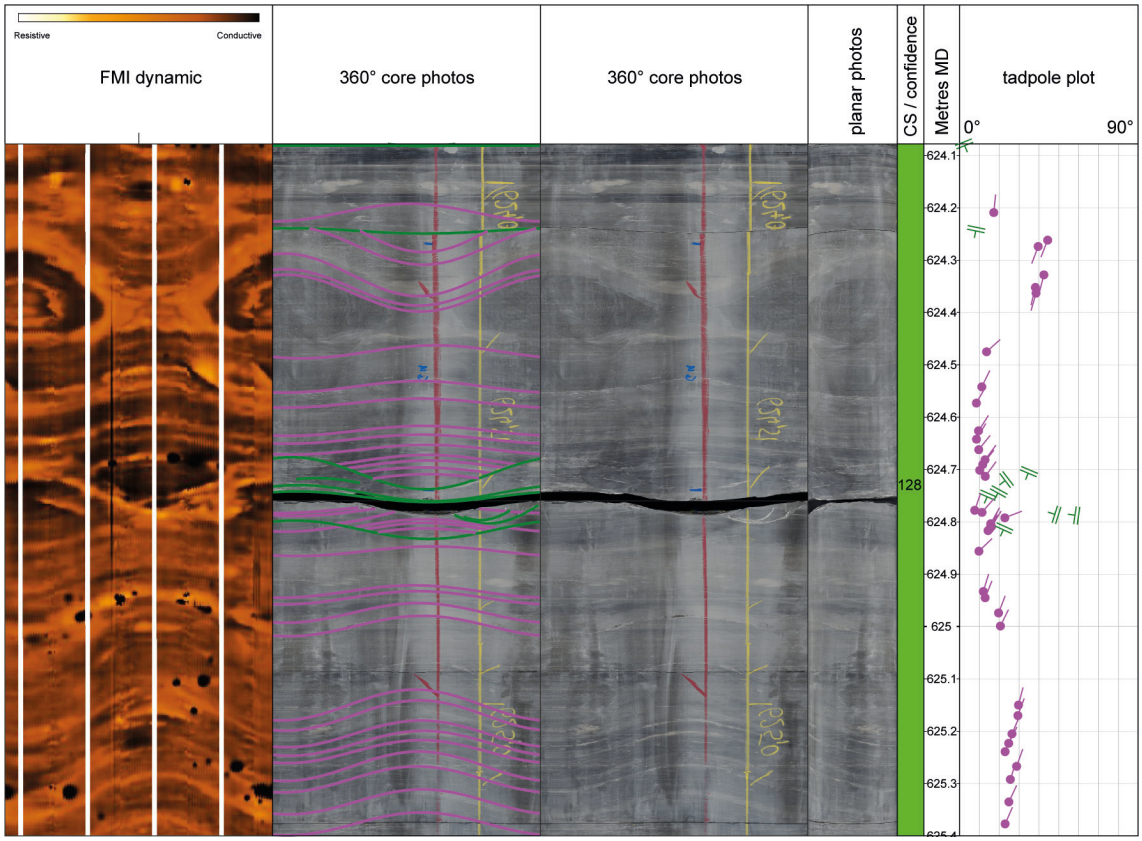


Fig. 5-1: Deformed bedding in the Opalinus Clay from 624.10 m to 625.40 m MD (log depth)

Note the bulls-eye structure at 624.40 m MD (log depth) with an erosive top and base. The latter is made clearly visible with the FMI.

5.2 Fault zone within the Schinznach Formation

A prominent fault zone is present in the carbonates of the Schinznach Formation from 850.27 m to 851.52 m MD (log depth) in BOZ1-1. The top and bottom are defined by prominent fault planes which dip steeply towards the NW (65° dip at the top and 73° at the bottom), truncating the bedding (Fig. 5-2). This 1.25 m thick fault zone is composed of dilation and stylolitic breccias with synkinematic calcite mineralisation. In total, 18 planar structures were recorded in this fault zone: mostly fault planes (n = 12), followed by mirror-like fault planes (n = 4) and unassigned fractures (n = 2). The stereogram in Fig. 5-3 shows a clear predominance of planes dipping towards the NNW to NW as well as towards the SSE. Their dip angles vary from inclined to subvertical (30° to 75°).

In addition to faults, abundant large open pores (up to 20 mm wide and 45 mm long) with idiomorphic mm-sized calcite crystals are also common. In the FMI image, some faults as well as the open pores show a conductive image response confirming their open character (Fig. 5-2).

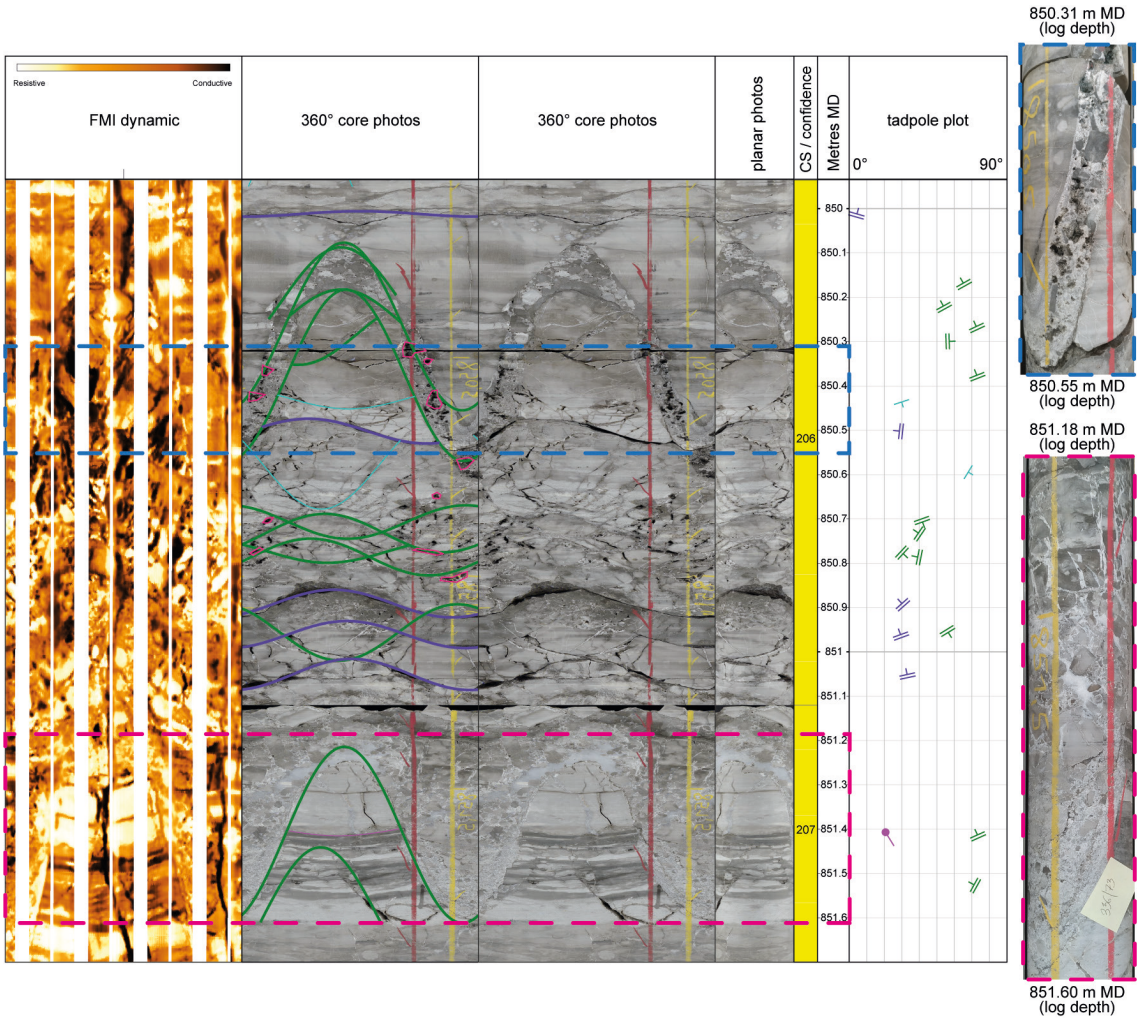


Fig. 5-2: Overview plot of the fault zone within the Schinznach Formation at 850.27 m to 851.52 m MD (log depth) in BOZ1-1

This fault zone is delimited by 65° and 73° NW-dipping fault planes at the top and bottom. In the drill cores it is composed of dilation and stylolitic breccias with synkinematic calcite mineralisation (e.g. red dashed square) and abundant open pores with idiomorphic calcite cristals (blue dashed square).

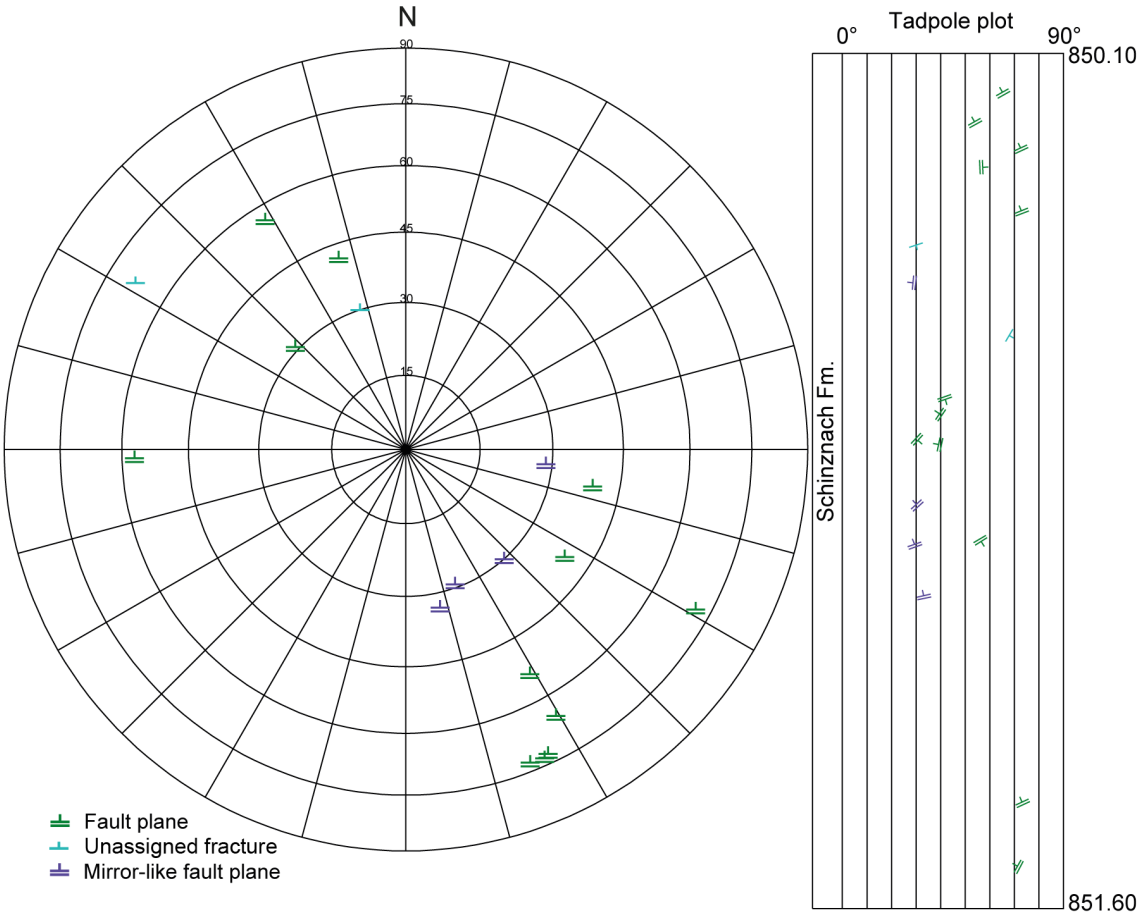


Fig. 5-3: Stereogram with interpreted structures in the fault zone from 850.27 m to 851.52 m MD (log depth).

Fault planes (n = 12), mirror-like fault planes (n = 4) and unassigned fractures (n = 2).

5.3 Fault zone within the Zeglingen Formation

A prominent 31.79 m thick fault zone with viscose deformation was interpreted within the Zeglingen Formation from 883.75 m to 915.54 m MD (log depth). This zone is flanked by brittle deformation above (from 881.05 m to 883.75 m MD log depth) and below (from 915.54 m to 922.30 m MD log depth). The fault zone is composed of faintly laminated to well bedded dolostone, anhydrite and claystone. This borehole section is characterised by disturbed bedding with variable dip magnitudes ranging from subhorizontal to about 70° and scattered dip azimuths (see Fig. 5-4). The most prominent structural dips change abruptly and coincide with faults, e.g. at 890.80 m MD (log depth) and at 895.80 m MD (log depth). In addition, gradual changes in dip angle also occur, e.g. from 891.00 m to 895.80 m MD (log depth), and may be related to folding and/or fault drag deformation (see Fig. 5-4). A potential subhorizontal and roughly SW-NE striking fold axis was interpreted at 907.37 m MD (log depth).

In the drill cores, most fault planes (n = 116) are mineralised with synkinematic anhydrite reaching up to 25 mm in thickness. In addition, abundant mirror-like fault planes reveal mm-thick anhydrite mineralisation. The faults are commonly associated with bedding offsets at a mm- to cm-scale, but never exceeding 5 cm. A number of fault rock fabrics such as fault breccia, dilation breccia, cataclasites and shear bands were observed in drill cores, indicating a strong tectonic overprint (examples are provided in Fig. 5-5). In addition, locally complex shear zones associated with dilation breccia filled with anhydrite as well as folded and thrusted beds were interpreted, e.g. from 895.21 m to 895.98 m MD log depth (Fig. 5-5). Furthermore, indications for a ductile shear deformation associated with foliation and rotation of recrystallised, elongated (mm- to cm-sized) sigma- and delta-type clasts were found, e.g. from 901.75 m to 915.54 m MD (log depth).

The majority of structures interpreted in the zone of viscose deformation (from 883.75 m to 915.54 m MD log depth) including the flanked intervals with brittle deformation (from 881.05 m to 883.75 m MD log depth and from 915.54 m to 922.30 m MD log depth) are faults (n = 249), consisting of fault planes (n = 123), mirror-like fault planes (n = 125) and stylolitic fault planes (n = 1). In addition, 62 tension gashes / veins and one unassigned fracture were interpreted. In the stereogram of Fig. 5-6, the fault planes show variable dip angles (3° to 90°) with well-defined SE- (mean 127/32; n = 52) and scattered NNE-, NE-, ENE- and E- (mean 032/21; n = 72) dipping planes. In addition, a cluster of SSW-dipping faults was observed (mean 202/57; n = 31). In contrast, tension gashes / veins (see Fig. 5-7) reveal scattered orientations with a weak dominance of E-dipping structures (mean 097/19; n = 15). Both fracture types are concentrated within the upper interval above 900.80 m MD (log depth). Above 905.50 m MD (log depth), the orientations of most faults and tension gashes / veins are subparallel to the bedding and show similar changes in pattern (Fig. 5-4).

Striations on fault planes are very common and clearly developed within this zone. Of the total of 249 faults recorded in this zone, 132 kinematic indicators associated with a predominantly dip-parallel slip could be measured (Fig. 5-8). Although the vertical offsets along faults did not exceed 5 cm, they were clearly visible on the intact cores, which allowed the determination of 46 shear senses. The majority (n = 36) of these shear senses are associated with S- to SSE- and N- to NNW-dipping thrusts / reverse faults (see Figs. 5-8 and 5-9).

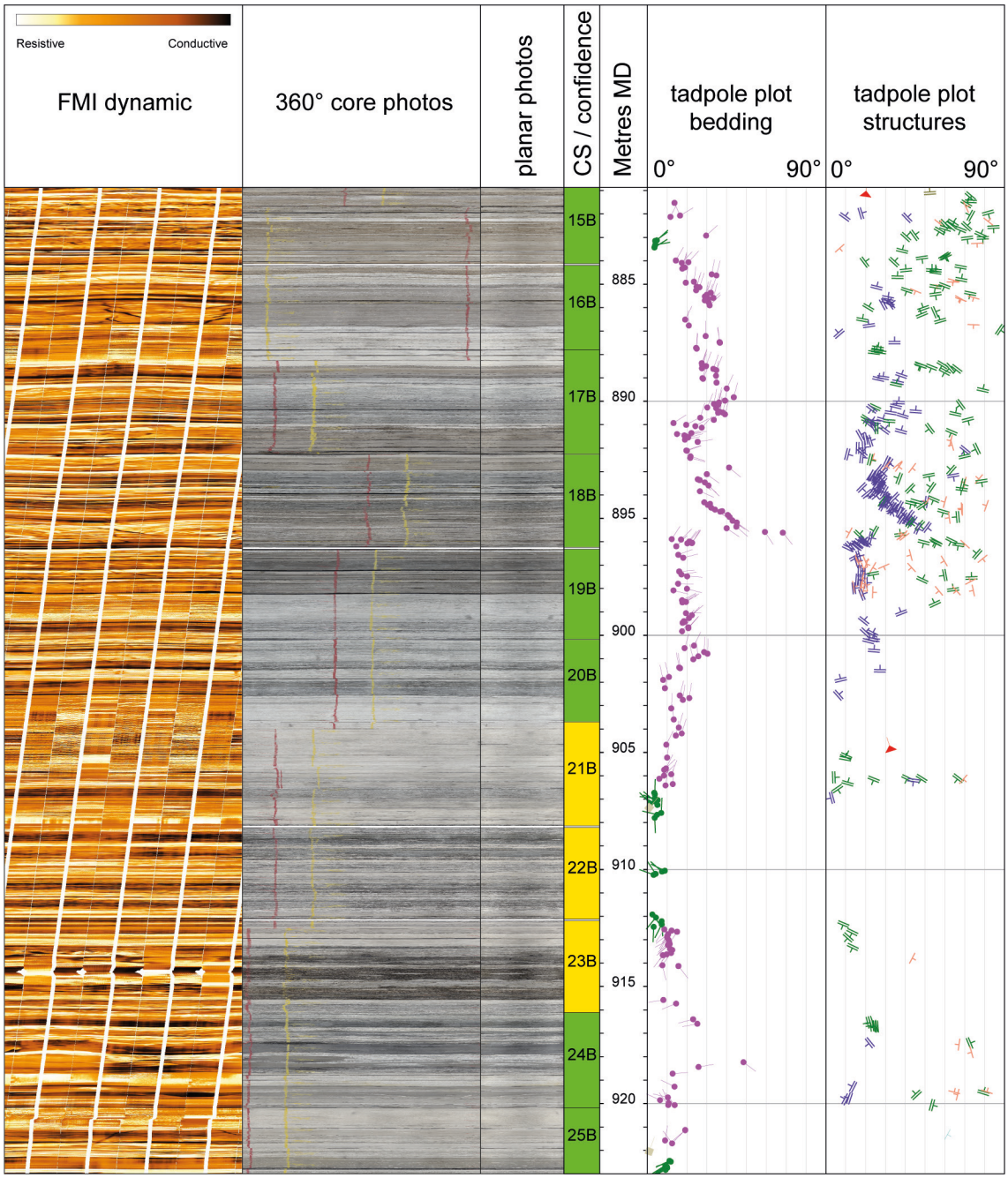


Fig. 5-4: Overview plot of the viscose deformation zone (from 883.75 m to 915.54 m MD log depth) including the flanked brittle deformation (from 881.05 m to 883.75 m MD log depth and from 915.54 m to 922.30 m MD log depth)

Note the separate dip data tracks showing the bedding planes (left) and fractures (right).

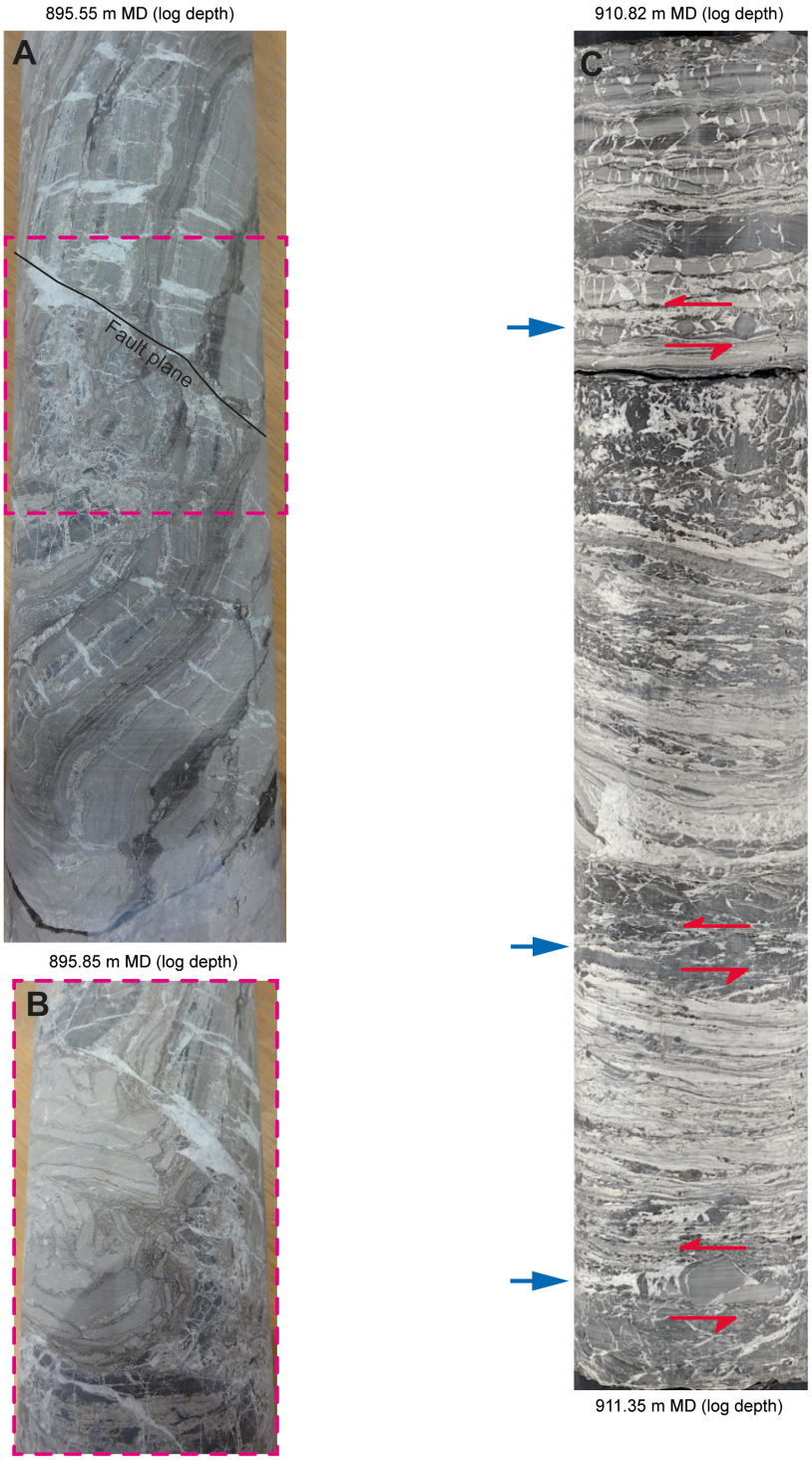


Fig. 5-5: Different deformation fabrics in drill cores

(A) Subvertical, partly folded and faulted beds from 895.55 m to 895.85 m MD (log depth). (B) The mm- to cm-thick veins are oriented perpendicular to the bedding as well as to the fault / dilation breccia, both filled with anhydrite. (C) Example of an intensely sheared, anhydrite- and clay-rich interval from 910.82 m to 911.35 m MD (log depth). Note the rotated sigma-type clay clasts (blue arrows) with associated reaction rims filled by anhydrite (white). The sense of shear is indicated by red arrows.

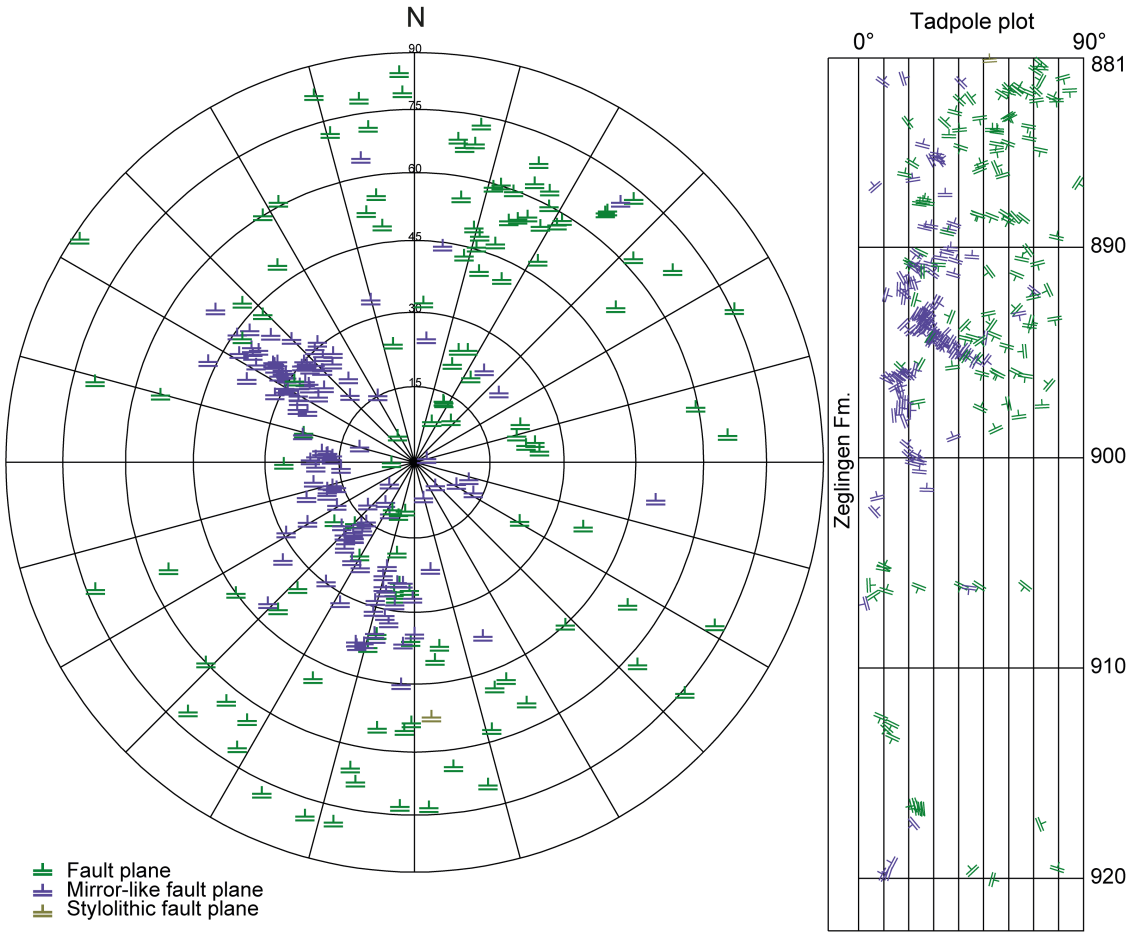


Fig. 5-6: Stereogram and depth plot of fault planes of the viscose deformation zone (from 883.75 m to 915.54 m MD log depth) including the flanked brittle deformation (from 881.05 m to 883.75 m MD log depth and from 915.54 m to 922.30 m MD log depth)

Fault planes (n = 123), mirror-like fault planes (n = 125) and stylolitic fault planes (n = 1).

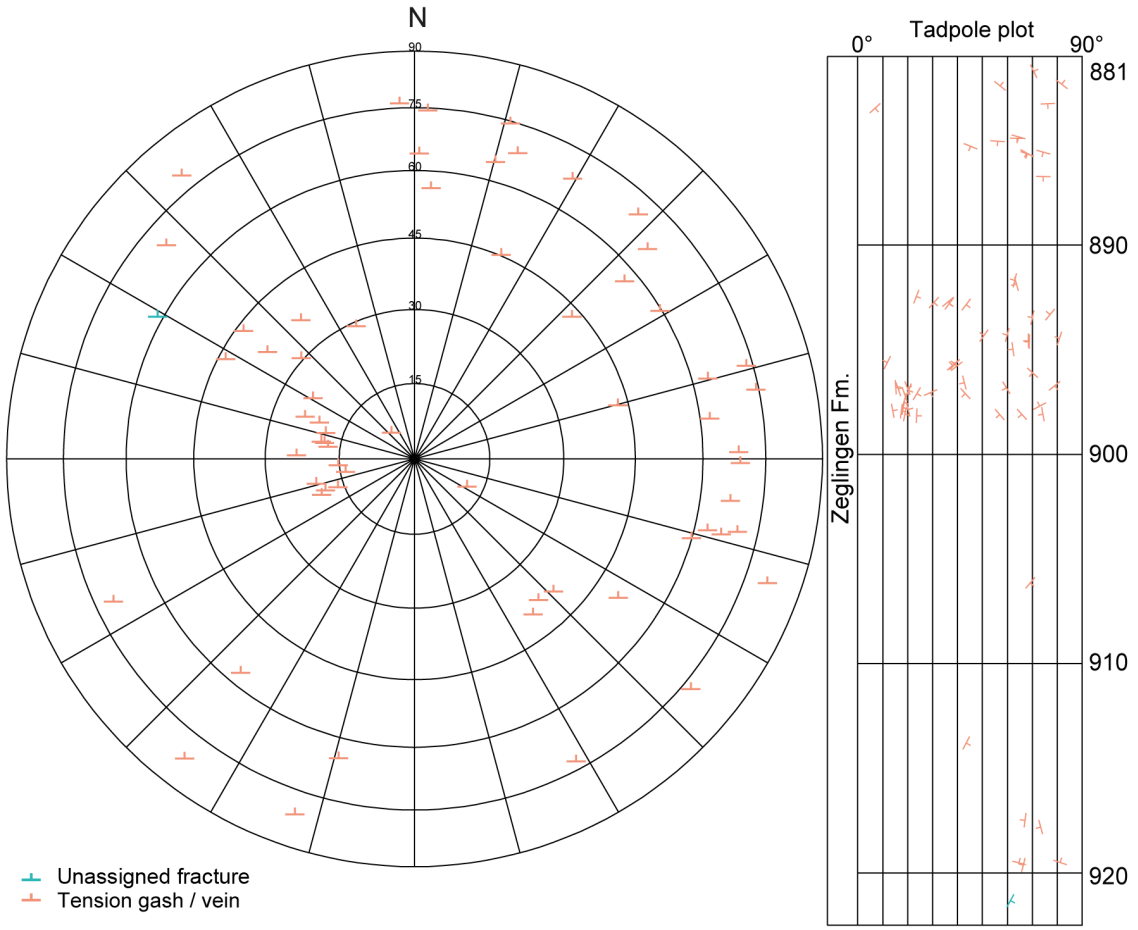


Fig. 5-7: Stereogram and depth plot of tension gashes / veins and unassigned fractures of the viscose deformation zone (from 883.75 m to 915.54 m MD log depth) including the flanked brittle deformation (from 881.05 m to 883.75 m MD log depth and from 915.54 m to 922.30 m MD log depth)

Tension gashes / veins (n = 62) and unassigned fractures (n = 1).

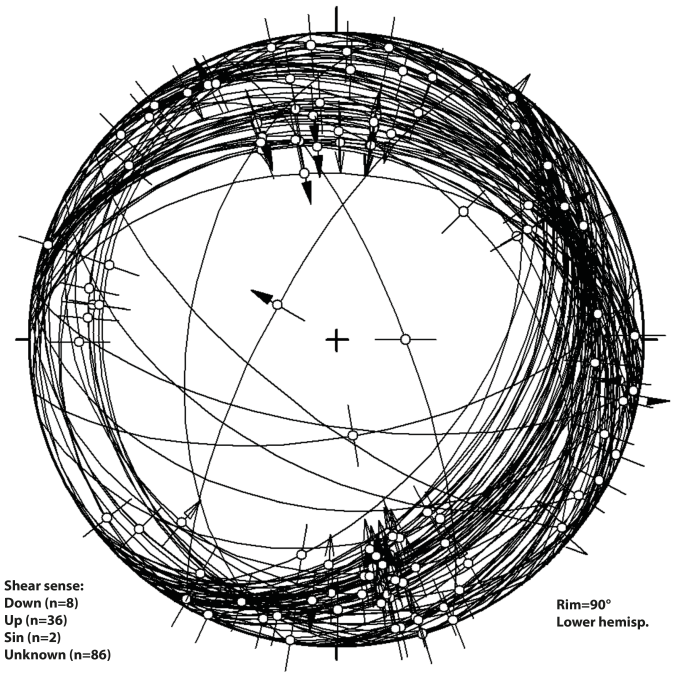


Fig. 5-8: Stereogram of fault planes and associated striations of the viscose deformation zone (from 883.75 m to 915.54 m MD log depth) including the flanked brittle deformation (from 881.05 m to 883.75 m MD log depth and from 915.54 m to 922.30 m MD log depth); n = 132

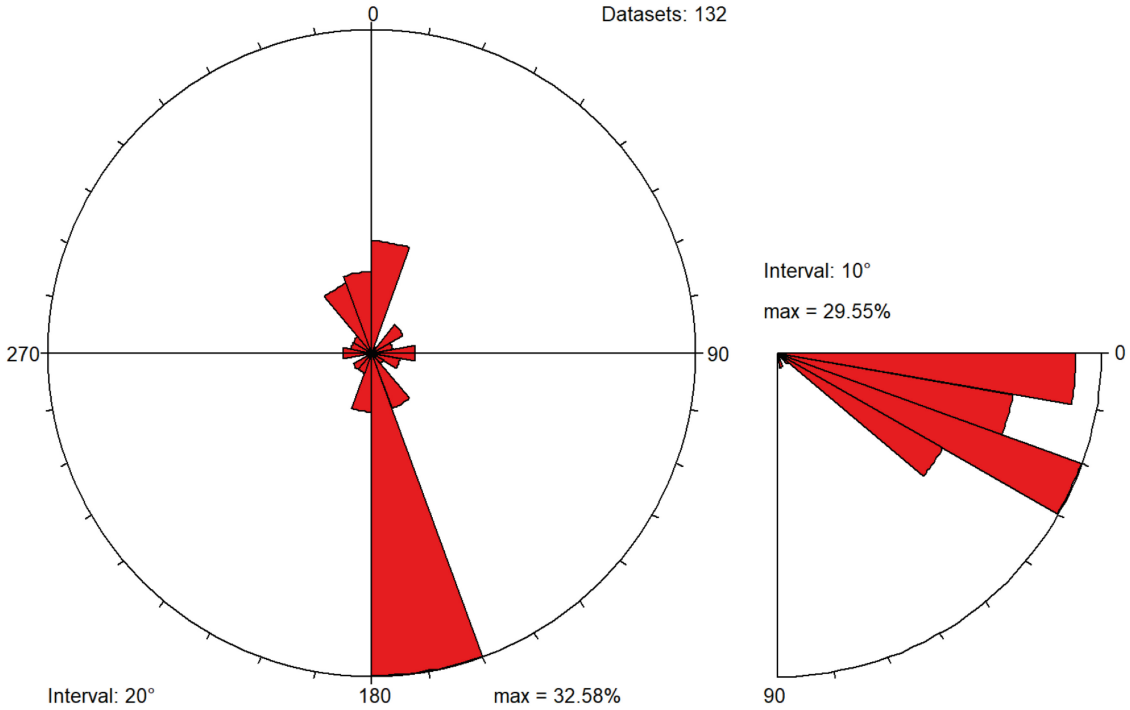


Fig. 5-9: Plunge azimuth rose diagram and plunge histogram of striations of the viscose deformation zone (from 883.75 m to 915.54 m MD log depth) including the flanked brittle deformation (from 881.05 m to 883.75 m MD log depth and from 915.54 m to 922.30 m MD log depth); n = 132

6 References

Barton, N. (1976): The shear strength of rock and rock joints. Int. J. Rock. Mech. Min. Sci. & Geomech. Abstr. 13/9, 255-279.

Barton, N. & Choubey, V. (1977): The shear strength of rock joints in theory and practice. Rock mechanics 10/1-2, 1-54.

Bauer, H., Schröckenfuchs, T. & Decker, K. (2016): Hydrogeological properties of fault zones in a karstified carbonate aquifer (Northern Calcareous Alps, Austria). Hydrogeology Journal 24, 1147-1170.

Ebert, A. & Decker, K. (2019): Structural Analysis Manual. Nagra Arbeitsbericht NAB 19-12.

Hancock, P.L. (1985): Brittle microtectonics: principles and practice. J. Structural Geology 7/3-4, 437-457.

Isler, A., Pasquier, F. & Huber, M. (1984): Geologische Karte der zentralen Nordschweiz 1:100'000. Herausgegeben von der Nagra und der Schweiz. Geol. Komm.

Nagra (2014): SGT Etappe 2: Vorschlag weiter zu untersuchender geologischer Standortgebiete mit zugehörigen Standortarealen für die Oberflächenanlage – Geologische Grundlagen. Dossier II – Sedimentologische und tektonische Verhältnisse. Nagra Technischer Bericht NTB 14-02.

Passchier, C.W. & Trouw, R.A.J. (1996): Microtectonics. Springer, 289 pp.

Peacock, D.C.P., Nixon, C.W., Rotevatn, A. & Sanderson, D.J. (2016): Glossary of faults and other fracture networks. J. Structural Geology 92, 12-29.

Pietsch, J. & Jordan, P. (2014): Digitales Höhenmodell Basis Quartär der Nordschweiz – Version 2013 (SGT E2) und ausgewählte Auswertungen. Nagra Arbeitsbericht NAB 14-02.